QUANTITATIVE NON-DESTRUCTIVE EVALUATION (NDE) OF FRP LAMINATE-CONCRETE BOND STRENGTH

by

MINA RIAD

Presented to the Faculty of the Graduate School of

The University of Texas at Arlington in Partial Fulfillment

of the Requirements

for the Degree of

DOCTOR OF PHILOSOPHY

THE UNIVERSITY OF TEXAS AT ARLINGTON

December 2017

Acknowledgements

First and foremost, my thanks and gratitude are to God for giving me the strength to complete this research.

My sincere appreciation goes to my advisor Dr. Nur Yazdani for his generous guidance, sincere help, consistent support and advice through all stages of this research work. I am grateful to Dr. Shih-Ho Chao, Dr. Raad Azzawi and Dr. Jay Rosenberger for readily accepting to serve on my dissertation committee as well as for their support during my study. I will be always grateful to the Department of Civil Engineering at UT Arlington for providing me with supports and facilities to perform my research work.

I am thankful to my friends Eyosias Beneberu, Santosh Timilsnia, Tariq Al Jaafreh, Yazan Almomani, Natawut Chaiwino and Towfiqul Alquadir for all the help and hard work during the experiment.

I am deeply grateful to my family who stood by my side through the entirety of this research.

November 15, 2017

Abstract

QUANTITATIVE NON-DESTRUCTIVE EVALUATION (NDE) OF

FRP LAMINATE-CONCRETE BOND STRENGTH

Mina Riad, PhD

The University of Texas at Arlington, 2017

Supervising Professor: Nur Yazdani

Repair and rehabilitation methods for civil infrastructure have become a topic of great interest to engineers. Fiber Reinforced Polymer (FRP) is considered as one of the most popular and practical solutions for strengthening and retrofitting of civil infrastructure. Several past studies indicated that significant increase in strength and stiffness can be achieved by using this technology. The FRP-concrete interface bond is critical in transferring stresses from the concrete surface to the FRP. However, the evaluation of the bond strength is still a challenging issue.

To evaluate the bond strength using non-destructive techniques, 32 concrete beams strengthened with FRP using different parameters affecting the bond strength (surface roughness, voids, Epoxy type, Epoxy layers, FRP type, surface preparation, application direction and surface wetness) were tested. The experiment was conducted with the objective of determining the suitable non-destructive method to detect each of the parameters in study, determining the effect of each parameter in study on the bond strength between the concrete and the FRP and finally use finite element models to prepare a set of relationships graphs between each of the parameters in study and the bond strength. The test samples were scanned using ground generating radar (GPR), ultrasound tomography, Infrared camera and Schmidt hammer.

Table of Contents

Acknowledgements iii

Abstract iv

List of Illustrations viii

List of Tables xiv

Chapter 1 INTRODUCTION 15

Introduction 15

Background 15

Problem Statement 18

Objectives 19

Organization of the Dissertation 20

Chapter 2 LITERATURE REVIEW 22

Introduction 22

FRP Laminate-Concrete Bond characteristics 23

Destructive testing 27

ASTM pull-off test 28

Witness panel test 29

Non-destructive testing 30

Visual inspection 31

Mechanical and acoustic vibration 31

Radiographic imaging 32

Optical methods 33

Thermographic imaging 34

Acoustic emission 39

Ultrasonic methods 40

Electromagnetic techniques 43
Ground penetrating radar 44
Limitation of previous study and significance of the research 48
Chapter 3 DESIGN OF EXPERIMENT AND SAMPLES CONSTRUCTION 49
Introduction 49
Design of Experiment 49
Samples preparation 55
Instrumentation Plan 63
Chapter 4 NON-DESTRUCTIVE TESTING 65
Introduction 65
Rebound Hammer Test 65
Infrared camera 76
Ultrasound Tomography Test 90
Ground Penetrating Radar (GPR) Test 103
Chapter 5 Destructive testing 121
Introduction 121
Pull-off Test 121
Three points bending test 133
Chapter 6 Numerical Modelling 148
Introduction 148
Development of modeling framework 148
Model Geometry and element types 152
Model adjustment and calibration 155
Chapter 7 Conclusions and recommendations 163
Introduction 163

Summary of findings and conclusion 163
Proposed procedures 166
Future Research 169
Appendix A 171
References 175
Biographical Information 184

List of Illustrations

Figure 1- 1: Types of debonding failures [Hesham, 2013]. 16
Figure 1- 2: Research approach 20
Figure 2- 1: Failure modes of FRP-strengthened concrete beams [Teng et al. 2003]. 24
Figure 2- 2: ASTM pull-off test 28
Figure 2- 3: ASTM pull-off test modes of failure [ASTM D7522/D7522M-15, 2015] 29
Figure 2- 4: Concept of radiographic inspection
[https://www.ndeed.org/GeneralResources/MethodSummary/RT1.jpg] 32
Figure 2- 5: Optical method [http://www.nanotech.jo] 34
Figure 2- 6: Grayscale infrared image [Halabe et al. 2003] 37
Figure 2- 7: Infrared image of concrete sample with embedded flaws [Monica et al. 2003] 37
Figure 2- 8: 3D view of thermal image after heating [Taillade et al. 2012] 38
Figure 2- 9: Bond testing using ultrasound method [Ribolla et al. 2016] 41
Figure 2- 10: Ground Penetrating Radar (GPR) 44
Figure 2- 11: Schematic diagram of generic GPR system 45
Figure 2- 12: GPR scan 46
Figure 2- 13: Results of GPR test showing smaller sized WF voids [Hing et al. 2006] 47
Figure 3- 1: Schematic of the beam sample 56
Figure 3- 2: Formwork Preparation 56
Figure 3- 3: Casting of the concrete beams 57
Figure 3- 4: Voids preparation 57
Figure 3- 5: Concrete surface roughness (CSP) 58
Figure 3- 6: Concrete surface preparation 59
Figure 3- 7: Cutting of the FRP 60

Figure 3- 8: Mixing of the Epoxy 61
Figure 3- 9: Applying the Epoxy 62
Figure 3- 10: FRP application 62
Figure 3- 11: The concrete beams after attaching the FRP 63
Figure 3- 12: Strain gages location 64
Figure 3- 13: Displacement transducer location 64
Figure 4- 1: Schmidt hammer 65
Figure 4- 2: Schmidt hammer test points 66
Figure 4- 3: Marking of the test points 67
Figure 4- 4: Schmidt hammer testing at the FRP surface 67
Figure 4- 5: Schmidt hammer testing at the concrete surface 68
Figure 4- 6: Schmidt Hammer test data 69
Figure 4- 7: Minitab software for statistical analysis 70
Figure 4- 8: Residual Plots for Q value (%) 71
Figure 4- 9: Plots of responses versus each parameter 72
Figure 4- 10: Main Effect of the parameters 72
Figure 4- 11: Interaction plot for Q value 73
Figure 4- 12: FRP sheets 75
Figure 4- 13: Effect of delamination on the Q value 76
Figure 4- 14: Infrared camera 77
Figure 4- 15: Infrared camera test setup 78
Figure 4- 16: Adjustable heat source 79
Figure 4- 17: Infrared camera video recording 79
Figure 4- 18: “FLIR Research IR” software 80
Figure 4- 19: Rate of cooling time after 40 seconds 81

Figure 4- 20: Residual Plots for Rate of cooling down (%) after 40 seconds 82
Figure 4- 21: Plots of responses after 40 seconds versus each parameter 83
Figure 4- 22: Main Effect of the parameters 83
Figure 4- 23: Interaction plot for the rate of cooling down 84
Figure 4- 24: Infrared camera test setup to locate voids and delaminations 87
Figure 4- 25: Heating the beam using heat lamp 87
Figure 4- 26: Infrared camera used to capture pictures of the beam surface 88
Figure 4- 27: Infrared camera picture of two 0.8 in × 0.8 in voids 89
Figure 4- 28: Infrared camera picture of two 1.6 in × 1.6 in voids 89
Figure 4- 29: Infrared camera picture of debonded FRP layer 90
Figure 4- 30: Ultrasonic tomography device 91
Figure 4- 31: Ultrasonic test configuration 92
Figure 4- 32: Ultrasonic tomography handle 93
Figure 4- 33: Ultrasonic testing over the FRP surface 93
Figure 4- 34: Ultrasonic testing over the concrete surface 94
Figure 4- 35: A sample of the B-scan of two different beams 94
Figure 4- 36: Residual Plots for the amplitude (%) 95
Figure 4- 37: Plots of responses versus each parameter 96
Figure 4- 38: Main Effect of the parameters 97
Figure 4- 39: Interaction plot for the amplitude value 97
Figure 4- 40: Ultrasound B-scan of two 0.8 in × 0.8 in voids 100
Figure 4- 41: Ultrasound B-scan of two 1.6 in × 1.6 in voids 100
Figure 4- 42: Ultrasound B-scan debonded FRP layer 101
Figure 4- 43: Main Effect of the parameters 102
Figure 4- 44: Interaction plot for the amplitude value 102

Figure 4- 45: Typical GPR A-scan 104
Figure 4- 46: GPR 2600 MHz antenna 105
Figure 4- 47: GPR Test configuration 105
Figure 4- 48: GPR device 106
Figure 4- 49: 2600 MHz antenna connected to a mini-cart 106
Figure 4- 50: A sample of the B-scan of two different beams 107
Figure 4- 51: A sample of the A-scan of three different beams 107
Figure 4- 52: Residual Plots for the Negative amplitude (%) 108
Figure 4- 53: Plots of responses versus each parameter 109
Figure 4- 54: Main Effect of the parameters 109
Figure 4- 55: Interaction plot for the amplitude value 110
Figure 4- 56: Ultrasound B-scan of two 1.6 in × 1.6 in voids 113
Figure 4- 57: Ultrasound B-scan of two 0.8 in × 0.8 in voids 113
Figure 4- 58: GPR test configuration after adding the additional layer 114
Figure 4- 59: Residual Plots for the amplitude (%) 115
Figure 4- 60: Plots of responses versus each parameter 116
Figure 4- 61: Main Effect of the parameters 116
Figure 4- 62: Interaction plots of the parameters 117
Figure 5- 1: Pull-off test mechanism 120
Figure 5- 2: Pull-off test mechanism 121
Figure 5- 3: Pull-off test locations. 122
Figure 5- 4: Core drilling 122
Figure 5- 5: Two inch diameter dolly 123
Figure 5- 6: Epoxy application to dolly surface 123

Figure 5- 7: Dollies attached to concrete surface 124
Figure 5- 8: Pull-off tester 124
Figure 5- 9: Dolly pulled from beam surface 125
Figure 5- 10: Various observed failure modes: 128
Figure 5- 11: Residual Plots for pull-off test 129
Figure 5- 12: Plots of the failure stress versus each parameter 130
Figure 5- 13: Main Effect of the parameters 131
Figure 5- 14: Interaction plot for the rate of cooling down 131
Figure 5- 15: Schematic Apparatus for Flexure Test of Concrete by Three Point Loading Method [ASTM C293/C293M, 2016] 132
Figure 5- 16: Debonding and delamination of externally bonded FRP systems [ACI 440, 2017] 133
Figure 5- 17: Bending test setup 134
Figure 5- 18: Displacement transducer location 135
Figure 5- 19: Concrete and FRP Strain gages 136
Figure 5- 20: Strain gages attached to the concrete beams 137
Figure 5- 21: Setup of the three points bending test 138
Figure 5- 22: Data acquisition system 139
Figure 5- 23: Three points bending test failure 141
Figure 5- 24: Debonding of the FRP layer 142
Figure 5- 25: Residual Plots for the three points bending test 143
Figure 5- 26: Plots of the failure load versus each parameter 144
Figure 5- 27: Main Effect of the parameters 145
Figure 5- 28: Interaction plot for the three points bending test 145
Figure 6- 1: Response of concrete to uniaxial loading [Obaidat, 2011] 149

Figure 6- 2: ABAQUS model geometry 151
Figure 6- 3: FRP sheet as modeled in ABAQUS 152
Figure 6- 4: Concrete beam as modeled in ABAQUS 152
Figure 6- 5: Mesh used in ABAQUS model 153
Figure 6- 6: ASTM cylinders compressive test setup 155
Figure 6- 7: ASTM FRP coupon test 156
Figure 6- 8: Load-displacement curve of a beam 157
Figure 6- 9: Main Effect of the parameters 159
Figure 6- 10: interaction plots 160
Figure 6- 11: Relationship between the voids area and the strength of the bond 161
Figure 7- 1: Proposed procedures to evaluate the bond strength flowchart 167

List of Tables

Table 3-1: Fractional Factorial with 6 parameters having two Levels [NIST/SEMATECH handbook, 2012]……50

Table 3-2: Experimental Matrix……...54

Table 4- 1: Analysis of variance for the Schmidt hammer test……...74

Table 4- 2: Analysis of variance for the Infrared camera test……85

Table 4- 3: Analysis of variance for the ultrasound test……..98

Table 4- 4: Analysis of variance for the GPR test……111

Table 4- 5: Analysis of variance for the GPR test after covering the sample with additional layer……...119

Table 5- 1: Summary of Pull-off test results……...125

Table 5- 2: Summary of three points bending test……139

Table 6- 1: Cylinder test results……..154

Table 6- 2: Results of the calibration process……157

Chapter 1

INTRODUCTION

Introduction

Repair and rehabilitation methods for civil infrastructure have become a topic of great interest to engineers, and Fiber Reinforced Polymer (FRP) laminate is one of the most popular and practical solutions for strengthening and retrofitting of concrete structures. Several past studies indicated that significant increase in strength and stiffness can be achieved by using this technology. The quality of the FRP-concrete bond is critical in transferring stresses through the interface, and the in-situ evaluation of the bond strength is still a challenging issue.

Background

Fiber reinforced polymer composites have emerged as a potential solution to the problems associated with strengthening deteriorating and/or under-designed concrete infrastructures [Meier, 1995]. The advantages of using the FRP in the strengthening of existing structures are the high strength to weight ratio [Bakis et al., 2002], the fast and easy application, the confinement of concrete elements and the corrosion resistance. The application of the external very thin FRP has little effect on the dimension of the member under repair. Therefore, they are widely used whenever there is a change in use of the structure, construction defects, code changes, seismic/blast retrofit, and deterioration of existing structure. Although externally bonded FRP performed well in practice, premature debonding failure was observed and identified by many researchers to be one of the problems with FRP.

For the repair to be effective, the bonded layer must work together with the original structure. However, under variable conditions, interfacial debonding of the bonded layer from the concrete surface may occur as illustrated in Figure 1-1. Debonding may initiate

at the end of the bonded layer, where a high strain gradient exists [Taljsten, 1997]. When the workmanship is not good enough, imperfect bonding may lead to the formation of debonded zones under the FRP layer. Debonding may also initiate at the bottom of a flexural crack or flexural shear crack, leading to the formation of a debonded region away from the edge of the FRP layer [Leung, 2001]. If the debonding is left unrepaired, its continued growth may lead to failure of the repair. The detection of the interfacial debonding in its early stage is, therefore, a very important task in monitoring the health of structures retrofitted with the bonded plate. Several other factors may lead to premature failure of the bond such as the surface preparation, quality of the adhesive material and the surface roughness.

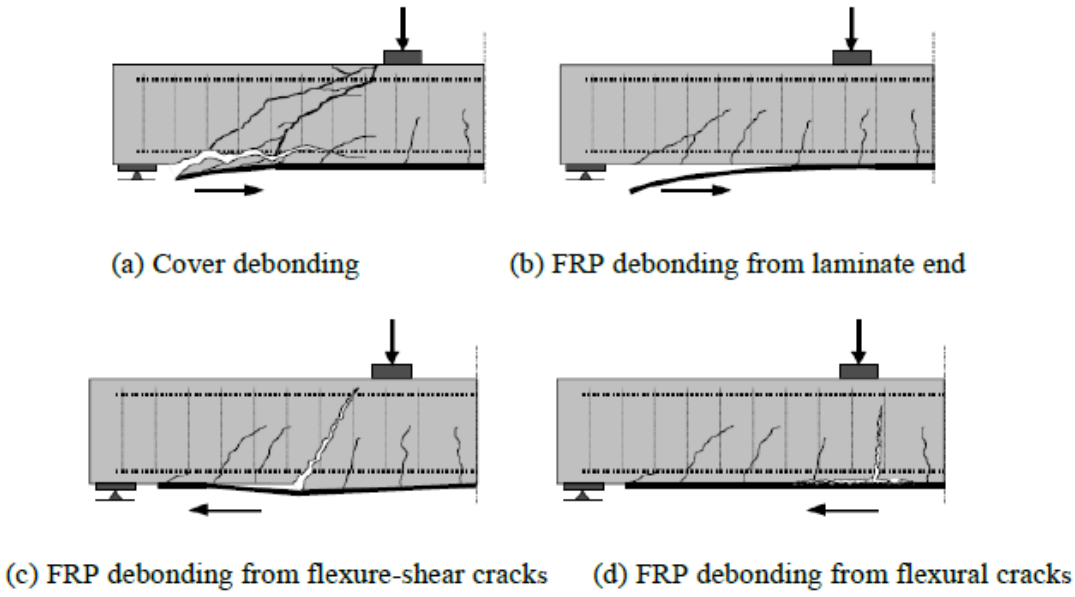

Figure 1-1: Types of debonding failures [Hesham, 2013].

Visual inspection and acoustic sounding (hammer tapping) are commonly used to detect delaminations. However, these current practices are unable to provide relevant information about the depth and width of debonded areas and they are not capable of evaluating the level of adhesion between the FRP and the concrete [Taillade et al. 2012].

Consequently different authors have developed nondestructive methods to assess the quality of the FRP concrete bond [Karbhari et al. 2005]. Based on the impact-echo technology [Maerz et al. 2008], the ultrasound technology [Mirmiran et al. 2001], the infrared detection technology [Galietti et al. 2007 and Monica et al. 2003], and the Microwave and radar technology [Akuthota et al. 2004 and Tzu-Yang et al., 2008]. Most of these NDE methods involve techniques adequate for limited characterization (location and size) of defects like pores, delamination or debonding within the adhesive layer. There is so far no NDE technique that is able to quantify the strength of the bond [Bastien et al. 2010]. This lack remains a major issue set against a wider application of the FRP adhesive bonding technology.

Several prior studies were focused on determining the bond strength between composites in areas other than civil engineering such as medicine, mechanical engineering, aviation and automotive manufacturers. Methods of acoustic emission [Choi et al. 2011 and Santulli et al. 1999], radiography [Nagarkar et al. 2001], acoustic-optical fiber [Ying et al. 2015], ultrasonic [Cantrell, 2004 and Brotherhood et al. 2003], guided mechanical waves [Le Crom et al. 2010 and Huo et al. 2007], infrared camera [Moore, 2009] and laser adhesion test [Arrigoni et al. 2008] were used to evaluate the bond strength. Despite the fact that these studies dealt with smooth surfaces and homogeneous materials that are different than the case of reinforced concrete and FRP, they provide promising approaches to be followed in case of rough and permeable surfaces.

Problem Statement

The bond between the FRP laminate and concrete imposes many challenges for quality control and assurance. Unlike welding and other critical structural construction methods, the epoxy layer is covered by the FRP and visual inspection cannot give a clear assessment of the quality of the bond or the concrete behind the FRP. Steel members corrode and concrete members exhibit cracking and spalling. However, the deterioration of FRP covered concrete member is not visible.

The ACI 440.2R-08 guidelines, the premier publication for externally applied FRP-concrete structures [ACI 440, 2008] provide some criteria for evaluation, inspection, and acceptance of FRP composite using visual inspection and destructive testing. Reference is made to non–destructive testing without specifying any requirements, procedures or guidelines for the non-destructive testing method.

There are no clear recommendations or limitations for the factors affecting the bond strength. The ACI 440.2R-08 document defines limits for the void sizes and area in order to neglect its effect on the total bond strength. Otherwise, the affected bonded area needs to be repaired. The ACI document does not mention how much bond strength is lost if the voids exceed these limits.

The ACI 440.3R-04 [ACI 440.3R, 2004] contains only two methods for testing the composite action between the concrete and the FRP. The two tests are the ASTM pull-off test [ASTM D7522/D7522M-15, 2015] and the witness panel test [ASTM D 3039, 2014]. The two tests recommended by ACI 440 lack the ability to detect the overall quality of the bond. The two tests are destructive, localized and could not be used regularly to monitor the condition of the bond. Some defects, cracks and voids may be unnoticed.

Objectives

This research aims to develop reliable and convenient procedures to be followed to quantitatively evaluate the FRP-concrete bond strength using non-destructive methods. The proposed concept consists of using the NDE approach to obtain NDE test parameters (such as ultrasonic attenuation, velocity change, thermal dissipation, refraction angle change and amplitude change) from test samples and then to correlate the parameters with the actual bond strengths measured when these same samples are destructively examined. Various parameters affecting the bond strength, such as surface roughness, voids, epoxy type and thickness, and FRP type, were considered.

The experiment was conducted with the objective of determining the suitability of NDT methods to detect these parameters, find the associated bond capacity of each sample through a bending test and finally, use finite element modeling to develop quantitative relationships between each of the parameters in the study and the associated bond strengths.

The following NDT methods were used: ground generating radar (GPR), ultrasound tomography, infrared camera and Schmidt hammer. The relationships will be very useful to structural engineers in estimating the in-service bond conditions of applied FRP laminate, thereby estimating the expected strength contribution of the laminate in the overall flexural strength of structural members. Figure 1-2 illustrates the different steps to achieve the objectives of the research.

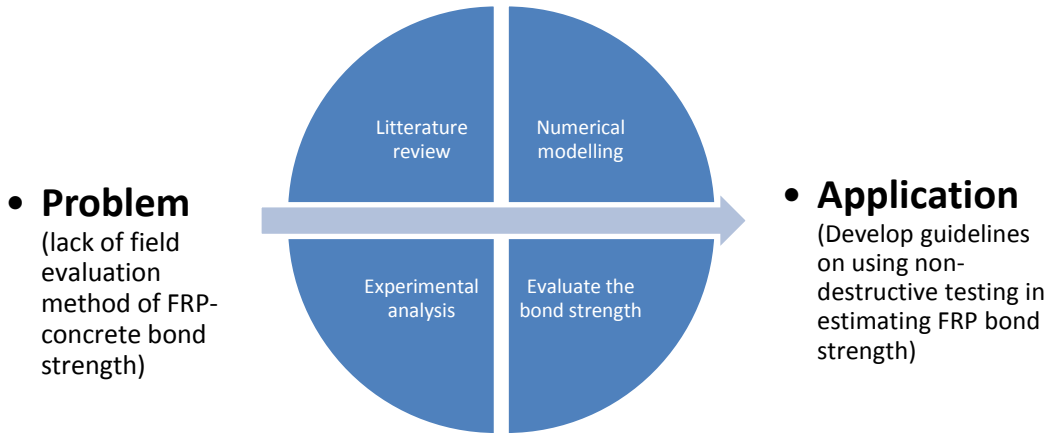

Figure 1-2: Research approach

Organization of the Dissertation

This dissertation is organized into seven chapters. The content of the remainder of this dissertation is as follows:

- *Chapter 2-Literature Review:*

  This chapter presents a review of the FRP properties and the conducted research on the FRP bond strength. The new developments in the non-destructive techniques along with the description of these methods.

- *Chapter 3-Design of Experiment and Samples Construction:*

  The design of the test samples, the method used to determine the required number of samples for the study, instrumentation plans and samples preparation are presented in this chapter.

- *Chapter 4-Non-destructive testing:*

  In this chapter, the non-destructive testing performed to evaluate the bond strength are presented. The results organized by the NDT methods used: Schmidt hammer, infrared camera, ultrasound tomography and ground generating radar (GPR).

- *Chapter 5-Destructive testing:*

  Two destructive tests are presented in this chapter, the pull-off test and the bending test.

- *Chapter 6-Numerical Modelling:*

  This chapter discusses the numerical modeling performed to develop quantitative relationships between each of the parameters in the study and the associated bond strengths.

- *Chapter 7-Conclusions and Recommendations:*

  Finally, a summary of findings, conclusions and future recommendations are presented in Chapter 7.

Chapter 2

LITERATURE REVIEW

Introduction

Fiber reinforced polymer (FRP) emerged as a popular strengthening agent for deteriorating and/or under-designed concrete infrastructures. FRP is a composite material made of resin matrix reinforced with fibers. The load is carried mostly by fibers. The fibers can be made of glass, carbon or aramid. The combination of these fibers and matrices will result in different kinds of FRPs, such as GFRP, CFRP or AFRP. There are two main types of FRP rehabilitation methods, embedded FRP rebars and externally applied FRP laminates.

The first type is embedded FRP rebar. They are highly corrosion resistant and unlike steel, will not rust when exposed to harsh weather and chemicals. They are also non-conductive, impact resistant, and has higher strength relative to steel.

The second type is externally applied FRP laminates (also known as FRP wrapping). In this technique, the FRP fabric is saturated with a polymeric epoxy and the fabric is applied to the desired surface of a structure. This wrapping technique is known as the wet-layup or prefabricated systems using cold cured adhesive bonding. They are being effectively used for their high strength to weight ratio [Bakis et al., 2002], fast and easy application, confinement of concrete elements and excellent corrosion resistance. It can be used whenever there is a change in use of the structure, construction defect, code change, seismic retrofit, or deterioration of an existing structure.

Externally applied FRP laminates are currently the most commonly used techniques for strengthening bridges and concrete structures. In spite of the significant research being

reported on their structural mechanism and performance, there are still heightened concerns regarding possible premature failure due to debonding [Rizkalla et al. 2003].

FRP Laminate-Concrete Bond characteristics

The load is transferred through the interface of the FRP laminate and the concrete. The strength and stiffness of bond are critical to the performance of the overall structure strengthened with FRP. The mechanism of the load transfer consists of three components:

- Epoxy applied at the interface of concrete and FRP.
- Friction between FRP and concrete which depends on the roughness of surfaces.
- Mechanical interlocking can be in different forms, by applying mechanical anchors or gluing aggregates on the surface of FRP. In mechanically-fastened FRP, the laminates are fastened to FRP with steel fasteners and bolts to increase the bond strength.

For concrete beams, strengthened with FRP laminates, a number of failure modes are possible as shown in Figure 2-1[Teng et al. 2003]. Failure can occur when the ultimate flexural capacity of the beam is reached, by either tensile rupture of the FRP sheet (Figure 2-1a) or crushing of concrete (Figure 2-1b). The beam can also fail in shear if the flexural capacity of the strengthened beam exceeds the shear capacity (Figure 2-1c). Although the desirable mode of failure is FRP rupture (meaning when the maximum capacity of the system is attained), the most common mode of failure is debonding. Numerous experimental studies have reported brittle debonding failure in FRP strengthened concrete beams prior to their ultimate flexural or shear strength is reached.

A variety of debonding failure modes have been observed in tests [Saadatmanesh et al. 1991], and these types of failures can be classified into two types:

- Failure associated with high interfacial stresses near the ends of the FRP laminate (Figure 2-1d and Figure 2-1e).
- Failure induced by a flexural or flexural-shear crack (intermediate crack) away from the FRP laminate ends (Figure 2-1f).

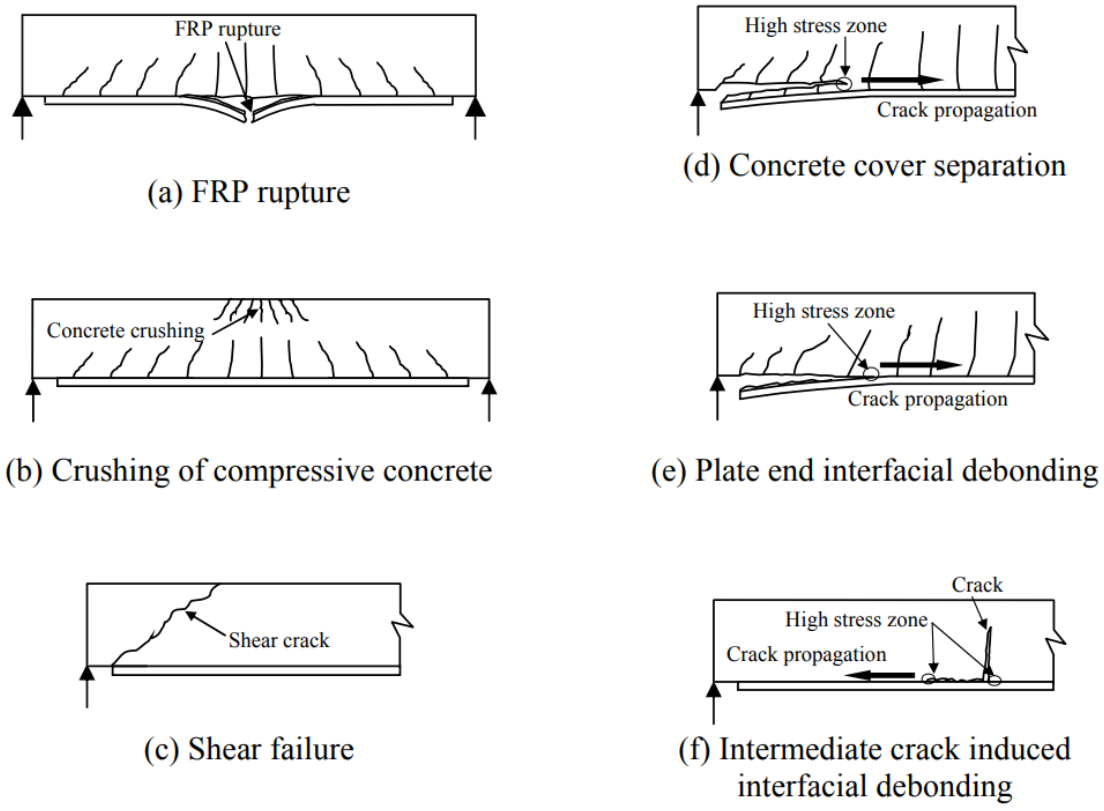

Figure 2-1: Failure modes of FRP-strengthened concrete beams [Teng et al. 2003].

Debonding is an important failure mode as it prevents the full ultimate flexural capacity of the beam from being achieved. This type of failure is often brittle, occur with little or no

visible warning, and take place at load levels significantly lower than the flexural or shear strength of the retrofitted system. As a result, the bond strength and the factors affecting the bond between the FRP and concrete have been of great interest to researchers. There have been several studies of the bond behavior between the FRP and the concrete to study the mechanism of load transfer and examine the various parameters which influence the bond strength.

Many researchers have studied the effects of the bond length. While bond strength increase as the bond length increase, when the bond length increase beyond a certain extent, the bond strength does not increase any further. Bizindavyi et al. (1999) performed an experimental and analytical investigation on transfer lengths and bond strengths of composite laminates bonded to concrete. A series of pull-out tests were performed and the observed modes of failure were shearing of the concrete beneath the epoxy and rupture of the composite coupon [Bizindavyi et al. 1999].

Nakaba et al. (2001) conducted double lap shear tests to investigate the bond behavior between FRP and concrete. Different types of fibers and concrete mixtures were studied to determine the influence of the strength of concrete and FRP on the bond strength. It was concluded that the bond strength is affected by concrete properties, but the FRP properties were not as effective as concrete properties [Nakaba et al. 2001].

De Lorenzis et al. (2001) performed flexural tests to determine the effectiveness of concrete strength, FRP stiffness, bonded length and surface preparation on the bond strength. The failure occurred in the concrete-adhesive interface, with very little or no sign of damage in the concrete surface. It was concluded that the bonded length does not have a significant effect on the ultimate load but the number of FRP sheets influenced the

ultimate load. Due to the failure mode, the concrete strength did not affect the ultimate load. Also, it was concluded that a roughened surface performs much better than a smooth surface [De Lorenzis et al. 2001].

Chen et.al (2001) conducted five different types of tests to examine the bond behavior of FRP and concrete. It was concluded that the type of test affects the bond strength and also a slight change in the geometry of elements can influence the final results. Test data suggest that the main failure mode is a concrete failure under shear, occurring generally at a few millimeters from the concrete-to-adhesive surface. The bond strength, therefore, depends strongly on the concrete strength. In addition, the plate-to-concrete member width ratio has a significant effect [Chen et al. 2001].

Ueda et.al (2003) tested several single lap pull-out samples with different types of FRP and adhesive, to understand the behavior of the bond between FRP and concrete. Applying high strength FRP laminates and low shear stiffness epoxy was recommended to improve the bond behavior of FRP and concrete [Ueda et al. 2003].

Coronado et.al (2006) Conducted flexural tests to study the bond behavior using experimental data obtained from 19 beams strengthened with different types of FRP. These beams failed by concrete crushing, cover failure and plate debonding. It was found that the fracture energy of the concrete–repair interface plays a central part in predicting plate-debonding failures [Coronado et al. 2006].

Therefore, the strength and stiffness of bond are critical to the performance of the overall structure strengthened with FRP. Unlike welding and other critical structural construction

methods, the epoxy layer is covered by the FRP and visual inspection cannot give a clear assessment of the quality of the bond or the concrete behind the FRP. Steel members corrode and concrete members exhibit cracking and spalling. However, the deterioration of FRP covered concrete member is not visible. The bond between the FRP laminate and concrete imposes many challenges for quality control and assurance.

The ACI 440.2R-08 guidelines, the premier publication for externally applied FRP-concrete structures [ACI 440, 2008] provide some criteria for evaluation, inspection, and acceptance of FRP composite using visual inspection and destructive testing. Reference is made to non–destructive testing without specifying any requirements, procedures or guidelines for the non-destructive testing method. The available methods for evaluation of FRP to concrete bond strength are presented as follows.

Destructive testing

Destructive testing for the FRP gives the inspector the ability to determine the areas of deficiency by testing the FRP conditions in situ. Due to the nature of the tests, careful analysis must be completed in order to ensure the test is suitable and will give useful results to the engineers.

The ACI 440.3R-04 [ACI 440.3R, 2004] contains only two methods for testing the composite action between the concrete and the FRP. The two tests are the ASTM pull-off test [ASTM D7522/D7522M-15, 2015] and the witness panel test [ASTM D 3039, 2014].

ASTM pull-off test

The pull-off test, as illustrated in Figure 2-2 is performed by securing a 25 to 40 mm square or circular plate area adhered to the surface of the FRP or concrete with a bonding agent. After the bonding agent is cured, a test apparatus is attached to the loading fixture and aligned to apply tension perpendicular to the concrete. The specimen is loaded until the adhesion fixture detaches from the surface.

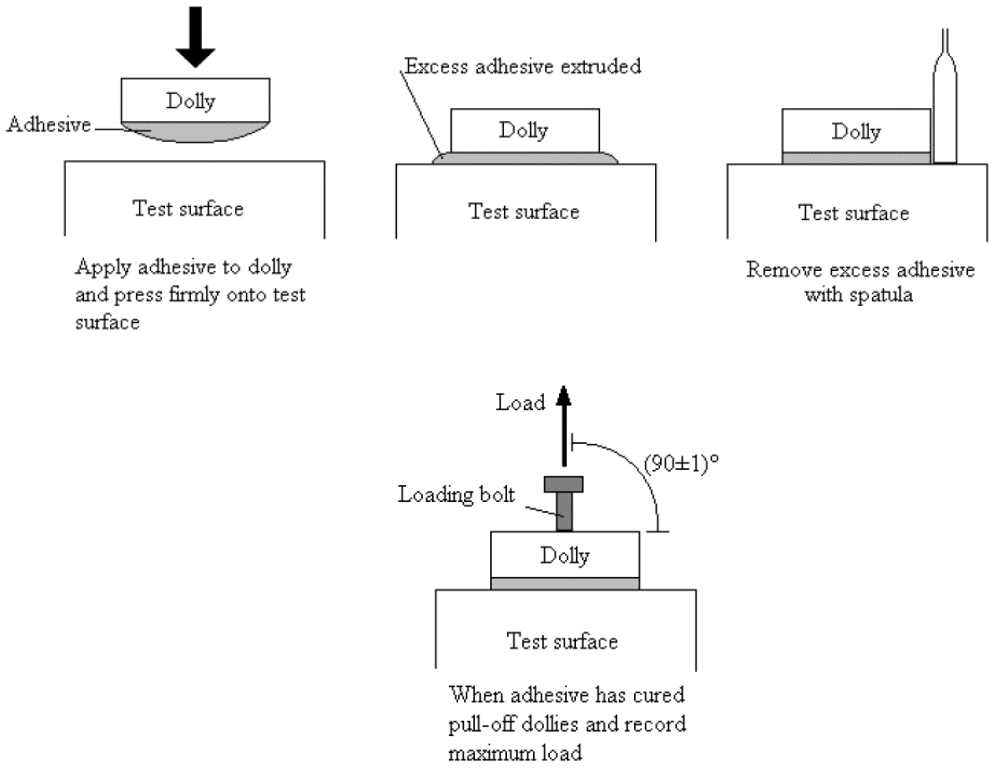

Figure 2-2: ASTM pull-off test

The pull-off strength is computed based on the maximum indicated load, the instrument calibration data and the original stressed surface area. Debonding of the adhered plate from the FRP is an indication of improper surface preparation or an under-strength

adhesive. These modes of failure yield an invalid test result. The ASTM modes of failure are illustrated in Figure 2-3.

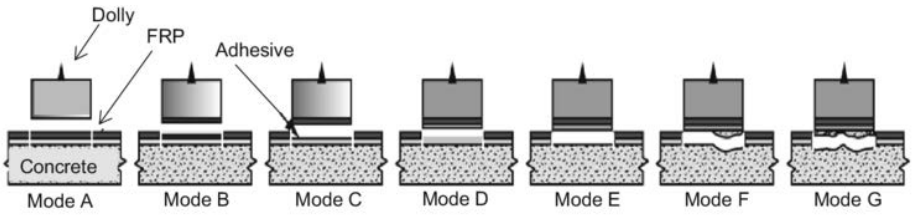

Figure 2-3: ASTM pull-off test modes of failure [ASTM D7522/D7522M-15, 2015]

The ASTM pull-off test method has the following advantages: quick and economic, on-site testing with only minimal damage to the FRP and immediate test results. A field assessment of the FRP strengthening and the evaluation of the long-term behavior of FRP is helpful in better understanding of FRP as a concrete strengthening material. The ASTM pull-off test results are used to evaluate the performance of FRP as a strengthening material [Yazdani et al., 2016].

Witness panel test

The witness panel test consists of small samples of the composite part. The panels are fabricated on the job site using the same materials prepared for the application of the FRP to the structure, and under the same conditions that are found on the job site. Fully cured panels should be sent to a qualified testing laboratory to validate the FRP material properties with those specified in the design.

Once the specimen has been properly prepared, aligned, measured, gripped and tested, the witness panel test follows the ASTM 2014 standard and provides the true tensile properties of the FRP, such as modulus, rupture strain, and rupture strength. The failure

occurs when the fiber reaches the rupture strain. Reasons for the failure occurring prior to the strain reaching the rupture strain point could be due to the existence of bending or local stress concentration arising from factors such as misalignment and improper gripping. It is because of this reasoning that the rupture strain obtained from the witness panel represents the lower bound of the actual rupture strain if no flaws exist in the procedure.

The two tests recommended by ACI 440 lack the ability to detect the overall quality of the bond. The two tests are destructive, localized and could not be used regularly to monitor the condition of the bond. Some defects, cracks and voids may be unnoticed. Consequently, different authors have developed nondestructive methods to assess the quality of the FRP concrete bond.

Non-destructive testing

The reliability of non-destructive testing (NDT) techniques to detect and assess defects in FRP rehabilitated concrete structures is highly dependent upon their ability to detect critical defect types and on the practicality of the method. Whereas some methods require very little equipment that could lead to the defect size, depth, and type being questionable, other methods are extremely powerful but have requirements such as power supply, experience, and ample space that are impractical in the field. The following sections discuss different types of applicable NDT techniques along with the advantages and disadvantages.

Visual inspection

The visual inspection is considered as the primary method of inspection. It is recommended by codes. In this technique, personnel uses their own judgment to determine whether a procedure was followed correctly. It is a simple technique and can be used to determine obvious surface defects. Advantages to visual inspection include instantaneous data results, economy and low equipment cost. Disadvantages include the limitation of the human eye, mistakes made by human misinterpretation, and inspection of only the structure's surface. Therefore, this method is a cheap yet unreliable method.

Mechanical and acoustic vibration

One of the most common types of mechanical vibration evaluation is the tap test. Tap testing is an NDE practice used on bridge decks that is fast, low cost and effective for inspecting FRP strengthened structures. To perform the test, an inspector taps the surface of the area of interest with a coin or hammer and then listens for any distinctive change in frequency which marks where a void or delamination exists. Tap testing is fast, low cost, and provides an effective way to inspect composites for delamination. Drawbacks to this test include the presence of ambient noise which could result in the erroneous interpretation of the defects, can only be used to identify near surface defects and measures only at the point of application.

The rebound hammer test is classified as a mechanical vibration test. It is not usually considered for testing of FRP strengthened structures. The rebound hammer provides an empirical measure of the hardness of a localized area of the concrete surface. The rebound principle is well established and widely accepted for assessment of concrete uniformity and determination of areas of poor quality or deterioration. The hammer works by impacting a spring-loaded mass on a plunger which is in contact with the surface. The

distance which the mass rebounds is a measure of the hardness of the surface, for which correlation graphs are available [Bungey et al. 2006]. The advantages of the method are that it gives a quick idea of the quality of concrete, it is simple to operate, requires a low skill level, light and has a low cost of operation. The disadvantages are that the test is highly localized and the reading is sensitive to local variations in the concrete, especially aggregate particles near the surface. The surface must be smooth, clean and dry.

Radiographic imaging

Radiography is an NDT technique where an image is produced from the radiation passing through the object resulting in a light emitted from the interaction. These lights or fluorescent elements form the image that is seen in the film radiography. Any defects or damage present within the specimen are superimposed on a two-dimensional (2D) image, without any indication of the depth of the flaw. Lighter and brighter images mean less dense section as illustrated in Figure 2-4.

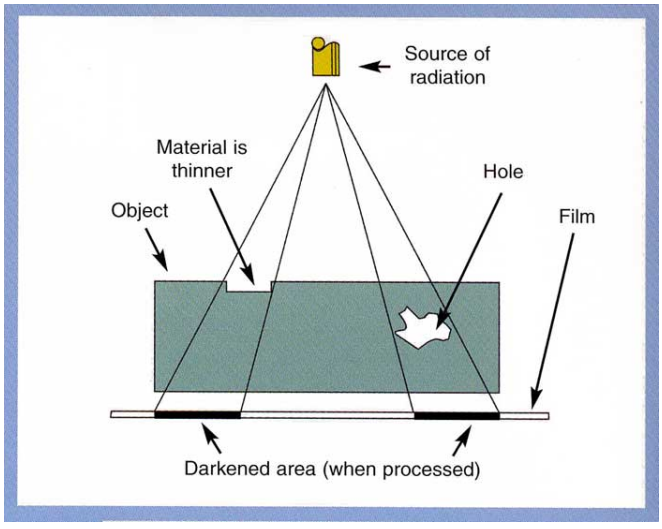

Figure 2-4: Concept of radiographic inspection

[https://www.ndeed.org/GeneralResources/MethodSummary/RT1.jpg]

To detect long cracks, the best-desired orientation must be in a position such that the photon ray will penetrate the maximum distance of the crack. If the orientation is perpendicular to the crack, the penetration region would be very small and the result of the recorded image would likely reveal no vital information [NSF, 2009]. Radiography offers some advantages, especially during in-situ testing. For starters, the test produces instantaneous and extremely accurate images of the radiographed section. It also works with any form of radiation including x-ray, gamma, or neutron radiation. Additionally, no surface contact is required; therefore, almost any geometric shape can be inspected. Disadvantages to Radiography include sensitivity, high cost, the need for high energy sources, and safety precautions due to radiation.

Optical methods

Optical NDT uses light as the measurement tool. These methods measure the change in the strain which requires the application of loads on the structure as illustrated in Figure 2-5. Therefore it is not considered as classical NDE method. The most common methods are interferometry, holography and shearography. Optical NDT can produce qualitative (defect detection) and quantitative (surface displacement maps or stress/strain analysis) results.

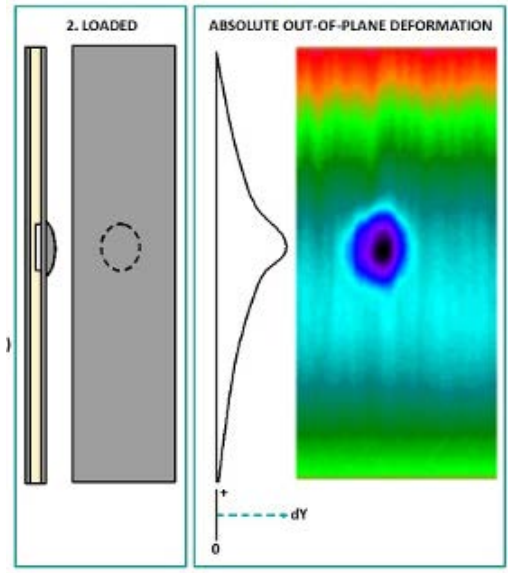

Figure 2-5: Optical method [http://www.nanotech.jo]

Optical techniques can provide information about not only the location of a defect on the object surface but also the effect of the defect on the object's behavior [Karbhari et al. 2005]. The major disadvantage is the need to perform these type of tests in a laboratory due to their complexity, sensitivity to external factors and stability requirements. All these optical methods are limited to the surface inspection. This puts a limitation on the detectability of the defects that are of insufficient size.

Thermographic imaging

Infrared Thermography is a non-contact sensing method. It involves the measurement of surface temperatures as heat flows to and from an object. The Infrared Thermography technique is one method that has been used for many years to scan aerospace structures, particularly to detect and characterize delamination in carbon/epoxy composites.

Usually, this technique consists of heating the surface of a structure during a period and measuring the temperature distribution of the sample with the use of an infrared camera. For large structures such as bridge decks and highways, solar heating is often sufficient. The Infrared camera technologies are broken down into two categories: thermal detectors and quantum detectors. A common type of thermal detector is an uncooled microbolometer made of a metal or semiconductor material. These typically have lower cost and a broader IR spectral response than quantum detectors. Quantum detectors are based on the change of state of electrons in a crystal structure reacting to incident photons. These detectors are generally faster and more sensitive than thermal detectors. However, they require cooling, sometimes down to very low temperatures.

The thermal detector type infrared camera will produce images of pixels and composed of uncooled microbolometer detectors allowing to see temperature differences. The principle is that the camera monitors the flow of heat from the surface which is affected by internal flaws such as disbands, cracks or voids. Solid bonds will cause rapid heat dissipation through the material, while areas with defects will retain the heat for longer periods of time. The method behind this principle is that the presence of subsurface anomalies will alter the rate of diffusion with respect to the surrounding area. As such, entrapped pockets or air will retain heat longer and serve as hot spots. This phenomenon is due to the low thermal conductivity of air as well as the high heat flow rate in the surrounding material [Karbhari et al. 2005]. Advantages of this test include ease of accessibility due to in-situ testing and short inspection time. Difficulties include the differentiation in the thermal contrast between the good and defective regions. The depth and type of defect that can be detected are limited.

Hu et al. (2002) used the infrared thermography technique for the detection of voids of size 0.6 in.-1.1 in (16 – 30 mm) embedded between the interface of FRP and concrete using cuts from plastic pipes. The test was able to detect defects even though the distance between the surface of the sample and infrared camera lens was increased to 65 ft. [Hu et al. 2002].

Schroeder et al. (2002) in applications to automotive industry, proposed a thermal non-destructive test (NDT) method using pulsed thermography to evaluate and assess the bond quality in adhesively bonded composites. The test was able to locate the mechanical damage to the composites, identifying the impact of any damage not visible.

Halabe et al. (2003) used infrared thermography to determine delaminations in FRP composite members. Two types of glass fiber reinforced polymer (GFRP) composites were tested. The test consisted of box sections of four different specimens containing delaminations of different sizes. The delaminations with different dimensions were inserted in these box sections. The delaminations were made by joining two polypropylene sheets with an enclosed air pocket in between them and the small strips were glued along the boundary in order to enclose an air pocket in between the two sheets. Finally, for trapping the air inside, the delaminations were sealed in between two latex sheets and then the delaminations were inserted inside the FRP specimens. The test successfully identified the void and delaminations as illustrated in Figure 2-6 [Halabe et al. 2003].

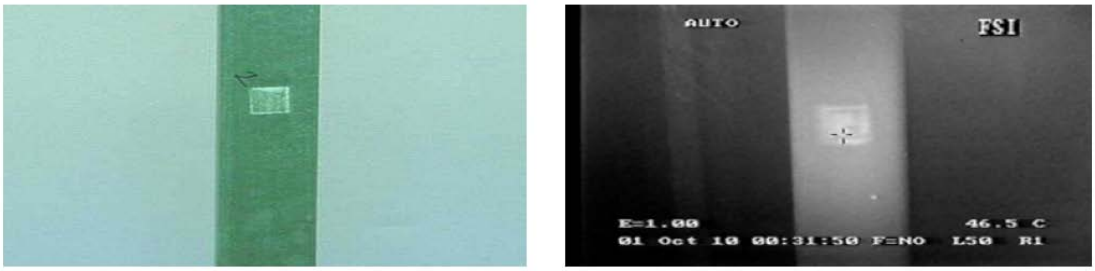

Figure 2-6: Grayscale infrared image [Halabe et al. 2003]

Monica et al. (2003) used a controlled-flaw specimen to study the response of different materials embedded into the concrete to heat. Eight ‘‘flaws’’ were created by placing different materials at the interface between the concrete and the CFRP laminate. The results showed that all simulated flaws could be detected and that the low-conductivity fabric material gave a response similar to that of an air void as illustrated in Figure 2-7 [Monica et al. 2003].

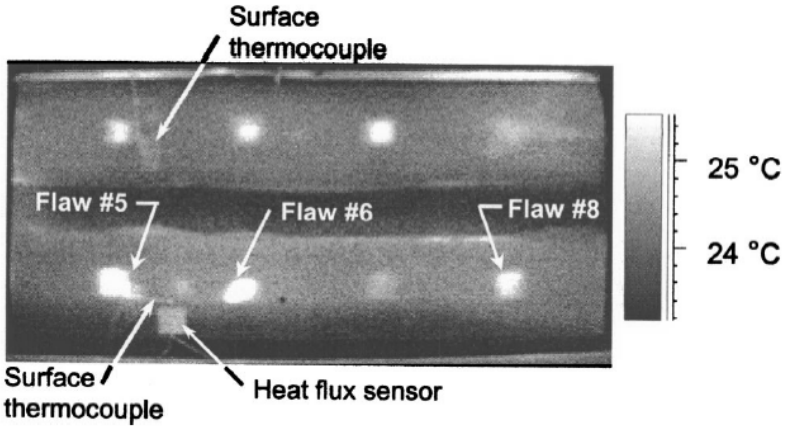

Figure 2-7: Infrared image of concrete sample with embedded flaws [Monica et al. 2003]

Meola et al. (2004) utilized thermographic technique to conclude that carbon fibers which have higher thermal properties permit the inspection of deeper material layers compared to glass fibers, and the defects composed of two superimposed thin foils of Teflon could be identified clearly using infrared images [Meola et al. 2004].

Galietti et al. (2007) investigated the possibility to detect defect embedded using two bonded foils of Teflon. The test identified the presence and dimension of the defects hidden in the interface between the concrete and FRP. The results show that two defects present at the same time can be wrongly interpreted [Galietti et al. 2007].

Taillade et al. (2012) used infrared camera test performed on an FRP-strengthened concrete sample containing calibrated defect created by inserting polytetrafluoroethylene (PTFE) discs to detect the defect depth and size. The test was successful in detecting and assessing the depth of the bond defects as illustrated in Figure 2-8. Defects were located between concrete and external FRP or between two layers of FRP [Taillade et al. 2012].

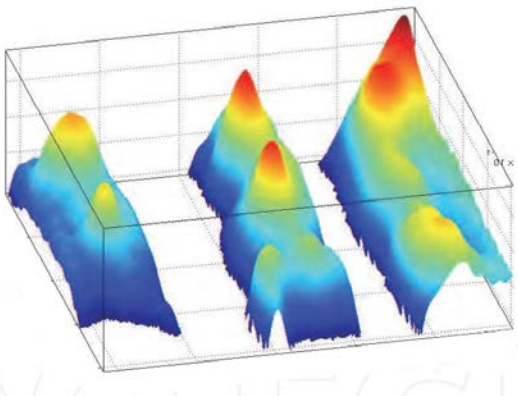

Figure 2-8: 3D view of thermal image after heating [Taillade et al. 2012]

Based on the literature review, it can be concluded that infrared thermography is a potentially powerful tool for inspection of concrete structures rehabilitated with FRP laminates. The majority of the study to investigate the quality of the bond was concerned of locating the size and depth of the voids. It is worth noting that, in most of these studies the voids were introduced by embedding air encased in some sort of outer casing which is not the case in most of the concrete structures.

Acoustic emission

Acoustic Emission (AE) uses elastic waves that are produced by moving dislocations, cracks, fiber breaks or debonding for defect detection and analysis of structures. Sensors are used to record the waves emitted when a structure is subjected to external load or temperature. In composite materials, matrix cracking and fiber breakage and debonding contribute to acoustic emissions [Degala et al. 2009]. This method is not considered as classical NDE method as it requires an application of loads and produces cracks and strain in the original structure. AE has been used in many industrial applications such as assessing structural integrity, detecting flaws, testing for leaks or monitoring weld quality and also used extensively as a research tool.

Advantages of AE include fast and complete volumetric inspection using multiple sensors. Drawbacks of AE testing include the possibility of flaws remaining undetected due to insufficient loading, resulting in a value not high enough to cause an acoustic event. Another drawback of AE comes from environments that have load and noisy nature which contribute extraneous noise to the signals.

Gostautas et al. (2005) investigated the performance of full-scale FRP bridge deck panel using the acoustic emission method. The test proved to be a useful tool for identification

of failure criteria associated with the initiation of permanent damage [Gostautas et al. 2005].

Ultrasonic methods

Ultrasound is acoustic energy in the form of waves having a frequency above the human hearing range. Ultrasound inspection methods are powerful tools for nondestructive testing and are widely used in the industry. In ultrasonic testing, stress waves are injected into the material or component to be examined and then the transmitted/reflected beams are monitored.

Ultrasonic pulse velocity UPV is one of the most popular ultrasonic methods. In contrast to the AE tests where elastic waves are generated through loading, in the ultrasonic pulse velocity (UPV) tests, a pulse signal of high-frequency sound energy is sent traveling through the structure to evaluate its condition. This inspection can be used for assessment of cracks, delamination, flaw detection [Mirmiran et al. 2001]. A typical Ultrasonic Testing inspection system consists of several functional units, such as the pulser/receiver, transducer, and display devices. Discontinuities in the structure (such as cracks) will cause the wave path to be reflected back. This energy is then transformed into an electrical signal by the transducer and displayed on the screen [NSF, 2009]. Advantages of the UPV test include instantaneous results, minimal preparation, the production of detailed results and high accuracy. Limitations of the UPV test include accessibility to transmit ultrasound, proper required training, and only suitable for homogenous materials.

Doyum et al. (2002) in application to aircraft, used Ultrasonic Scanning System which is a computer controlled ultrasonic testing and data collection system for finding defects created using Teflon strip in honeycomb composite structures after immersing the

samples in water. The ultrasonic method identified the size of most of the defects [Doyum et al. 2002].

Roth et al. (2003) in application to aircraft, studied an ultrasonic guided wave scan technique to distinguish various flaws in ceramic composites. The test shows that delamination, density variation, and crack location could be identified from the images obtained from ultrasonic test parameters [Roth et al. 2003].

Hosur et al. (2004) in application to aircraft, used the pulse-echo immersion ultrasonic technique to evaluate the damage due to high-velocity impact loading in FRP composites. The research identifies and compares the damaged area of each sample using ultrasonic C-scan images [Hosur et al. (2004].

Ribolla et al. (2016) used the ultrasound method to detect the debonding between FRP and concrete. The test used the equivalent time length of the ultrasound wave as an indicator of the quantity of energy propagating through the bonding. The test concept is illustrated in Figure 2-9 [Ribolla et al. 2016].

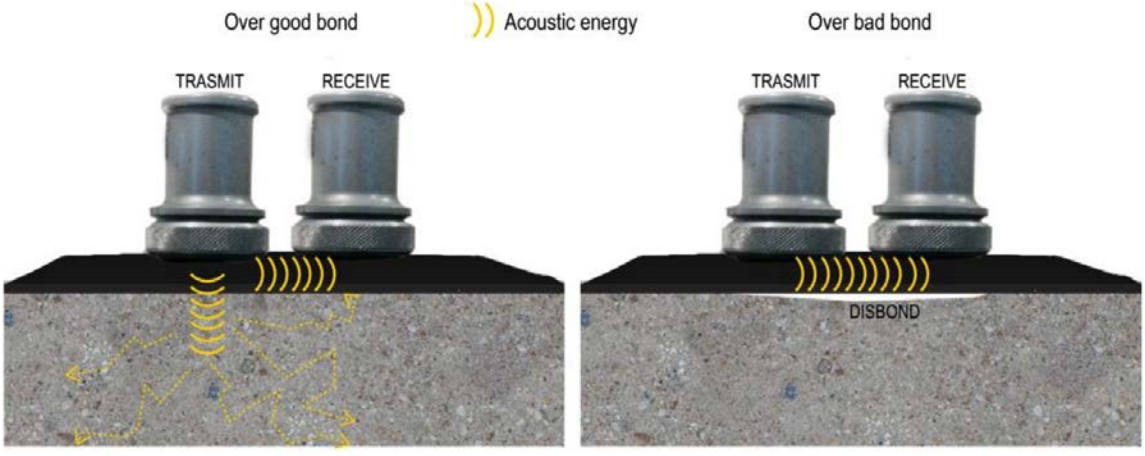

Figure 2-9: Bond testing using ultrasound method [Ribolla et al. 2016]

Impact echo is another ultrasonic method for NDT. This method is based on the use of impact generated stress waves that propagate through concrete and are reflected by internal flaws and external surfaces. A short impact produced by tapping a steel ball against the concrete surface is used to generate low-frequency stress waves that propagate in the structure and get reflected by flaws or other discontinuities. These surface displacements caused by wave reflections are recorded by a transducer that produces a voltage proportional to displacement, resulting in a voltage-time signal where it is transformed by a computer into a spectrum of amplitude versus frequency [Sansalone et al. 2003]. These variations in reflections are then used to identify and evaluate the integrity of the structure and to determine the location of flaws.

Another technique used for NDT is the Ultrasonic Tomography method. This technique consists of exciting an elastic wave in the concrete structure in order to determine location and size of defects, such as cracks, air voids or inclusions. Instrumentation features a multi-head antenna that generates 50 kHz ultrasonic pulses and is used for receiving and processing ultrasonic signals. F [Schabowicz, 2013].The methodology has been geared to locate defects in unilaterally accessible concrete members, determining their size and estimating the thickness of the members.

Nonlinear ultrasonic is a newer approach for NDE of material degradation that is helpful in detecting cracks at early stages. When there is a presence of micro-cracks in an elastic medium, the proportionality between an impinging ultrasonic wave and the corresponding elastic response of the medium occurs. Due to an increase of nonlinearity associated with increased damage, the goal of nonlinear ultrasonic methods is to extract the signature of the nonlinearity from the elastic response of the tested element to characterize damage progression [Antonaci et al., 2009].

Electromagnetic techniques

One of the popular electromagnetic techniques is the Eddy Current Test (ET). The eddy currents are created through electromagnetic induction. When alternating current is applied to the conductor, such as a coil or copper wire, a magnetic field is developed around the conductor. The magnetic field propagates as the current rises to a maximum level and collapses until the current is reduced to zero. When another electric conductor is brought close to the original one, a change in magnetic field occurs and current will induce in the second conductor [Laight et al. 1997]. When a flaw is introduced to the conductive material, the eddy currents are disrupted. The Eddy current method requires a conductive material. The Glass FRP is not conductive, therefore this method has limited application for the GFRP testing.

Another popular Electromagnetic technique is microwave based. It uses high-frequency electromagnetic energy ranging from a few hundred MHz to a few hundred GHz. Here, the material is tested by measuring various properties of the electromagnetic waves scattered by or transmitted through the test material [Jamil et al. 2012]. Dielectric spectroscopy is a fundamental technique that measures the dielectric properties of a medium as a function of frequency. The application allows for the prediction of parameters such as porosity and pore connectivity based on the interaction of an external field with the electric dipole moment, often expressed by permittivity [Raihan 2014]. Nuclear Magnetic Resonance (NMR) is a technique that studies the properties of water storage and transport. They also provide information about the porosity and water tightness of structures that allow for the determination of environmental durability problems at an early stage. [Dobman et al. 2002].

Ground penetrating radar

Ground Penetrating Radar (GPR) is a real-time NDT technique that uses high-frequency radio waves to investigate the features buried underground. This technique relies on an electromagnetic wave which is propagated into the material under investigation. The main components that make up the GPR include a waveform generator, a single transducer comprised of an emitting and receiving antenna, a signal processor and a data storage/display unit [Ekes, 2007]. A schematic of GPR is shown in Figure 2-10.

Figure 2-10: Ground Penetrating Radar (GPR)

The transmitter sends a signal into the ground. The transmitting signal gets reflected from the target and the reflected signal is received by the receiver antenna. The received data is then processed and displayed. A typical GPR system is shown in Fig. 2-11. GPR wave gets reflected if there is a new material in the path of propagation of the wave. The reflection wave is the function of the permittivity (ε), the magnetic permeability (μ) and the electrical conductivity (σ) of the reflection surface. A medium with high conductivity reduces the penetration of the GPR wave because it absorbs the radar signal. The

magnetic permeability is very low for most of the engineering materials. The GPR signal is most susceptible to the permittivity of the medium.

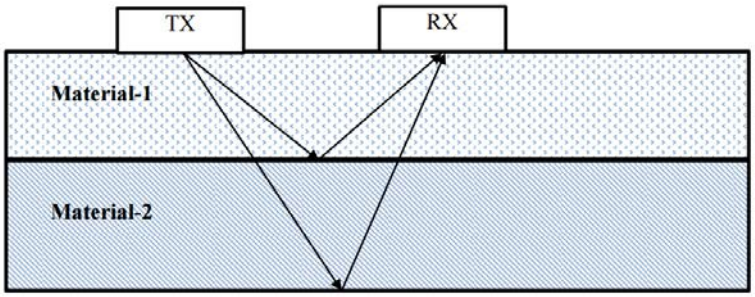

Figure 2-11: Schematic diagram of generic GPR system

This reflected signal is recorded by the receiver antenna of the GPR system. The amplitude and wavelength and the travel time of the signal are recorded by GPR. This recorded information consists of valuable information about the reflection surface or target.

The output signal of GPR scan possesses valuable information about the subsurface. The output of the GPR scan is not the real image of the subsurface. Rather it is a type of signature depends on the size, shape and dielectric constant of the target. GPR scan data can be collected and presented in one, two and three dimensions (A-scan, B-scan and C-scan) as shown in the Fig. 2-12.

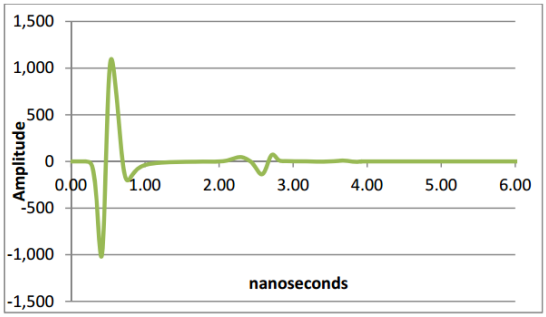

Figure 2-12a GPR A scan

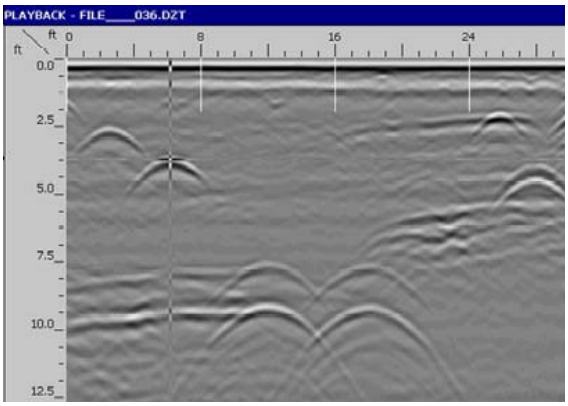

Figure 2-12b GPR B scan

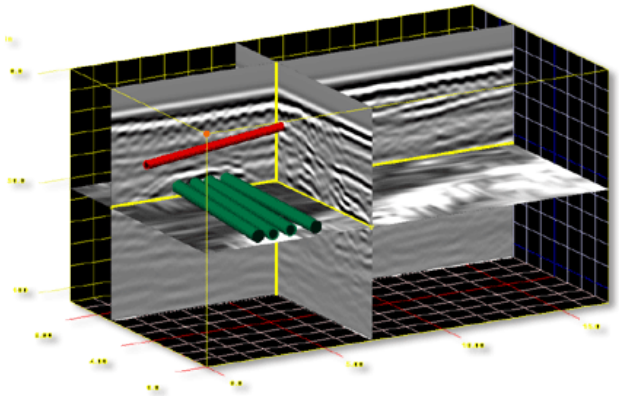

Figure 2-12c GPR C scan

Dutta (2006) used GPR technique using 1.5 GHz ground-coupled antenna for detecting embedded subsurface voids of sizes 3'' x 3'', 2'' x 2'' and 1.4'' x 1.4'' in FRP wrapped concrete cylinders. While the water filled voids showed up very prominently in the GPR scan, the technique was unable to detect the air-filled voids [Dutta, 2006].

Hing (2006) used GPR technique utilizing both 1.5 GHz ground coupled for detecting voids in FRP bridge deck. This study showed that the 1.5 GHz ground-coupled antenna was successful in detecting water filled defects of small dimensions as illustrated in Figure 2-13. The 1.5 GHz ground-coupled antenna proved to be an excellent tool for detecting subsurface water-filled voids of size as small as 2" x 2" x 0.06" [Hing et al. 2006].

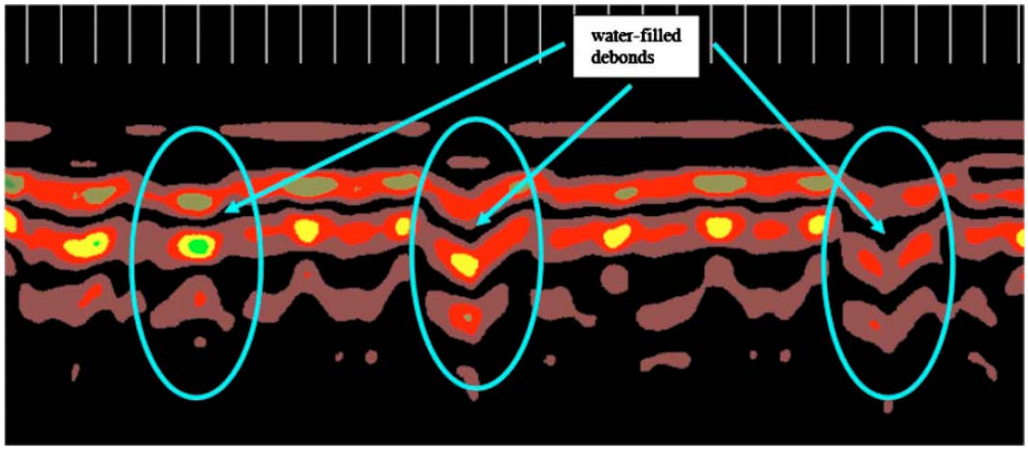

Figure 2-13: Results of GPR test showing smaller sized WF voids [Hing et al. 2006]

Limitation of previous study and significance of the research

Most of these NDE methods involve techniques that are adequate for limited characterization (location and size only). In most of these studies, the voids were introduced by embedding air encased in some sort of outer casing which is not the case in most of the concrete structures. More research is needed to quantify the bond strength and ensure the quality of the overall strengthened structure.

This research aims to develop reliable and convenient procedures to be followed to quantitatively evaluate the FRP-concrete bond strength using non-destructive methods. The proposed concept consists of using the NDE approach to obtain NDE test parameters from test samples and then to correlate the parameters with the actual bond strengths. Various parameters affecting the bond strength, such as surface roughness, voids, epoxy type and thickness, and FRP type, were considered. The objective of the research is to develop quantitative relationships between each of the parameters in the study and the associated bond strengths. The following NDT methods were used: ground generating radar (GPR), ultrasound tomography, infrared camera and Schmidt hammer.

The relationships will be very useful to structural engineers in estimating the in-service bond conditions of applied FRP laminate and estimating the expected strength of the overall flexural strength of structural members.

Chapter 3

DESIGN OF EXPERIMENT AND SAMPLES CONSTRUCTION

Introduction

The purpose of this research is to evaluate bond strength between the concrete and the FRP. To achieve this purpose, various parameters affecting the bond strength, such as surface roughness, voids, epoxy type and thickness, and FRP type, were considered. This chapter describes the design consideration and procedures of the test samples to incorporate all the parameters in the study. The following sections describe the method used to determine the required number of samples for the study, instrumentation plan and samples preparation.

Design of Experiment

The first step in the design is to determine the number of required samples that incorporates all the parameters considered in the study. Since that the interaction between the parameters could not be ignored, the simple approach of changing only one parameter at a time is not suitable for this test. The design of the experiment is necessary for this test for a sound statistical approach is required to consider the interaction between all the parameters.

The choice of an experimental design depends on the objectives of the experiment, the number of parameters, and the levels of these parameters. With 6 parameters and the primary purpose of the experiment is to select the effect of each parameter on the bond strength. The “Factorial Design” method was appropriate for this study [NIST/SEMATECH handbook, 2012].

Due to limitations on space, cost and time, the “Full Factorial” design with 128 samples was not possible. Therefore, the “Fractional factorial” method was selected. Where, in the Full Factorial method the interactions between all the parameters are considered while in

the Fractional Factorial method, the effect of several parameters is grouped together to reduce the total number of samples in a process called confounding [NIST/SEMATECH handbook, 2012].

The Fractional Factorial method could be used in many resolutions depending on the number of parameters grouped together in one sample. The selection of the Fractional Factorial resolution depends on limitations imposed on the test due to cost, time or any outside factors. For this test Fractional Factorial method resolution 4 was recommended with only two parameters confounded at a time. Using the Fractional Factorial method resolution 4 for 6 parameters each having two levels (High and low) results in 16 required samples for the research as illustrated in Table 3-1.

Table 3-1: Fractional Factorial with 6 parameters having two levels [NIST/SEMATECH handbook, 2012]

X1	***X2***	***X3***	***X4***	***X5***	***X6***
-1	-1	-1	-1	-1	-1
1	-1	-1	-1	1	-1
-1	1	-1	-1	1	1
1	1	-1	-1	-1	1
-1	-1	1	-1	1	1
1	-1	1	-1	-1	1
-1	1	1	-1	-1	-1
1	1	1	-1	1	-1
-1	-1	-1	1	-1	1
1	-1	-1	1	1	1
-1	1	-1	1	1	-1

1	1	-1	1	-1	-1
-1	-1	1	1	1	-1
1	-1	1	1	-1	-1
-1	1	1	1	-1	1
1	1	1	1	1	1

Where X1 to X6 represents the parameters considered. The (-1) refers to the parameter in its low level and the (+1) refers to the parameter in its high level.

For this test, replicability is important to reduce any noise and reduce the chance of false conclusions. Hence, two replicates of the same sample are used, resulting in a total of 32 samples.

The first parameter considered to have an effect on the bond strength is the FRP type. Two different FRP types were selected in this research. The first type “Sika Wrap Hex 117C” and the second type “Sika Wrap Hex 103C”. The cured laminate properties for the “Sika Wrap Hex 117C” are as follows:

- Design Values Tensile Strength: 1.05 × 105 psi (724 MPa)
- Modulus of Elasticity: 8.2 × 106 psi (56,500 MPa)
- Elongation at Break: 1.0%
- Thickness: 0.02 in. (0.51 mm)

While “Sika Wrap Hex 103C” cured laminate properties are:

- Design Values Tensile Strength: 1.609 × 105 psi (1110 MPa)
- Modulus of Elasticity: 10.39 × 106 psi (71,700 MPa)
- Elongation at Break: 1.45%

- Thickness: 0.04 in. (1 mm)

The adhesive layer is considered to have a considerable impact on the bond strength. Therefore, two parameters are assigned to study the adhesive layer. The first parameter is the Epoxy type and the second is the No. of Epoxy layer used. For the Epoxy type, “Sikadur 300” as type I and “Sikadur 330” as type II. For the second parameter, the epoxy “Sikadur 31” was applied to the concrete surface in addition to the “Sikadur 300” or the “Sikadur 330” to form the second layer. The properties of the three adhesive types used in this research are as follows:

- “Sikadur 300”:
  - Tensile Strength: 8,000 psi (55 MPa)
  - Elongation at Break: 3%
  - Flexural Strength: 11,500 psi (79 MPa)
  - Flexural Modulus: 5 x 105 psi (3,450 MPa)
- “Sikadur 330”:
  - Tensile Strength: 4,900 psi (33.8 MPa)
  - Elongation at Break: 1.2%
  - Flexural Strength: 8,800 psi (60.6 MPa)
  - Flexural Modulus: 5.06 x 105 psi (3,489 MPa)
- “Sikadur 31”:
  - Tensile Strength: 3,300 psi (22.7 MPa)
  - Elongation at Break: 0.9%
  - Flexural Strength: 6,100 psi (42.0 MPa)
  - Flexural Modulus: 16.7 x 105 psi (11,52 MPa)

The friction between the concrete surface and the FRP layer is one of the forces contributing to the bond strength. The surface roughness of the concrete surface is considered to increase the friction and consequently increase the bond strength. To study the effect of the surface roughness and to quantify its effect, two types of surface roughness are considered in this research. The two types selected are classified based on the method used to achieve the surface roughness, the first type is using sandblasting, in this method the surface profile of the beam is prepared to a minimum of concrete surface profile (CSP) 3 as defined by the ICRI-surface-profile chips. While the second method using hand grinding, in this method the surface profile of the beam is prepared to a maximum of concrete surface profile (CSP) 2.

The last two parameters considered in this research, study quality of the FRP application in the field as of the presence of any bubbles or voids under the FRP surface and the effect of these imperfections on the total bond strength. The two parameters consider the presence of voids of different sizes. For the first parameter, two voids of size 0.8 in × 0.8 in. side by side are present under the FRP layer. For the second parameter, two voids of size 1.6 in × 1.6 in. side by side are present under the FRP layer.

After assigning each of the before mentioned parameters to its corresponding Fractional Factorial level, the final experimental matrix is prepared as illustrated in Table 3-2.

Table 3-2: Experimental Matrix

DOE #	FRP type	Epoxy Nb. of layers	Epoxy type	Surface roughness	Voids 1	Voids 2	No.
1	Type I	Type I	Type I	Sandblasting	-	-	2
2	Type II	Type I	Type I	Sandblasting	2x0.8	-	2
3	Type I	Type II	Type I	Sandblasting	-	-	2
4	Type II	Type II	Type I	Sandblasting	-	2x1.6	2
5	Type I	Type I	Type II	Sandblasting	-	-	2
6	Type II	Type I	Type II	Sandblasting	-	2x1.6	2
7	Type I	Type II	Type II	Sandblasting	-	-	2
8	Type II	Type II	Type II	Sandblasting	2x0.8	-	2
9	Type I	Type I	Type I	Hand grinding	-	2x1.6	2
10	Type II	Type I	Type I	Hand grinding	-	-	2
11	Type I	Type II	Type I	Hand grinding	2x0.8	-	2
12	Type II	Type II	Type I	Hand grinding	-	-	2
13	Type I	Type I	Type II	Hand grinding	2x0.8	-	2
14	Type II	Type I	Type II	Hand grinding	-	-	2
15	Type I	Type II	Type II	Hand grinding	-	2x1.6	2
16	Type II	Type II	Type II	Hand grinding	-	-	2

Where, Epoxy type I: Sikadur 300 and Epoxy type II: Sikadur 330. FRP type I “Sika Wrap Hex 117C” and FRP type II “Sika Wrap Hex 103C”. The number of Epoxy Layers: type I “Sikadur 300” or “Sikadur 330” and Epoxy thickness type II “Sikadur 31” will be applied to

the concrete surface in addition to “Sikadur 300” or “Sikadur 330” that will be applied to the FRP to form the two layers.

The final step in the experimental design is randomization. The randomization is important to remove any potential biases or judgments. Each one of the samples in the experimental method was assigned a random number and then the table was sorted following the random assignment resulting in a fully random table.

Samples preparation

After the design of the experiment, the samples were designed taking into consideration various factors to come up with the optimum beam dimensions. The width of the beams was chosen as 8 in. (20.3 cm) which is enough to accommodate the wheels of the handheld cart for the scanning using the GPR, and also to have enough cover for the pull-off test. The depth and the length of the beams were selected following the ACI 440.2R-08 guidelines [ACI 440, 2008] to make sure that the failure is in the bond. The failure load for the control beams was calculated to be 14 kips which below the capacity of the available bending test machine. The design was based on concrete material with a compressive strength of 3.5 ksi (24.1 MPa). A notch was included in the mid-span of the concrete beam to ensure a failure at the bond during the bending test. The schematic of the beam is illustrated in Figure 3-1.

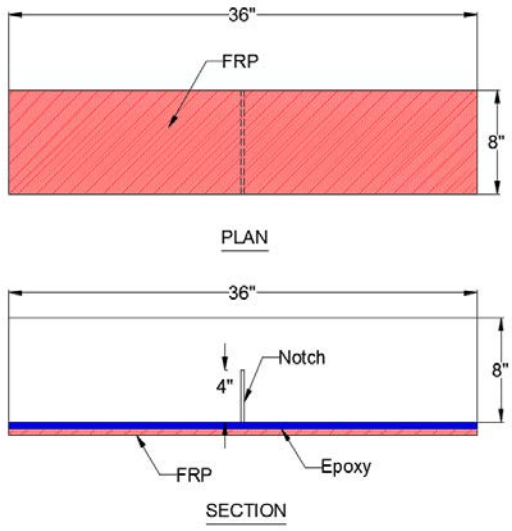

Figure 3-1: Schematic of the beam sample

The first stage in constructing the test samples was the formwork. The formwork for 32 beams with dimensions 8 in. × 8 in. × 36 in. using plywood was prepared. A cardboard of dimensions 4 in. × 8 in. × 0.022 in. was inserted in each sample to form a notch in the mid-span of the concrete sample. The formwork for the beams was covered to protect them from any weather effect. The Formwork preparation is illustrated in Figure 3-2.

Figure 3-2: Formwork Preparation

All specimens were cast horizontally, compacted, and trowel finished. Ready-mix concrete was used to make sure that all beams have the same properties. All the 32 beam samples were cast using normal weight concrete with a water-cement ratio of 0.40 and a maximum aggregate size of ¾ in.(19 mm) with a target 28-day compressive strength of 3.5 ksi (24.1 MPa). The casting of the samples is shown in Figure 3-3.

Figure 3-3: Casting of the concrete beams

To investigate the effect of voids present under the FRP layer on the bond strength, some predetermined voids were inserted at the surface of the concrete using foam cubes with the exact dimensions of the required voids as shown in Figure 3-4.

Figure 3-4: Voids preparation

After curing the foam pieces were easily removed. The specimens were covered with polythene sheets for 24 hours and then de-molded. The specimens were cured for 28 days by spraying water.

To investigate the effect of surface roughness on the bond strength, two degrees of surface preparation was selected as shown in Figure 3-5. Figure 3-5a illustrates the surface roughness achieved using hand grinding while Figure 3-5b illustrates the surface roughness using sandblasting.

Figure 3-5a: Concrete surface roughness (CSP) 2 using hand grinding

Figure 3-5b: Concrete surface roughness (CSP) 3 using sandblasting

The highest surface roughness was achieved using sandblasting as illustrated in Figure 3-6a. For this surface profile, the surface of the beams was prepared to a minimum concrete surface profile (CSP) 3 as defined by the ICRI-surface-profile chips. For the low surface roughness, the method of hand grinding using diamond discs was used as illustrated in Figure 3-6b.

Figure 3-6a: Concrete surface preparation using sandblasting

Figure 3-6b: Concrete surface preparation using hand grinding

The following step was the FRP Application. In this step, two types of epoxy were used to attach the FRP for specimens. For type I “Sikadur 300” and for type II “Sikadur 330” with tensile strength 55 MPa and 24.8 MPa respectively. Two types of FRP material were used for the specimens. For type I “Sika Wrap Hex 117C” and for type II “Sika Wrap Hex 103C”. The epoxy “Sikadur 31” (tensile strength 22.7 MPa) was applied to the concrete surface in addition to the “Sikadur 300” or the “Sikadur 330” to form the two layers.

The FRP was applied at an ambient temperature of 60 degrees Fahrenheit and in absence of direct light to prevent any undesirable problems with the epoxy. The temperature was cooling down to prevent the phenomena of outgassing of the concrete which might increase the voids under the FRP.

The first step in the application of FRP was cutting the FRP sheets. The FRP sheets come in rolls of 24 in. × 300 ft. while the required dimensions 8 in. × 3 ft. The FRP sheets were cut into the appropriate dimensions from both the “Sika Wrap Hex 117C” and the “Sika Wrap Hex 103C” rolls as shown in Figure 3-7.

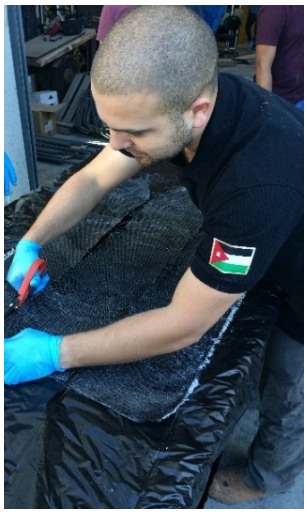

Figure 3-7: Cutting of the FRP

The next step, mixing the epoxy. The epoxy works as the adhesive layer between the FRP and the concrete and to form the cured laminate. Each of the three different types of epoxies were mixed by pouring the contents of part B to part A. The components were mixed thoroughly for 5 minutes for the “Sikadur 300” and “Sikadur 330” and for 3 minutes for the “Sikadur 31” on low using a paddle style mixer on low speed drill until uniformly blended. The mixing of the epoxy is illustrated in Figure 3-8.

Figure 3-8: Mixing of the Epoxy

Before applying the epoxy to the concrete surface, the surface was cleaned and dry. All the dust, laitance, grease, curing compounds, impregnation, waxes, and any other contaminants were removed. The voids were filled with towels to prevent any excess epoxy to fill the voids before applying the epoxy. After cleaning the surface, the “Sikadur 300” was applied to the FRP sheets to prepare the cured laminate. The next step was to apply the epoxy to the concrete surface as illustrated in Figure 3-9.

Figure 3-9: Applying the Epoxy

The final step in the FRP application was laying the FRP sheets on top of the concrete surface and making sure that the interface is free from any voids or imperfections as illustrated in Figure 3-10. To help remove any voids that might get entrapped below the FRP sheet, an aluminum roller was used to burst any entrapped voids.

Figure 3-10: FRP application

After attaching the FRP, the samples were left for 3 days to cure. The samples were covered with plastic sheets to protect them from any exposure to direct sun or rain. The cover was fixed at a height to prevent any contact with the epoxy while it is not fully cured. The test sample after applying the FRP is illustrated in Figure 3-11.

Figure 3-11: The concrete beams after attaching the FRP

Instrumentation Plan

In this section, the instrumentation plan for the bending test is presented. Two strain gages are attached to each beam. The first strain gage is attached to the FRP layer at mid-span to capture strain corresponding to the maximum tensile stress at the bottom of the beam section. The second strain gage is attached to the top of the concrete beam to record the strain corresponding to the maximum compressive strain at the top of the beam. An additional strain gage was attached to FRP layer at mid-span in only 16 of the 32 beams to verify the reading from the first strain gage. The instrumentation of the beam samples are illustrated in Figure 3-12.

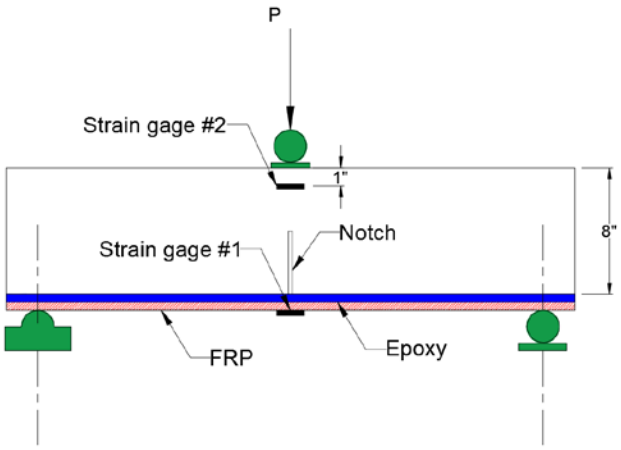

Figure 3-12: Strain gages location

To record the displacement at the mid-span during the bending test. Two displacement transducers (LVDT) were used. The LVDT were placed at both sides at the mid-span of the beam as in the side view shown in Figure 3-13.

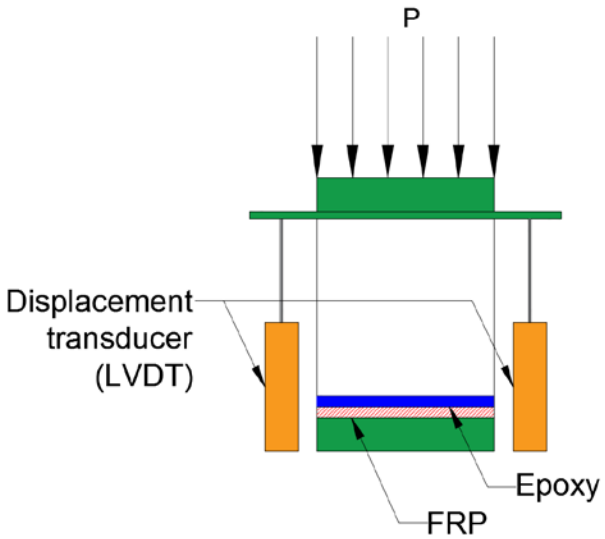

Figure 3-13: Displacement transducer location

Chapter 4

NON-DESTRUCTIVE TESTING

Introduction

In this chapter the capacity of the following NDE methods: ground generating radar (GPR), ultrasound tomography, infrared camera and Schmidt hammer on detecting the bond strength between the concrete and FRP is investigated. Each of the NDE methods is used to scan samples with various parameters that affect the bond strength, such as surface roughness, voids, epoxy type and thickness, and FRP type. The results of the NDE tests are presented.

Rebound Hammer Test

The Original Schmidt hammer was invented and introduced into the market in the 1950s. Since that time it has become the first and most widely used instrument for non-destructive estimation of concrete strength properties, asphalt, mortar, rock and paper. In this test, the “Silver Schmidt hammer” from “Proceq” is used as illustrated in Figure 4- 1. The silver Schmidt hammer principle is to measure the ratio between the rebound velocity and the impact velocity when the hammer hit the surface. The rebound is dependent on the hardness of the surface. The rebound value can be used to determine the bond strength between the concrete and the FRP.

Figure 4- 1: Schmidt hammer

Schmidt hammer defines the ratio between the rebound velocity and the impact velocity as the quotient value “Q”. The Q value is used in this test to compare the surface hardness of each sample. The surface hardness of each sample to be correlated with the overall bond strength.

Schmidt hammer test: In this test, six points were selected as illustrated in Figure 4- 2. The Q value (the ratio between the rebound velocity and the impact velocity) was recorded for the 6 points. This test was repeated 3 times. The Q value for each beam is the average of the 6×3 readings.

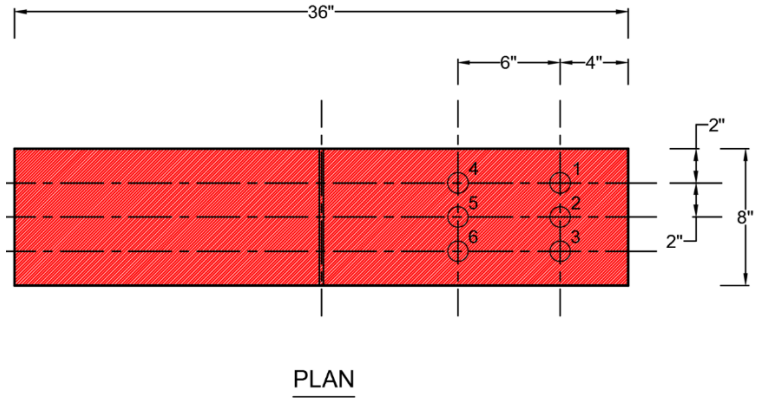

Figure 4- 2: Schmidt hammer test points

The first step in the test procedures was to mark the exact location of the points to be tested. To help with marking, a cardboard sheet was prepared by adding 6 holes at the required locations as illustrated in Figure 4- 3. After placing the cardboard over the sample, a marker pen was used to highlight the exact location of the test point.

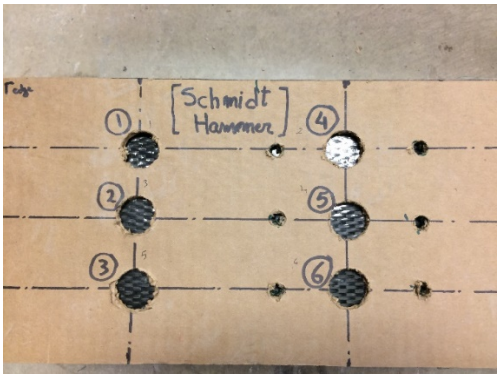

Figure 4- 3: Marking of the test points

The next step was using the Schmidt hammer device to record the Q value at each of the test points. The device was held perpendicular to the concrete surface. To perform the test the device was held steadily with both hands and pressed toward the beam surface until a sound of the hammer hitting the surface produce a loud noise as illustrated in Figure 4- 4. The Q value was recorded corresponding to each point of the test. This test was repeated three times for each sample.

Figure 4- 4: Schmidt hammer testing at the FRP surface

In order to compare the surface hardness of the FRP surface with the surface hardness of the concrete surface of each beam, additional test points were used to record the Q value from the concrete surface of the beam as shown in Figure 4- 5. Three points were used and the Q value at each of the points was recorded.

Figure 4- 5: Schmidt hammer testing at the concrete surface

After collecting the data using Schmidt hammer, the data are presented in form of a column chart as illustrated in Figure 4- 6. For each beam, four different series are presented. The first three series represent the Q value of the concrete surface for both replicates of the same beam type followed by the average value of both replicates. The last three series represent the Q value from the FRP surface for both replicates of the same beam type followed by the average value of both replicates. The chart indicates that the Q value increases for the FRP surface relative to the concrete surface in all the test samples.

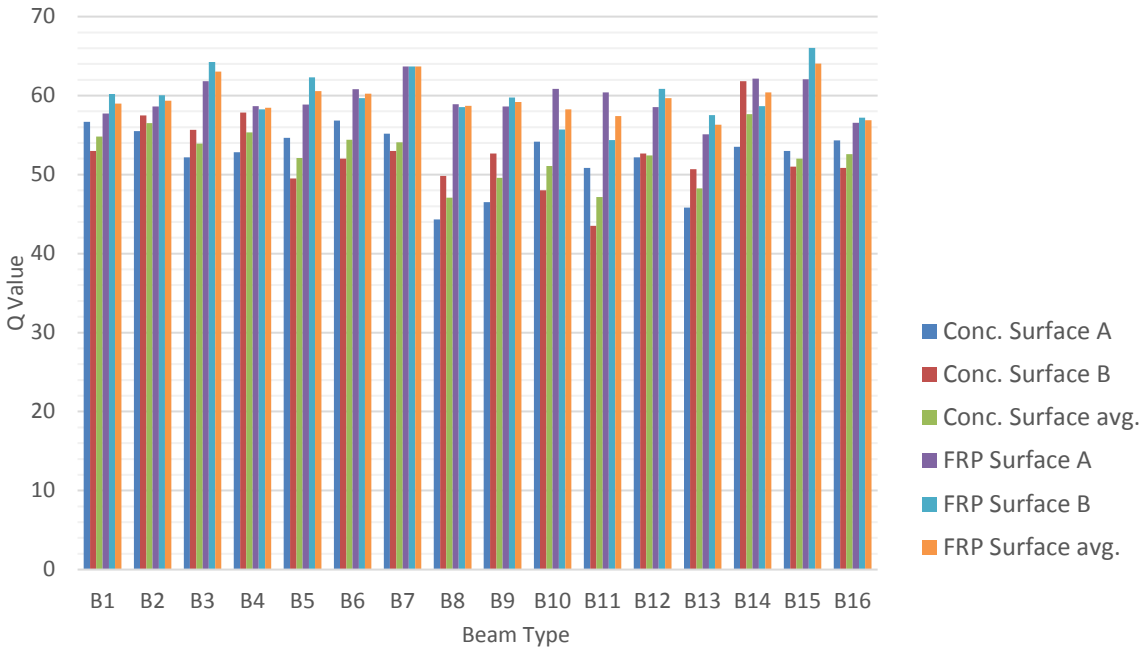

Figure 4- 6: Schmidt Hammer test data

To further analyze the data and determine the effect of each parameter on the Q value, Minitab software package for statistical analysis was used as illustrated in Figure 4- 7. The software provides several tools related to the design of experiment method. The inputs were selected to be the percentage change of Q value of the FRP surface relative to the Q value of the concrete surface. Following are some of the results of the design of experiment using Minitab software.

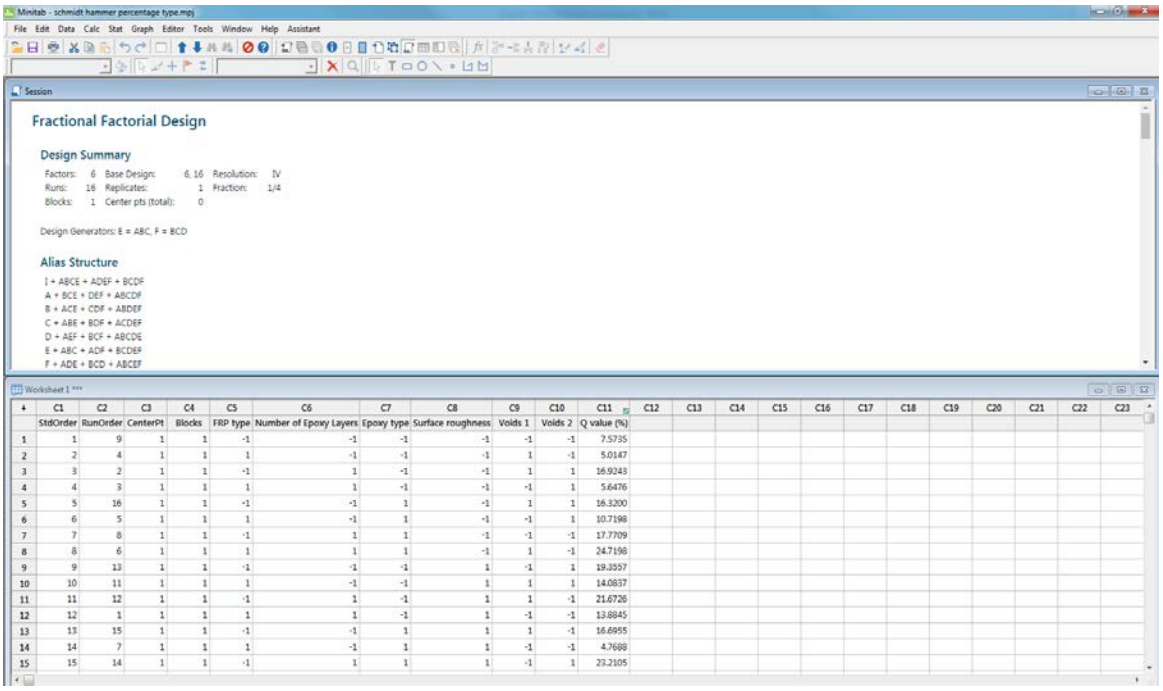

	C1	C2	C3	C4	C5	C6	C7	C8	C9	C10	C11	C12	C13	C14	C15	C16	C17	C18	C19	C20	C21	C22	C23
	StdOrder	RunOrder	CenterPt	Blocks	FRP type	Number of Epoxy Layers	Epoxy type	Surface roughness	Voids 1	Voids 2	Q value (%)												
1	1	9	1	1	-1	-1	-1	-1	-1	-1	7.5735												
2	2	4	1	1	1	-1	-1	-1	1	-1	5.0147												
3	3	2	1	1	-1	1	-1	-1	1	1	16.9243												
4	4	3	1	1	1	1	-1	-1	-1	1	5.6476												
5	5	16	1	1	-1	-1	1	-1	1	1	16.3200												
6	6	5	1	1	1	-1	1	-1	-1	1	10.7198												
7	7	8	1	1	-1	1	1	-1	-1	-1	17.7709												
8	8	6	1	1	1	1	1	-1	1	-1	24.7198												
9	9	13	1	1	-1	-1	-1	1	-1	1	19.3557												
10	10	11	1	1	1	-1	-1	1	1	1	14.0837												
11	11	12	1	1	-1	1	-1	1	1	-1	21.6726												
12	12	1	1	1	1	1	-1	1	-1	-1	13.8845												
13	13	15	1	1	-1	-1	1	1	1	-1	16.6955												
14	14	7	1	1	1	-1	1	1	-1	-1	4.7688												
15	15	14	1	1	-1	1	1	1	-1	1	23.2105												

Figure 4- 7: Minitab software for statistical analysis

The first step is plotting the data several ways to see if any trends or anomalies appear that would not be accounted for by the model. Figure 4- 8 examine the assumption that the residuals are approximately normally distributed, are independent, and have equal variances, Minitab generates four plots of the residuals: a normal probability plot, residuals versus the fitted values, histogram and a run-order plot of the residuals. The four charts show a large spread of the data and there does not appear to be a pattern to the residuals. The residuals do appear to have, at least approximately, a normal distribution.

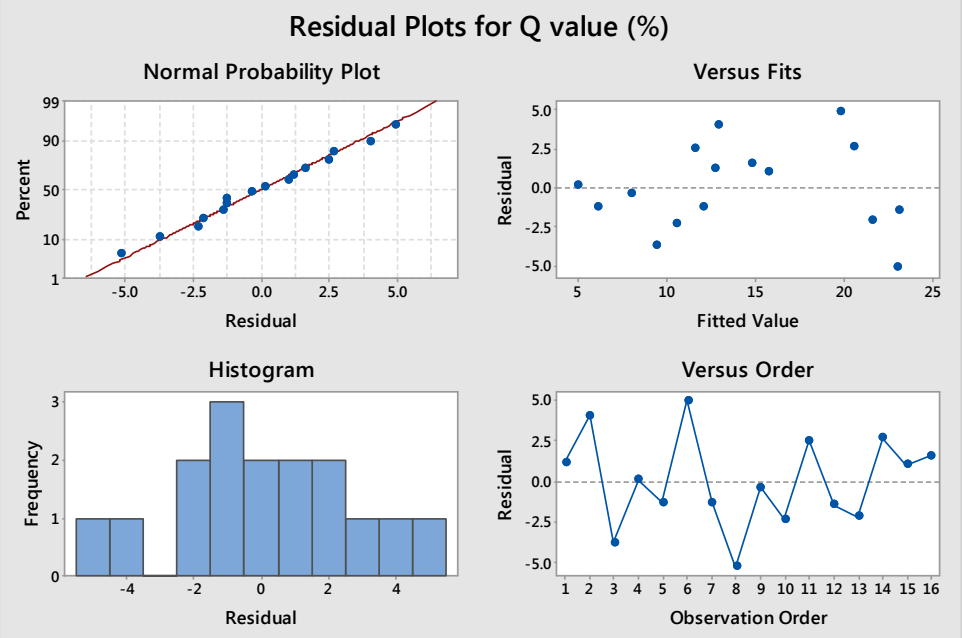

Figure 4- 8: Residual Plots for Q value (%)

Next step, to look at the plots of responses versus each parameter as presented in Figure 4- 9. The plot of the Q value (%) versus the FRP type shows that the Q value tends to decrease with the increase in the thickness of the FRP layer. The plot of the number of epoxy layers shows that adding an extra layer of Epoxy increase the Q value reading. For the Epoxy type, the chart shows that the Epoxy with higher viscosity tends to increase slightly the Q value. Finally, the sandblasting surface preparation with higher CSP tends to decrease slightly the Q value.

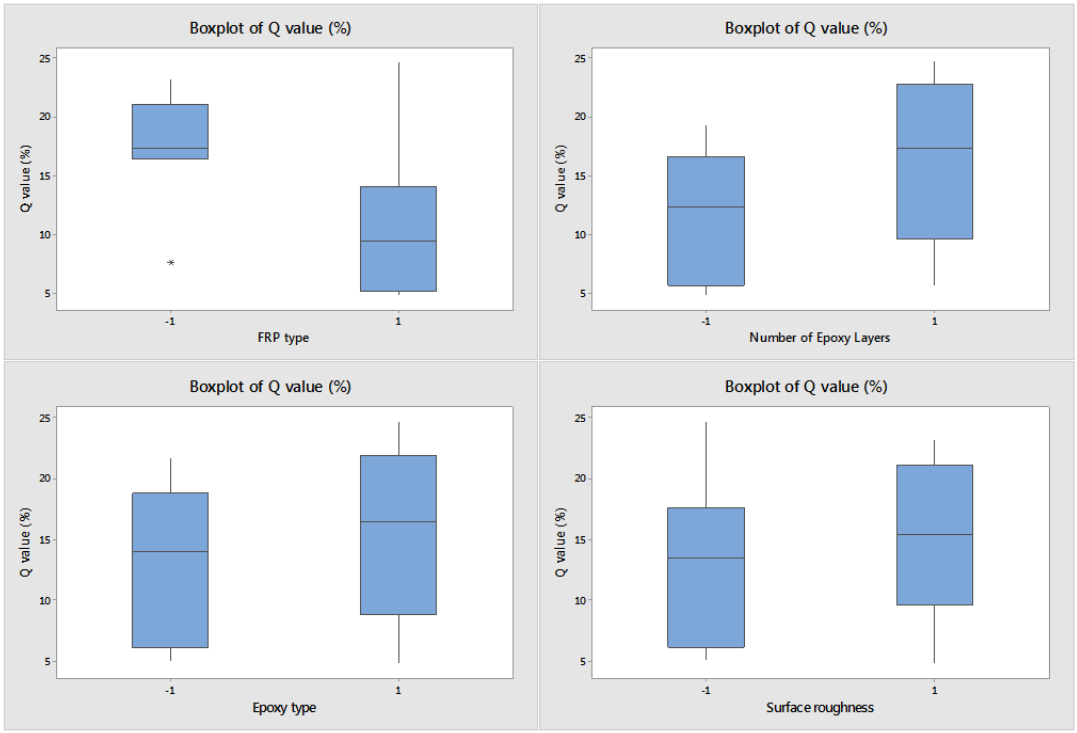

Figure 4- 9: Plots of responses versus each parameter

Minitab software presents the effect of each of the main parameters in a combined figure as illustrated in Figure 4- 10.

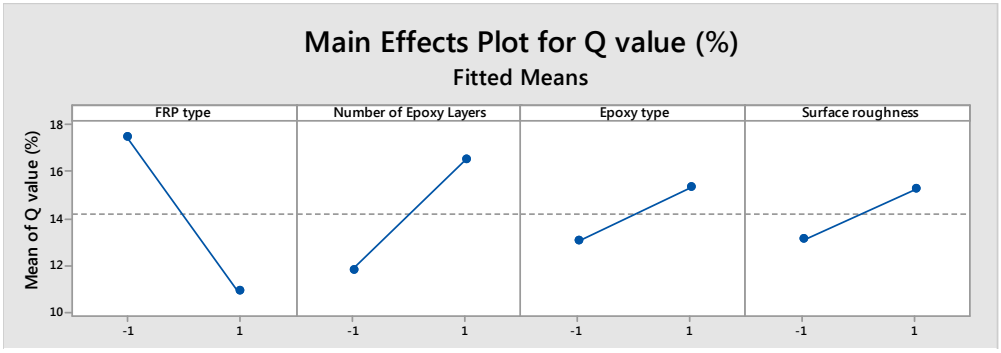

Figure 4- 10: Main Effect of the parameters

Since the interaction between each of the parameters is important for this study, the interaction plot is presented in Figure 4- 11. The interaction plot shows that there is no interaction between the FRP type and the number of Epoxy Layers used or the Epoxy type. The graph shows that there is a slight interaction between the number of Epoxy layer used and the Epoxy type. Also, there is a slight interaction between the number of Epoxy layer used and the surface roughness. The interaction between the FRP type and the surface roughness and the interaction between the Epoxy type and the surface roughness seems to be significant.

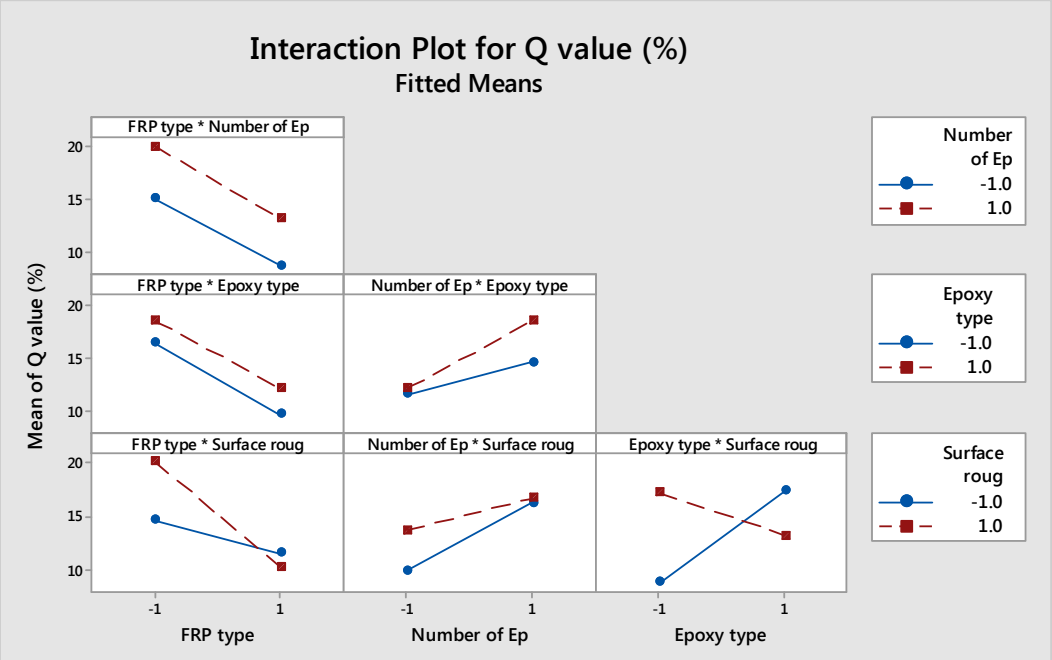

Figure 4- 11: Interaction plot for Q value

Finally, to study the significance of each of the main parameters and the interaction between them, the ANOVA table prepared by Minitab is presented in Table 4- 1. The

Table shows the FRP type along with the interaction between the Epoxy type the surface roughness have a significant effect on the Q value (%). The model has an R square of 82.9%.

Table 4- 1: Analysis of variance for the Schmidt hammer test

Source	DF	Adj SS	Adj MS	F-Value	P-Value
Model	10	528.560	52.856	2.29	0.186
Linear	4	299.275	74.819	3.24	0.114
FRP type	1	172.239	172.239	7.47	0.041
Number of Epoxy Layers	1	87.827	87.827	3.81	0.108
Epoxy type	1	20.786	20.786	0.90	0.386
Surface roughness	1	18.423	18.423	0.80	0.412
2-Way Interactions	6	229.285	38.214	1.66	0.298
FRP type*Number of Epoxy Layers	1	0.198	0.198	0.01	0.930
FRP type*Epoxy type	1	0.105	0.105	0.00	0.949
FRP type*Surface roughness	1	47.343	47.343	2.05	0.211
Number of Epoxy Layers*Epoxy type	1	11.029	11.029	0.48	0.520
Number of Epoxy Layers*Surface roughness	1	11.194	11.194	0.49	0.517
Epoxy type*Surface roughness	1	159.417	159.417	6.91	0.047
Error	5	115.323	23.065		
Total	15	643.883			

S	R-sq	R-sq(adj)	R-sq(pred)
4.80257	82.09%	46.27%	0.00%

The model prepared by Minitab present an equation that could be used in estimating the expected Q value for a specific beam. The estimated Q value is useful in the evaluation of the FRP application process. A Q value can provide a base for quality inspection and assurance. The equation for estimating the Q value is presented as follows.

$$\text{Q value (\%)} = 14.16 - 3.28\,(\text{FRP type}) + 2.34\,(\text{Nb. of Epoxy Layers}) + 1.14\,(\text{Epoxy type}) + 1.07\,(\text{Surface Roughness}) - 0.11\,(\text{FRP type} * \text{Nb. of Epoxy Layers}) + 0.08\,(\text{FRP type} * \text{Epoxy type}) - 1.72\,(\text{FRP type} * \text{Surface Roughness}) + 0.83\,(\text{Nb. of Epoxy Layers} * \text{Epoxy type}) - 0.84\,(\text{Nb. of Epoxy Layers} * \text{Surface roughness}) - 3.16\,(\text{Epoxy type} * \text{Surface Roughness}) \quad \text{Eq. (4-1)}$$

Where, FRP type is -1 for FRP type I and +1 for FRP type II. Similarly, for each parameter in the previous equation, a value of -1 is assigned to the type I and a value of +1 is assigned to type II.

A separate study was undertaken to identify the effect of the voids and delamination of the Q value of the Schmidt hammer test. In this section, Schmidt hammer device was used on several voids embedded below the FRP surface to study the effect of voids on the Q value. Also, cured FRP sheets as illustrated in Figure 4- 12, were used over the concrete surface to study the effect of delamination on the Q value.

Figure 4- 12: FRP sheets

In contrast to the previous results where the FRP were bonded to the concrete surface, the presence of voids or delamination under the FRP layer reduce the Q value relative to the Q value of the concrete surface. Figure 4- 13 shows that imperfect bond between the FRP and the concrete results in a reduction of the Q value relative to the Q value for the concrete test.

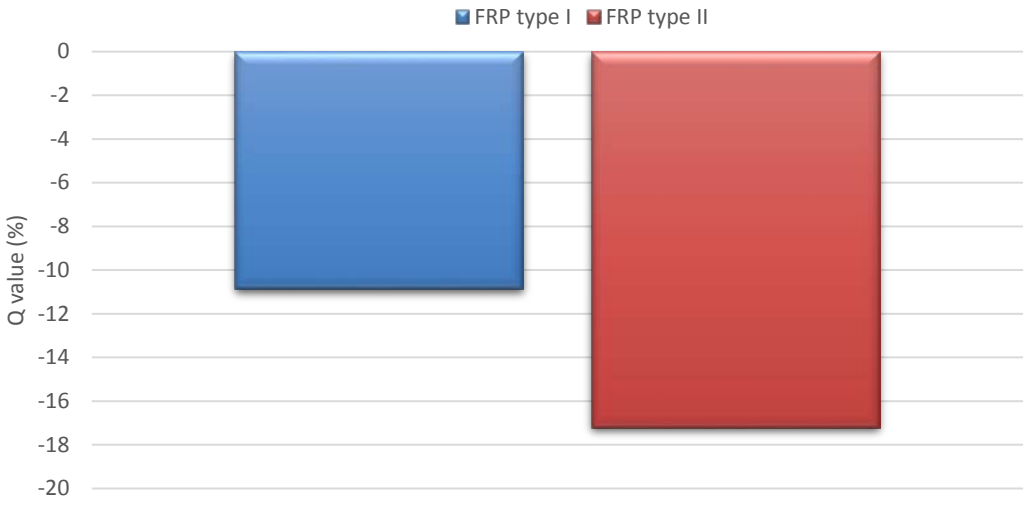

Figure 4- 13: Effect of delamination on the Q value

This conclusion could be used to identify the location and size of voids and debonded zones under the FRP layer. This information would be useful along with the results from the previous section in identifying the total effects of the parameters on the bond strength.

Infrared camera

An infrared camera is a device that forms an image using infrared radiation, similar to a common camera that forms an image using visible light. Their use is called thermography. Although infrared radiation (IR) is not detectable by the human eye, an IR camera can convert it to a visual image that depicts thermal variations across an object

or scene. IR covers a portion of the electromagnetic spectrum from approximately 900 to 14,000 nanometers (0.9–14 µm). IR is emitted by all objects at temperatures above absolute zero, and the amount of radiation increases with temperature [Flir, 2009].

In this study, a “Flir E50” infrared camera was used as shown in Figure 4- 14. The camera produces images of 240×180 pixels and composed of uncooled microbolometer with a spectral range of 7.5 to 13µm. The camera detects the thermal variations across the area captured by the camera.

Figure 4- 14: Infrared camera

Infrared camera test (heat dissipation): In this test, the rate of heat dissipation is recorded. The samples were subjected to a source of heat for a specific amount of time and the rate of cooling down is recorded and later correlated with corresponding bond properties. Two area from each sample were selected. The test configuration and setup is presented in Figure 4- 15.

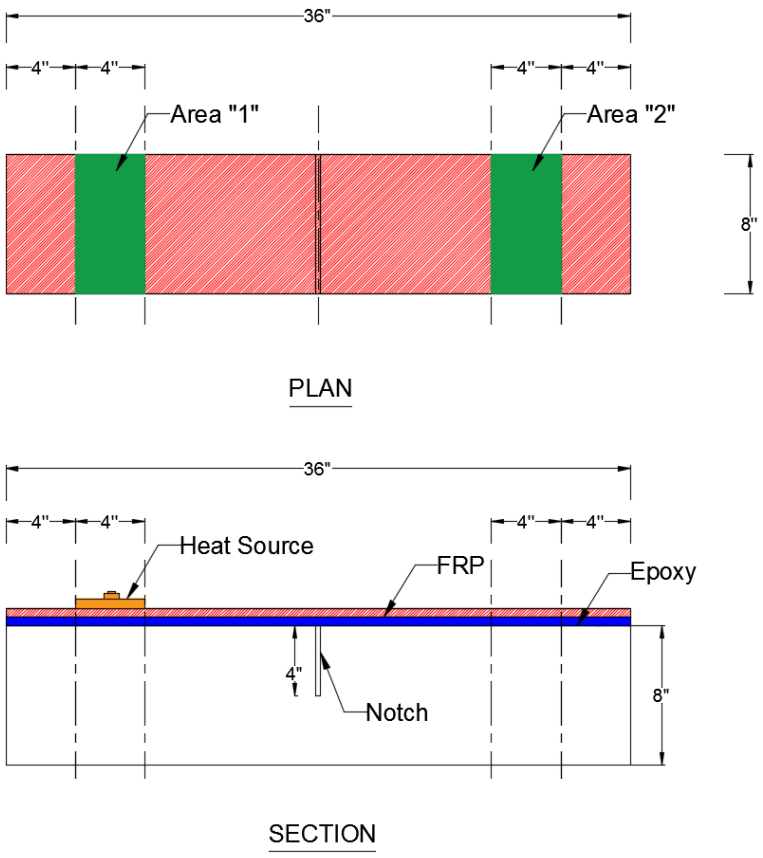

Figure 4- 15: Infrared camera test setup

The surface of the specimen was heated for 60 s using a flexible electric cover (electric power is about 450 W with a width of 4in.). The heat of the electric belt is controlled using a thermostat as illustrated in Figure 4- 16. The belt was preheated until it reaches 190 °F, placed on top of the required surface and then the power was turned off and the temperature was allowed to cool. After 60 seconds, the belt was removed from the top of the beam.

Figure 4- 16: Adjustable heat source

After removing the heat source, a video was recorded for three minutes using the infrared camera to capture the process of cooling down for each sample. The camera was placed at a height of 2 ft. above the concrete surface as illustrated in Figure 4- 17. The camera was connected to the “FLIR Research IR” software.

Figure 4- 17: Infrared camera video recording

“FLIR Research IR” as shown in Figure 4- 18, provided additional tools to record and analyze the infrared camera data. It is a powerful thermal analysis software for camera system command and control, high-speed data recording, real-time or playback analysis, and reporting. One of the important reasons for using this software is the option for manual calibration. Using that option, all the test performed were calibrated at the exact time through the experiment.

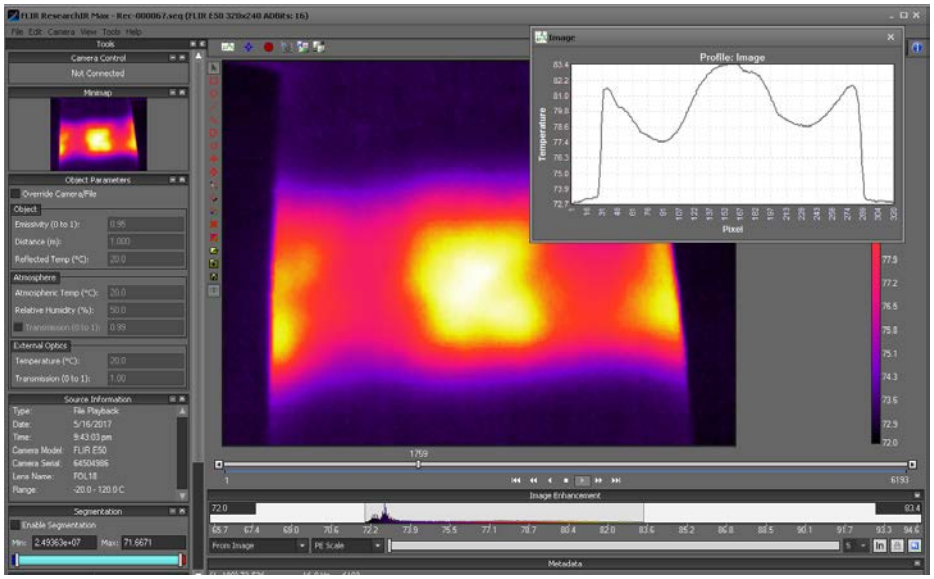

Figure 4- 18: “FLIR Research IR” software

The temperature profile of the heated part was recorded and the rate of heat dissipation was calculated. The change in temperature with time (heat dissipation °F/sec) is presented for each beam in Figure 4- 19 after 40 seconds from removing the heat source. The chart indicates that the rate of cooling down changes with respect to each parameter.

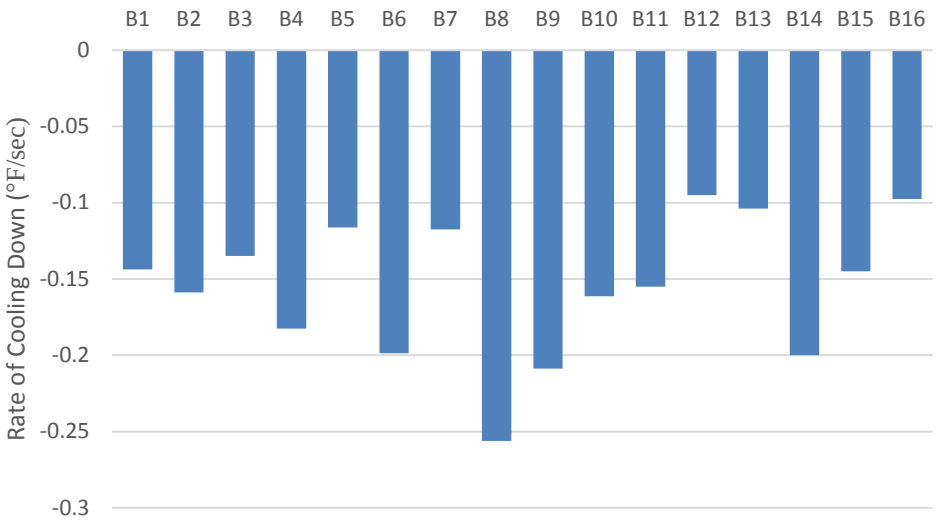

Figure 4- 19: Rate of cooling time after 40 seconds

To further analyze the data and determine the effect of each parameter on the heat dissipation, Minitab software package for statistical analysis was used. The inputs were selected to be the percentage change of the rate of cooling down of the FRP surface in relative to the rate of cooling down of the concrete surface. Following are some of the results of the design of experiment using Minitab software.

The first step is plotting the data several ways to see if any trends or anomalies appear that would not be accounted for by the model. Figure 4- 20 illustrates the four plots of the residuals generated by Minitab: a normal probability plot, residuals versus the fitted values, histogram and a run-order plot of the residuals. The four charts show the spread of the data and there is no clear pattern of the residuals. The residuals do appear to have, at least approximately, a normal distribution.

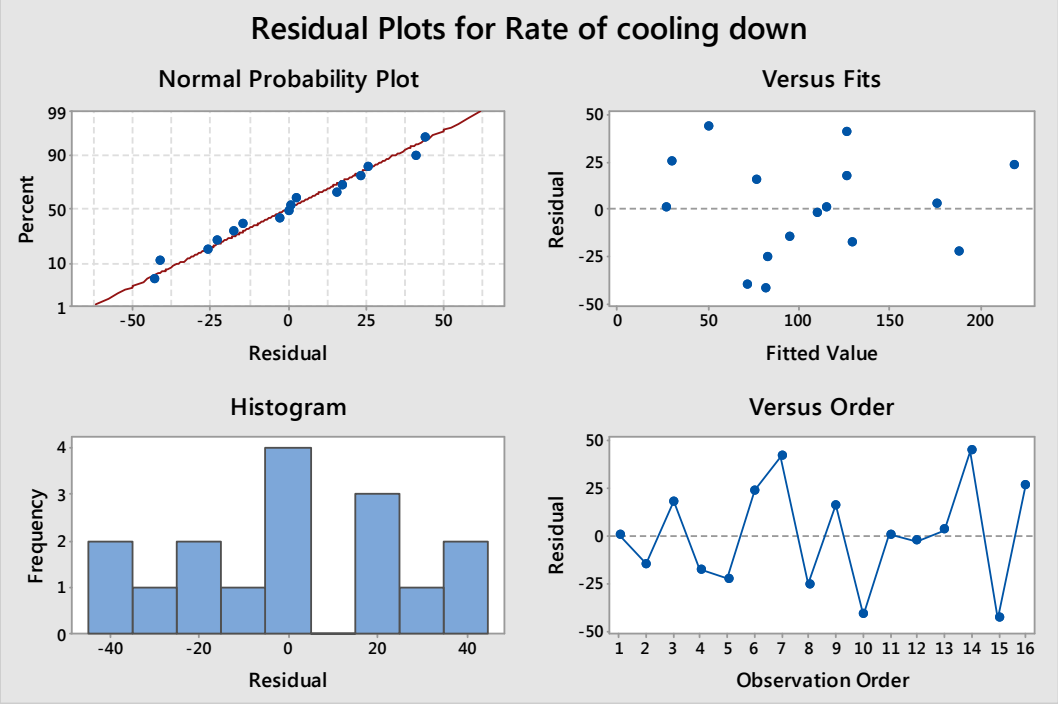

Figure 4- 20: Residual Plots for Rate of cooling down (%) after 40 seconds

Next step, to look at the plots of responses versus each parameter as presented in Figure 4- 21 for the data collected after 40 seconds. The plot of the rate of cooling down after 40 seconds (%) versus the FRP type shows that the rate of cooling down tend to increase with the increase in the thickness of the FRP layer. The plot of the number of epoxy layers shows that adding an extra layer of Epoxy decrease the rate of cooling down. For the Epoxy type, the chart shows that the Epoxy with higher viscosity tends to decrease the rate. Finally, the sandblasting surface preparation seems slightly increase the rate of cooling down relative to the surface prepared using hand grinding.

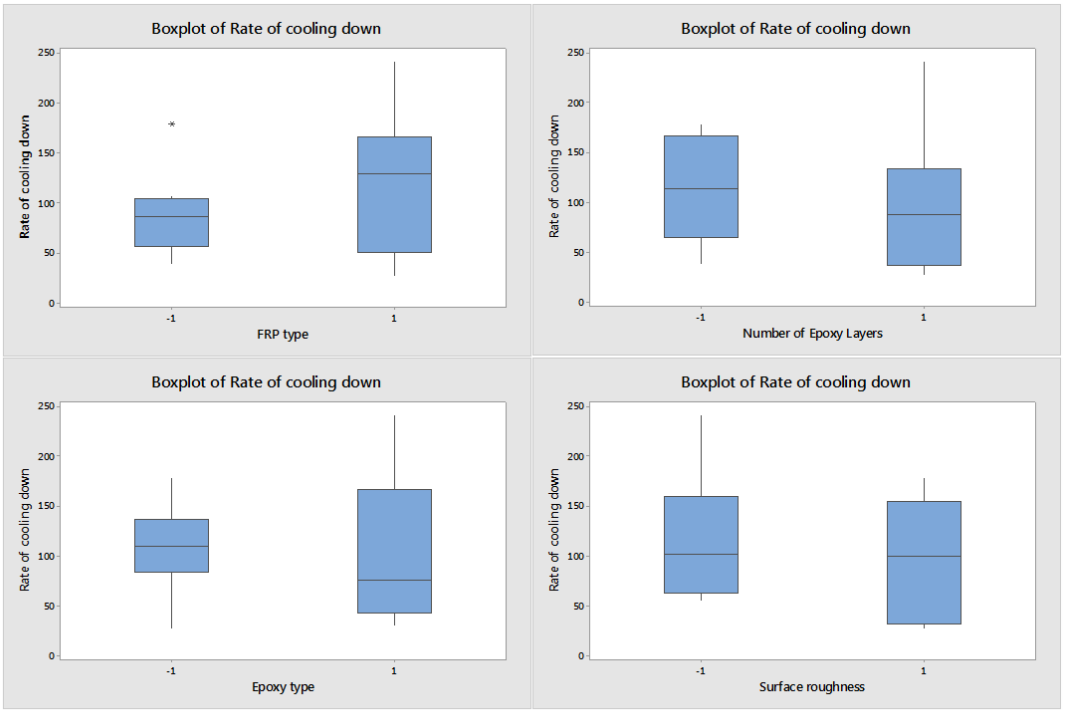

Figure 4- 21: Plots of responses after 40 seconds versus each parameter

To investigate the main effects, Minitab software presents the effect of each of the main parameters in a combined figure as illustrated in Figure 4- 22. The graph shows that the Epoxy type does not have an effect on the rate of cooling down. The FRP type seems to have the highest effect in respect to all the other parameters. The surface roughness appears to have an effect on the results.

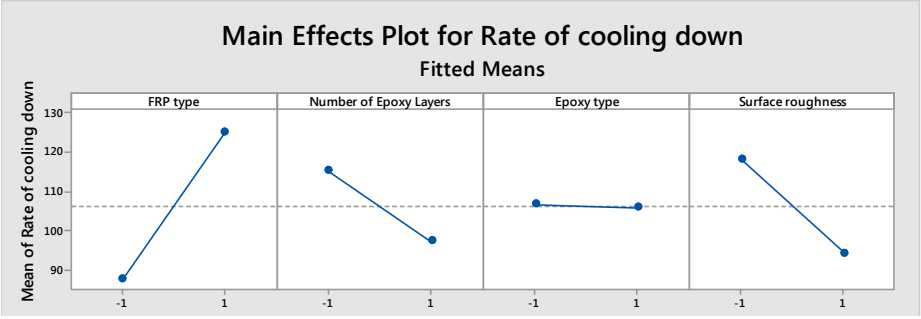

Figure 4- 22: Main Effect of the parameters

The interaction plot is presented in Figure 4- 23. The interaction plot shows that there is no interaction between the FRP type and the number of Epoxy Layers used. The graph also shows that the highest interaction is between the FRP type and both Epoxy type and the surface roughness. Also, there is a slight interaction between the number of Epoxy layer used and both the Epoxy type and the surface roughness. There is also an interaction between the Epoxy type and the surface roughness.

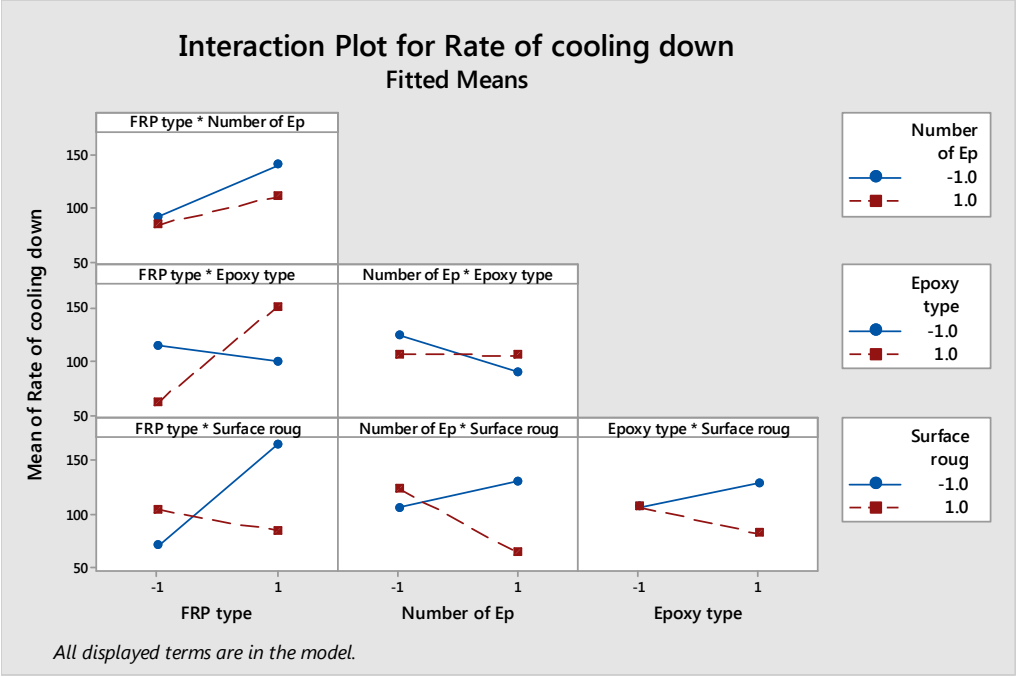

Figure 4- 23: Interaction plot for the rate of cooling down

Finally, to study the significance of each of the main parameters and the interaction between them, the ANOVA table prepared by Minitab is presented in Table 4- 2. The Table shows the FRP type followed by the surface roughness and the number of Epoxy Layers have the highest effect between all off the main parameters. However, none of

these parameters have a significant effect by itself. The model has an R square of 80.65%.

Table 4- 2: Analysis of variance for the Infrared camera test

Source	DF	Adj SS	Adj MS	F-Value	P-Value
Model	10	44381.9	4438.2	2.08	0.216
Linear	4	9168.1	2292.0	1.08	0.456
FRP type	1	5625.0	5625.0	2.64	0.165
Number of Epoxy Layers	1	1284.0	1284.0	0.60	0.473
Epoxy type	1	2.8	2.8	0.00	0.973
Surface roughness	1	2256.2	2256.2	1.06	0.351
2-Way Interactions	6	35213.9	5869.0	2.76	0.143
FRP type*Number of Epoxy Layers	1	506.2	506.2	0.24	0.646
FRP type*Epoxy type	1	11025.0	11025.0	5.18	0.072
FRP type*Surface roughness	1	13034.0	13034.0	6.12	0.056
Number of Epoxy Layers*Epoxy type	1	1167.4	1167.4	0.55	0.492
Number of Epoxy Layers*Surface roughness	1	7225.0	7225.0	3.39	0.125
Epoxy type*Surface roughness	1	2256.3	2256.3	1.06	0.351
Error	5	10648.6	2129.7		
Total	15	55030.6			

S	R-sq	R-sq(adj)	R-sq(pred)
46.1489	80.65%	41.95%	0.00%

The model prepared by Minitab present an equation that could be used in estimating the expected rate of cooling down for a specific beam. The estimated rate is useful in the evaluation of the FRP application process. A rate of cooling down value can provide a base for quality inspection and assurance. The equation for estimating the rate of cooling down is presented as follows.

$$\text{Rate of cooling down (\%)} = 106.2 + 18.8\,[\text{FRP type}] - 9.0\,[\text{Nb. of Epoxy Layers}] - 0.4\,[\text{Epoxy type}] - 11.9\,[\text{Surface roughness}] - 5.6\,[\text{FRP type} * \text{Nb. of Epoxy Layers}] + 26.3\,[\text{FRP type} * \text{Epoxy type}] - 28.5\,[\text{FRP type} * \text{Surface roughness}] + 8.5\,[\text{Nb. of Epoxy Layers} * \text{Epoxy type}] - 21.3\,[\text{Nb. of Epoxy Layers} * \text{Surface roughness}] - 11.9\,[\text{Epoxy type} * \text{Surface roughness}] \quad \text{Eq. (4-2)}$$

Where, FRP type is -1 for FRP type I and +1 for FRP type II. Similarly, for each parameter in the previous equation, a value of -1 is assigned to the type I and a value of +1 is assigned to type II.

Another approach was used in this section to identify the location and size of any voids present below the FRP sheet. In this section, a simpler and more comprehensive test is presented to locate the voids, delamination or any imperfections that might be hidden below the FRP layer.

In this test, the samples were subjected to a source of heat (heat lamp) for 10 seconds as illustrated in Figure 4- 24. Two pictures were recorded one picture before heating the sample and the other was taken just after the heating process. This test was selected due to its capability to detect imperfection below the FRP sheet without the need for a point to point inspection.

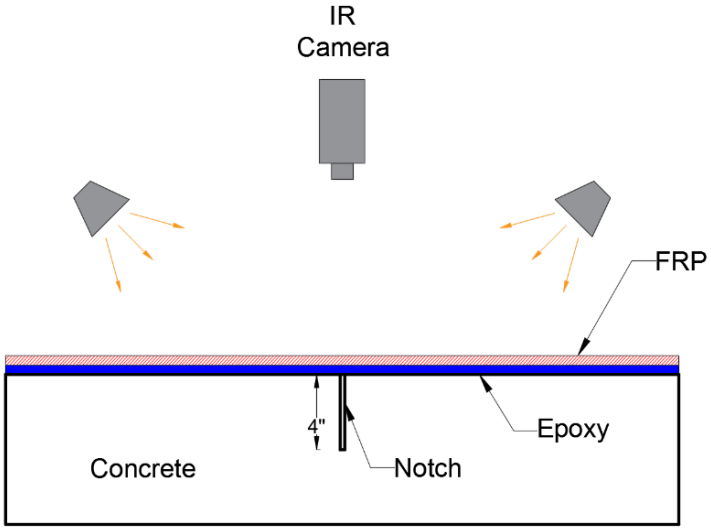

Figure 4- 24: Infrared camera test setup to locate voids and delaminations

The First step in this test is to heat the FRP surface using the heat lamp as illustrated in Figure 4- 25. The FRP surface was subjected to the heat for a total of 10 seconds.

Figure 4- 25: Heating the beam using heat lamp

After the heating process, two pictures were recorded of each sample using the infrared camera as illustrated in Figure 4- 26. Each of the two pictures captures half of the beam for clear presentation.

Figure 4- 26: Infrared camera used to capture pictures of the beam surface

Samples of the results are presented in Figure 4- 27 and Figure 4- 28. The pictures show that an infrared camera is a powerful tool for the detection of voids. From these two pictures, the location and the size of the voids could be easily determined and used to assess their effect on the overall strength of the bond.

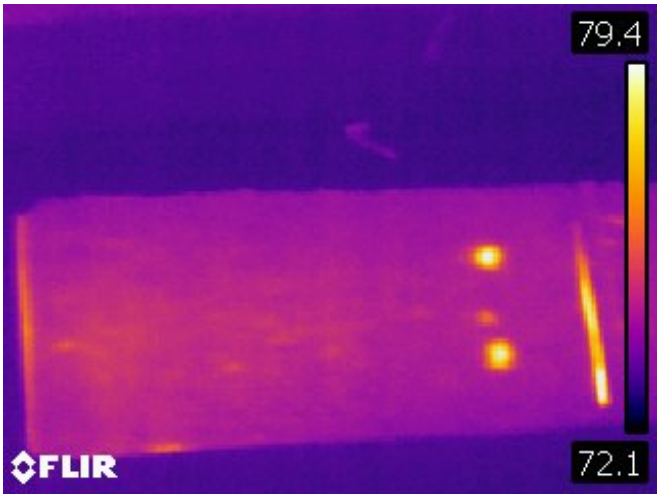

Figure 4- 27: Infrared camera picture of two 0.8 in × 0.8 in voids

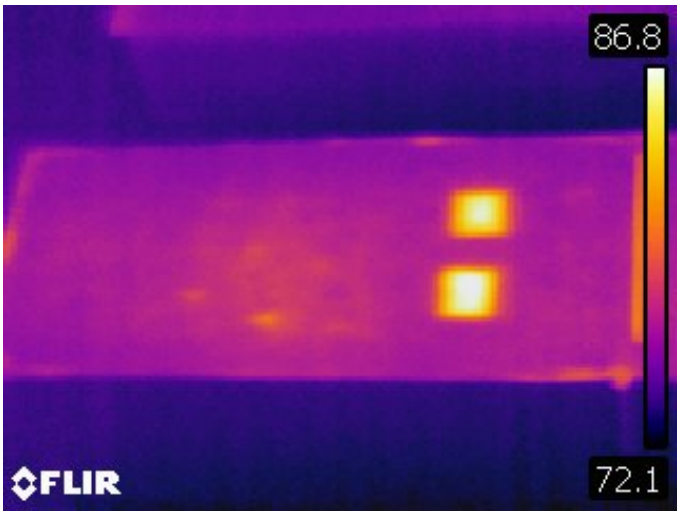

Figure 4- 28: Infrared camera picture of two 1.6 in × 1.6 in voids

For the purpose of detecting debonding between the concrete and the FRP. Some cured FRP sheets were placed over the concrete surface to simulate that the FRP layer is not bonded to the concrete surface. The results show that if the FRP is not bonded to the concrete surface, the FRP layer appears to be bright in the picture in a similar way to the voids as presented in Figure 4- 29.

Figure 4- 29: Infrared camera picture of debonded FRP layer

This method appears to be simple, fast and comprehensive and could be used to identify the location and size of voids and debonded zones under the FRP layer. This information would be useful along with the results from the previous section in identifying the total effects of the parameters on the bond strength.

Ultrasound Tomography Test

The ultrasound testing is considered to be the most used NDE technique after the visual inspection. The concept of this method depends on measuring the speed of the ultrasonic wave when it travels through the material under inspection moving from a transmitter to a receiver. The speed of the wave may carry some information on the quality of the object and any unexpected reflections might lead to the identification of cracks and unwanted imperfections in the material.

This test was performed using an ultrasonic tomography device as shown in Figure 4- 30. The device is based on the ultrasonic multichannel pulse-echo technology using 8

channels. One channel transmits and the echoes are received by the other seven channels. Each channel transmits in turn. A complete measurement consists of 56 A-scans. These are used to compute and display a B-scan. This device produces a 50 KHz shear wave.

Figure 4- 30: Ultrasonic tomography device

The ultrasound tomography device provides information about the amplitude of the reflected wave through the depth of the sample. The value of the amplitude is used in this test to compare the effect each parameter. The amplitude of each sample to be correlated with the overall bond strength.

Ultrasound test: Four scans were recorded for each sample as illustrated in Figure 4- 31 where the A and B scans were recorded. This test was repeated twice. Points 2 and 4 represents a scan on a surface of the beams above the location of the embedded voids while Points 1 and 3 represents a scan on a surface of the beams with no voids.

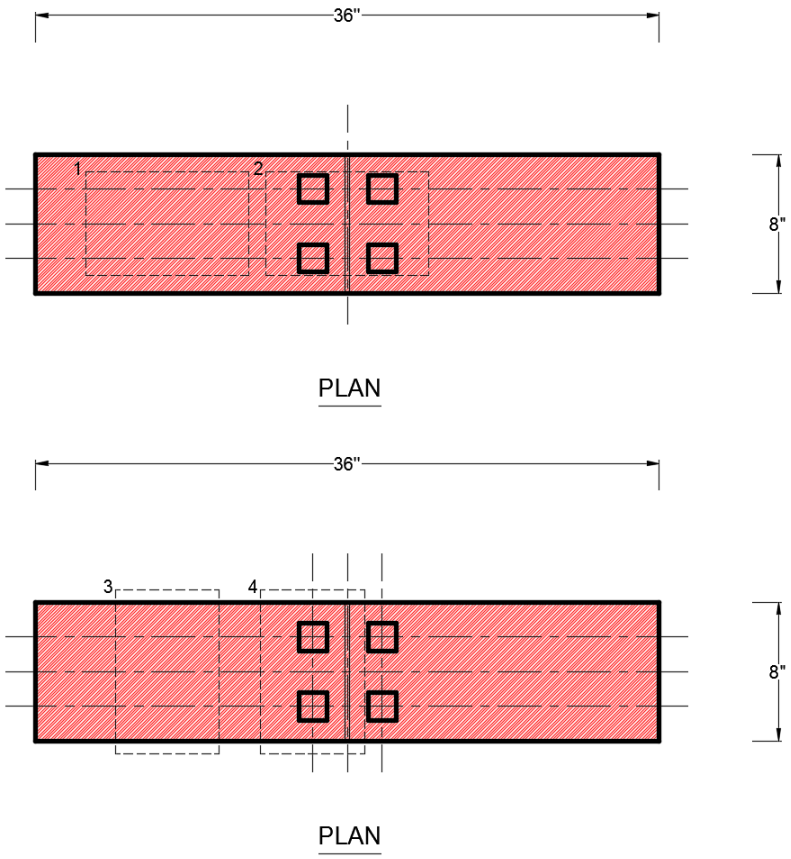

Figure 4- 31: Ultrasonic test configuration

Figure 4- 32 shows the details of the ultrasonic tomography handle. The figure shows the distribution of the transmitter and receivers on the device. Each of the shown pins works as receiver and transmitter alternatively.

Figure 4- 32: Ultrasonic tomography handle

Each of the beams was scanned using the ultrasonic tomography device as illustrated in Figure 4- 33. Four images representing the B-scan were recorded over the FRP surface for each of the two repetitions. Additional scans were recorded from the concrete surface of each beam. The scan of the concrete surface was taken from the side of the beam as illustrated in Figure 4- 34.

Figure 4- 33: Ultrasonic testing over the FRP surface

Figure 4- 34: Ultrasonic testing over the concrete surface

A sample of the B-scan of the ultrasound test for two different beams is presented in Figure 4- 35. The results show that the parameters in the study seem to have an effect on the amplitude values from the ultrasound scan.

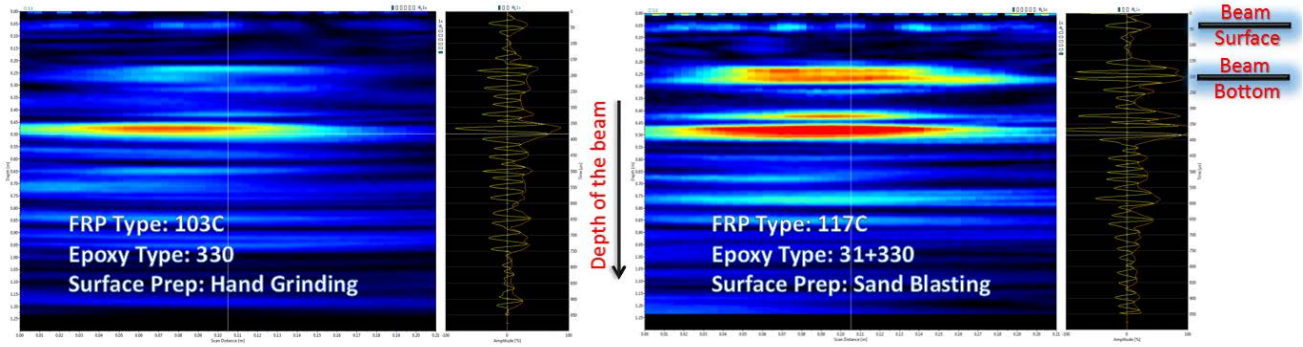

Figure 4- 35: A sample of the B-scan of two different beams

To further analyze the data and determine the effect of each parameter on the Amplitude, The value of the reflected amplitude from the surface of each beam was selected. The

selected amplitude value for all the beams were analyzed using the Minitab software. Following are some of the results of the design of experiment using Minitab software.

Results for point 3 were selected to represent the properties of each beam. Point 3 from the ultrasound test is located in the middle of the FRP surface and away from any voids. Figure 4- 36 examine the assumption that the residuals are approximately normally distributed, are independent and have equal variances. The four charts show a large spread of the data and that there is no clear pattern to the residuals. The residuals do appear to have approximately, a normal distribution.

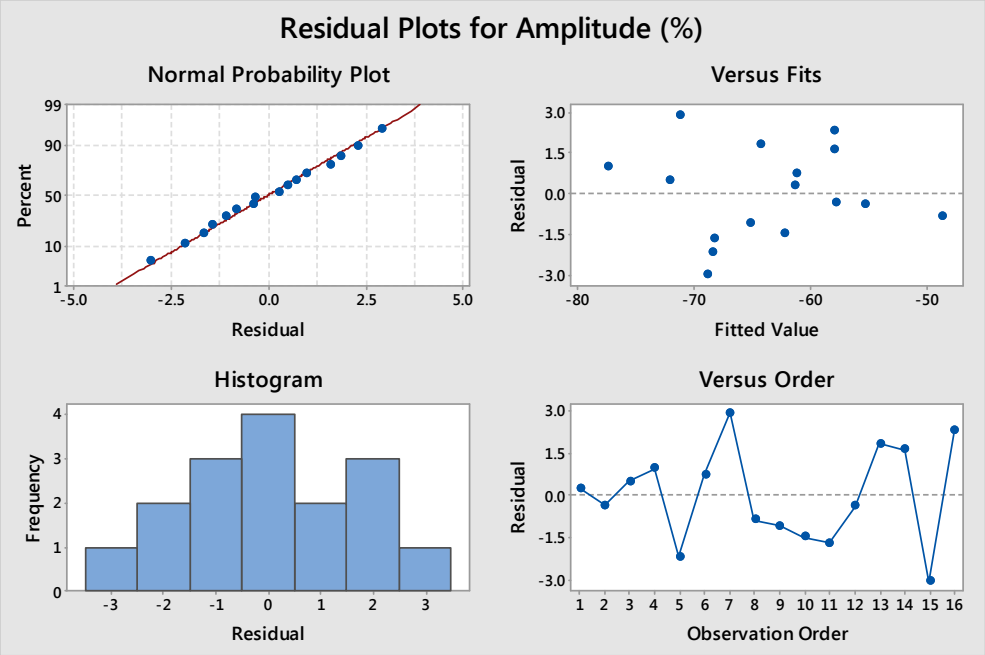

Figure 4- 36: Residual Plots for the amplitude (%)

Next step, to look at the plots of responses versus each parameter as presented in Figure 4- 37. The plot shows each parameter versus the percentage change of the amplitude value of the FRP surface relative to the amplitude value of the concrete surface. The first chart of the amplitude (%) versus the FRP type shows that the

amplitude tends to decrease with the increase in the thickness of the FRP layer. The plot of the number of epoxy layers shows that adding an extra layer of Epoxy increase the amplitude reading. For the Epoxy type, the chart shows that the Epoxy with higher viscosity tends to decrease the amplitude value. Finally, surface preparation does not seem to have an effect on the amplitude value.

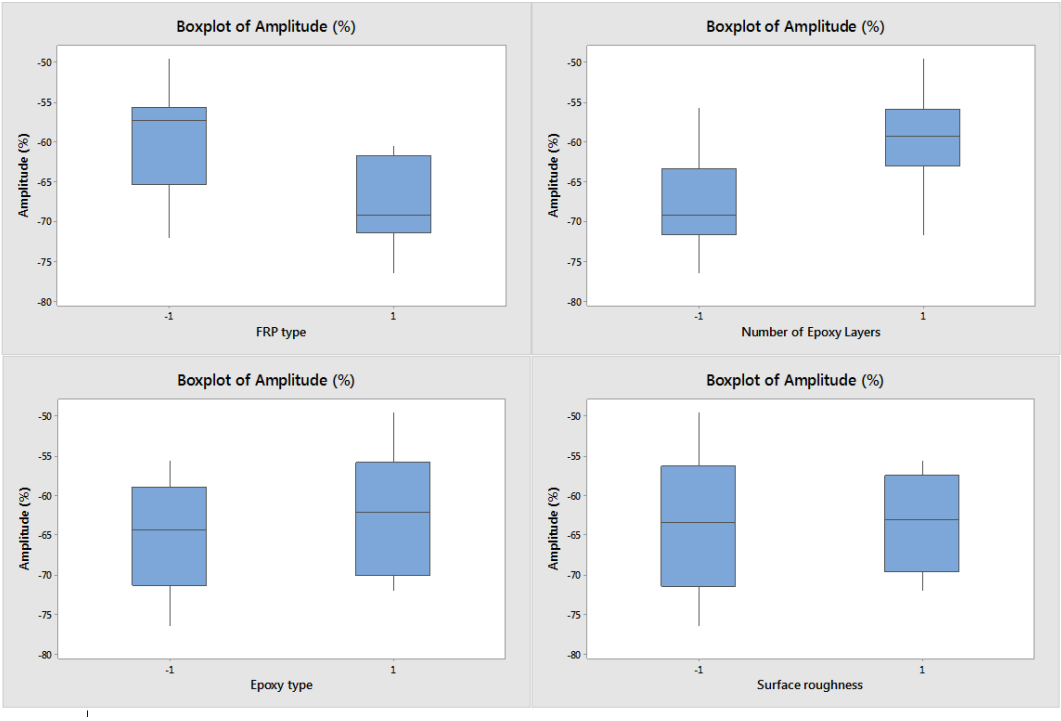

Figure 4- 37: Plots of responses versus each parameter

Minitab software presents the effect of each of the main parameters in a combined figure as illustrated in Figure 4- 38.

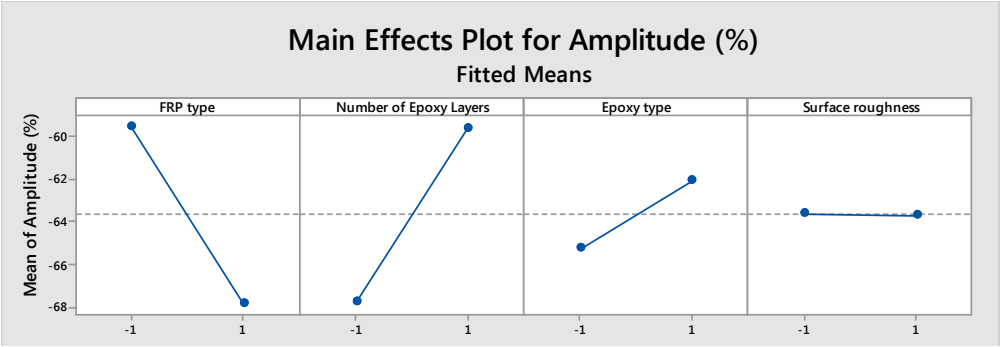

Figure 4- 38: Main Effect of the parameters

The interaction plot is presented in Figure 4- 39. The interaction plot shows that there is no interaction between the FRP type and the number of Epoxy Layers used or the Epoxy type. The graph shows that there is a slight interaction between the FRP type and the surface roughness. Also, it seems that there is an interaction between the number of Epoxy type and the surface roughness.

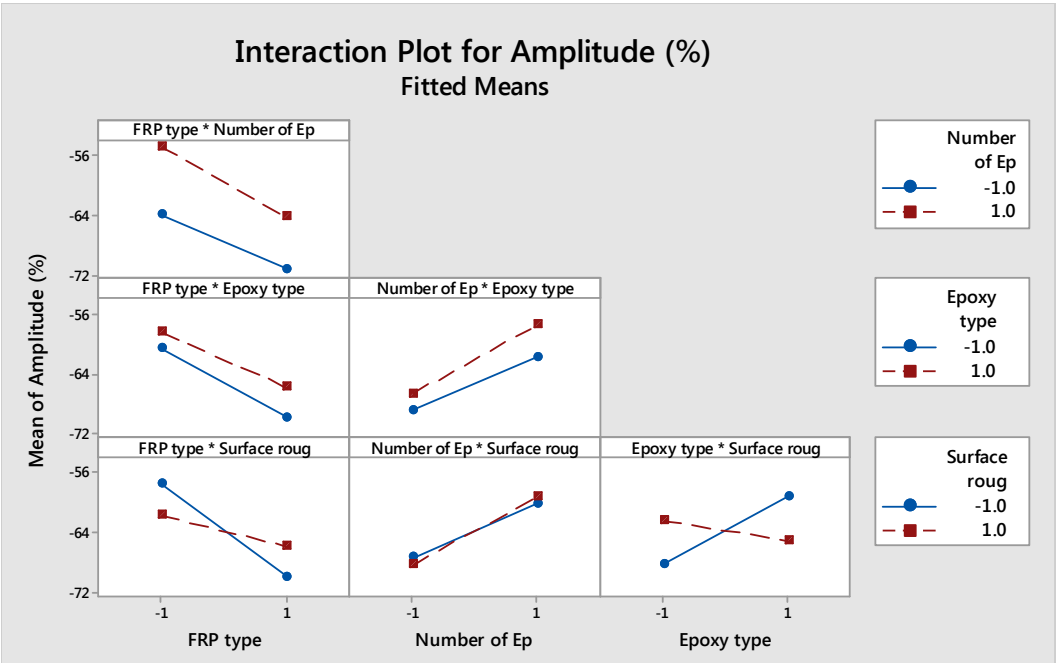

Figure 4- 39: Interaction plot for the amplitude value

Finally, to study the significance of each of the main parameters and the interaction between them, the ANOVA table prepared by Minitab is presented in Table 4- 3. The Table shows the FRP type, the number of Epoxy layers used, the interaction between the FRP type and the surface roughness and finally the interaction between the Epoxy type and the surface roughness has a significant effect on the Amplitude value (%). The model has an R square of 94.99%.

Table 4- 3: Analysis of variance for the ultrasound test

Source	DF	Adj SS	Adj MS	F-Value	P-Value
Model	10	805.993	80.599	9.47	0.011
Linear	4	582.675	145.669	17.12	0.004
FRP type	1	276.032	276.032	32.45	0.002
Number of Epoxy Layers	1	266.091	266.091	31.28	0.003
Epoxy type	1	40.524	40.524	4.76	0.081
Surface roughness	1	0.028	0.028	0.00	0.957
2-Way Interactions	6	223.318	37.220	4.38	0.063
FRP type*Number of Epoxy Layers	1	4.219	4.219	0.50	0.513
FRP type*Epoxy type	1	3.220	3.220	0.38	0.565
FRP type*Surface roughness	1	67.777	67.777	7.97	0.037
Number of Epoxy Layers*Epoxy type	1	4.289	4.289	0.50	0.509
Number of Epoxy Layers*Surface roughness	1	2.850	2.850	0.34	0.588
Epoxy type*Surface roughness	1	140.963	140.963	16.57	0.010
Error	5	42.536	8.507		
Total	15	848.528			

S	R-sq	R-sq(adj)	R-sq(pred)
2.91670	94.99%	84.96%	48.67%

The model prepared by Minitab present an equation that could be used in estimating the expected Amplitude value for a specific beam. The estimated Amplitude value is useful in the evaluation of the FRP application process. The Amplitude value can provide a base

for quality inspection and assurance. The equation for estimating the Amplitude value is presented as follows.

$$\begin{aligned}\text{Amplitude}\,(\%) = {} & -63.665 - 4.154\,[\text{FRP type}] \\ & + 4.078\,[\text{Nb. of Epoxy Layers}] + 1.591\,[\text{Epoxy type}] \\ & - 0.041\,[\text{Surface roughness}] - 0.513\,[\text{FRP type} \\ & * \text{Nb. of Epoxy Layers}] + 0.449\,[\text{FRP type} * \text{Epoxy type}] \\ & + 2.058\,[\text{FRP type} * \text{Surface roughness}] \\ & + 0.518\,[\text{Nb. of Epoxy Layers} * \text{Epoxy type}] \\ & + 0.422\,[\text{Nb. of Epoxy Layers} * \text{Surface roughness}] \\ & - 2.968\,[\text{Epoxy type} * \text{Surface roughness}]\end{aligned} \qquad \text{Eq. (4-3)}$$

Where, FRP type is -1 for FRP type I and +1 for FRP type II. Similarly, for each parameter in the previous equation, a value of -1 is assigned to the type I and a value of +1 is assigned to type II.

In this section, a simple approach is presented to identify and locate any voids and delamination that might be hidden under the FRP surface. The method depends on visually analyze the B-scan of each beam to identify the presence of hidden voids.

Samples of the results are presented in Figure 4- 40 and Figure 4- 41. The pictures show that the ultrasound tomography device could be used for the detection of voids. From these two pictures, the location and the size of the voids could be determined and used to assess their effect on the overall strength of the bond.

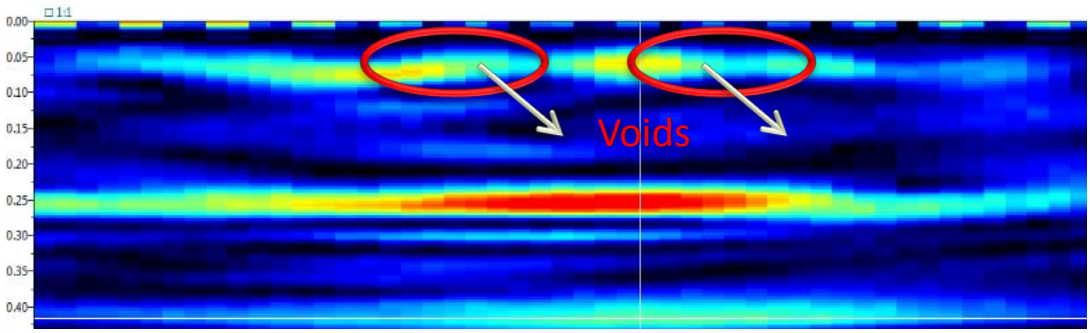

Figure 4- 40: Ultrasound B-scan of two 0.8 in × 0.8 in voids

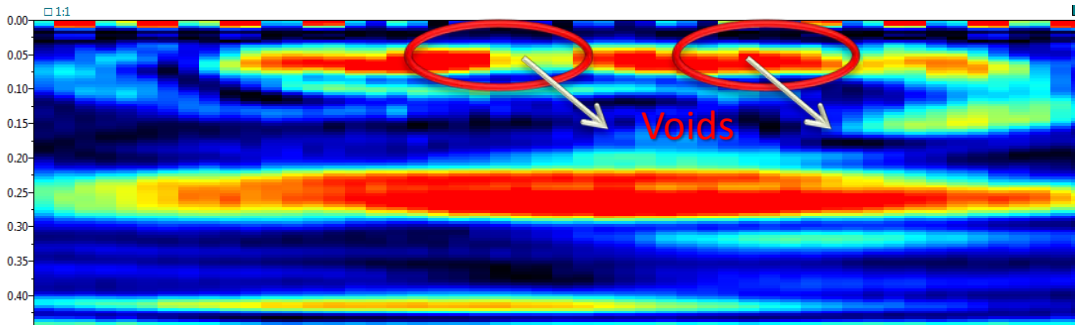

Figure 4- 41: Ultrasound B-scan of two 1.6 in × 1.6 in voids

For the purpose of detecting debonding between the concrete and the FRP. Some cured FRP sheets were placed over the concrete surface to simulate that the FRP layer is not bonded to the concrete surface. The results show that if the FRP is not bonded to the concrete surface, the amplitude value is significantly higher as the wave is reflected from the surface and do not penetrate through the concrete beam. The FRP layer appears in a similar way to the voids as presented in Figure 4- 42.

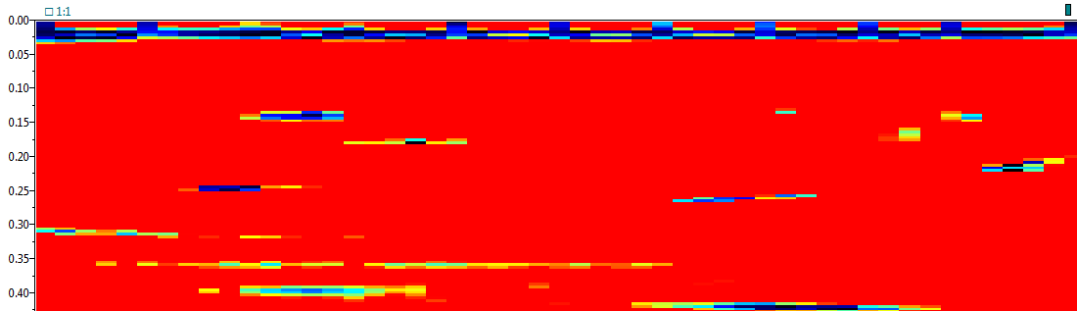

Figure 4- 42: Ultrasound B-scan debonded FRP layer

This method, in general, offers good capabilities in detecting voids, debonding, number of Epoxy layers used and FRP type. This information would be useful in identifying the total effects of the parameters on the bond strength.

Similarly, another study was performed to investigate the effect of the bond parameters on the amplitude value. In this section, the wave traveling between the exterior transmitter and receiver were considered. This increase the distance traveled by the wave which increases its exposure to the bond parameters. Minitab software was used to analyze the data. Following are some of the results of the design of experiment using Minitab software. Results for point 3 were selected to represent the properties of each beam. Point 3 from the ultrasound test is located in the middle of the FRP surface and away from any voids.

Minitab software presents the effect of each of the main parameters in a combined figure as illustrated in Figure 4- 43.

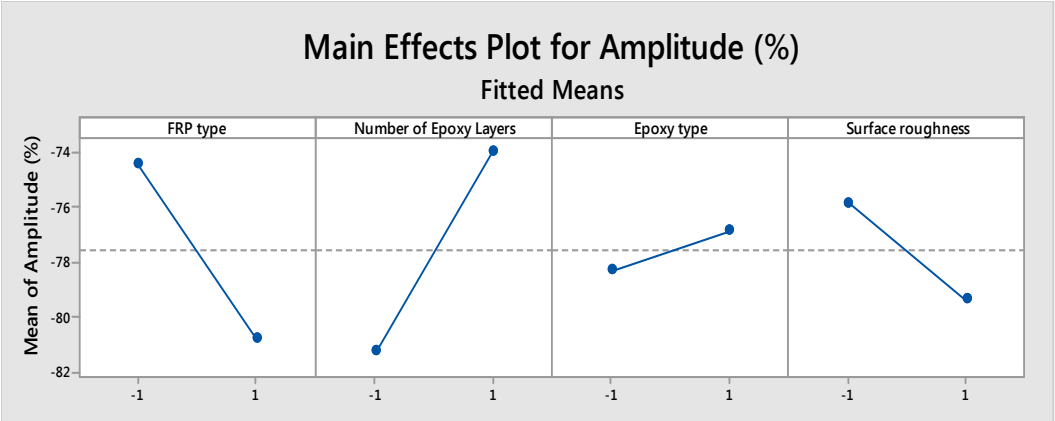

Figure 4- 43: Main Effect of the parameters

The interaction plot is presented in Figure 4- 44. The interaction plot shows that there is no interaction between the FRP type and the number of Epoxy Layers used or the Epoxy type. The graph shows that there is a slight interaction between the FRP type and the surface roughness. Also, it seems that there is an interaction between the number of Epoxy type and the surface roughness.

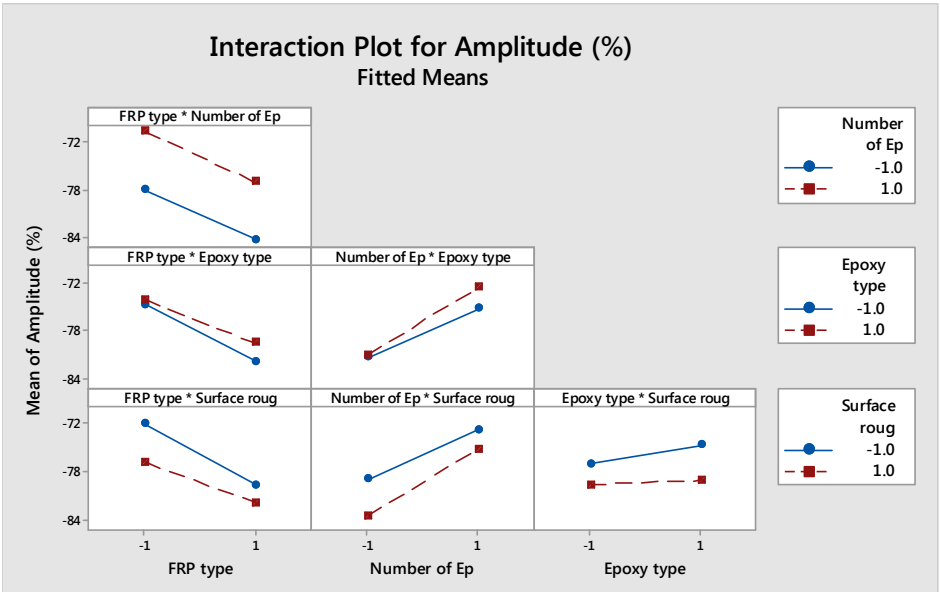

Figure 4- 44: Interaction plot for the amplitude value

The model prepared by Minitab present an equation that could be used in estimating the expected Amplitude value for a specific beam. The estimated Amplitude value is useful in the evaluation of the FRP application process. The Amplitude value can provide a base for quality inspection and assurance. The equation for estimating the Amplitude value is presented as follows.

$$\begin{aligned}\text{Amplitude}\ (\%)\ = {} & -77.59\ -\ 3.17\ [\text{FRP type}] \\ & +\ 3.66\ [\text{Number of Epoxy Layers}]\ +\ 0.73\ [\text{Epoxy type}] \\ & -\ 1.76\ [\text{Surface Roughness}]\ -\ 0.03\ [\text{FRP type} \\ & *\ \text{Number of Epoxy Layers}]\ +\ 0.44\ [\text{FRP type} * \text{Epoxy type}] \\ & +\ 0.64\ [\text{FRP type} * \text{Surface Roughness}] \\ & +\ 0.59\ [\text{Number of Epoxy Layers} * \text{Epoxy type}] \\ & +\ 0.54\ [\text{Number of Epoxy Layers} * \text{Surface Roughness}] \\ & -\ 0.46\ [\text{Epoxy type} * \text{Surface Roughness}]\end{aligned} \qquad \text{Eq. (4-4)}$$

Where, FRP type is -1 for FRP type I and +1 for FRP type II. Similarly, for each parameter in the previous equation, a value of -1 is assigned to the type I and a value of +1 is assigned to type II.

Ground Penetrating Radar (GPR) Test

Ground Penetrating Radar (GPR) uses high-frequency radio waves that propagate into the material under investigation. The transmitter sends a signal into the material. The transmitting signal gets reflected from the different surfaces and the objects

throughout the depth and the reflected signal is received by the receiver antenna. The received data is then processed and displayed. The GPR wave gets reflected if there is a different material in the path of propagation of the wave. The output signal of GPR scan possesses valuable information about the materials that it passes through. The output of the GPR scan is presented in form of A-scan or B-scan.

The first reflection of the GPR wave is called direct wave or direct coupling. This direct wave indicates the top surface. Figure 4- 43 shows a GPR reflection signal with direct coupling at the top of it.

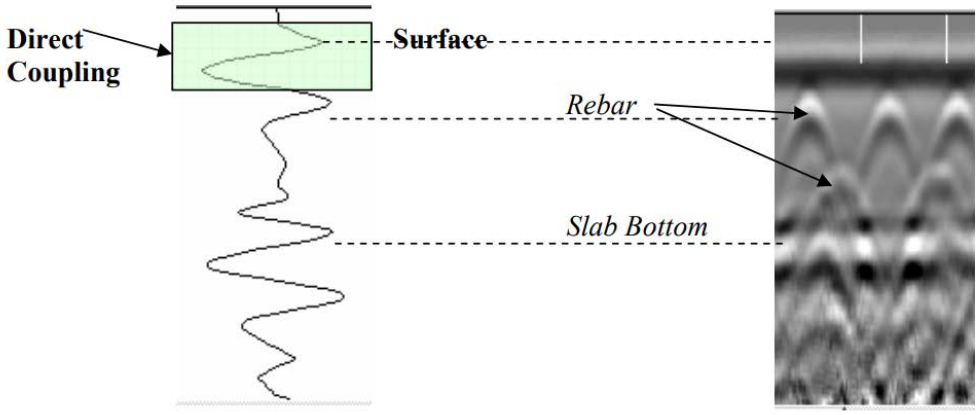

Figure 4- 45: Typical GPR A-scan

For a typical FRP repaired structure the FRP Layer and the Epoxy layer are located on top of the concrete and by consequence, they lie in the direct coupling zone. The following statement is mentioned in the GSSI concrete inspection handbook. “The negative peak (a straight horizontal black line in the B-scan display) immediately below the surface is a part of the direct coupling. Some variations may be seen within the negative peak. They usually indicate changes in concrete properties within the top inch of material, though their accurate interpretation is difficult” [GSSI Concrete Handbook, 2015].

In this study, a GPR system acquired from Geophysical Survey System Inc. (GSSI) is used with a 2600 MHz GPR antenna. The 2600 MHz antenna is able to scan concrete up to a depth of 10 in with high resolution as illustrated in Figure 4- 44. The GPR device provides information about the amplitude of the reflected wave through the depth of the sample. The value of the amplitude is used in this test to compare the effect each parameter. The amplitude of each sample to be correlated with the overall bond strength.

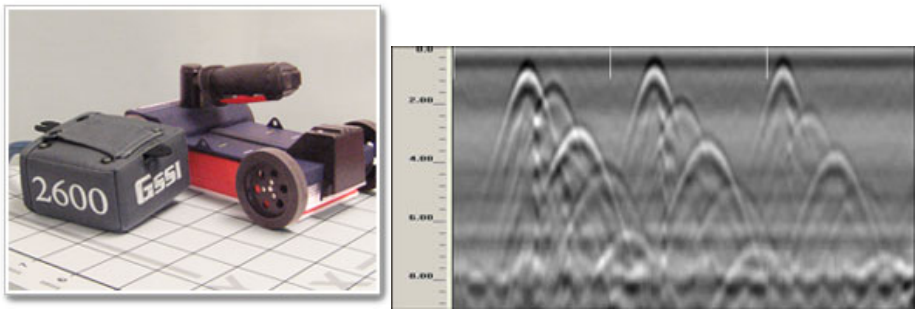

Figure 4- 46: GPR 2600 MHz antenna

Ground Penetration Radar (GPR) test: Two-line scans were recorded for each sample as illustrated in Figure 4- 45 where the A-scan and B-scan were recorded. This test was repeated twice. Line scan 2 represents a scan on a surface of the beams above the location of the embedded voids while line scan 1 represents a scan on a surface of the beams with no voids.

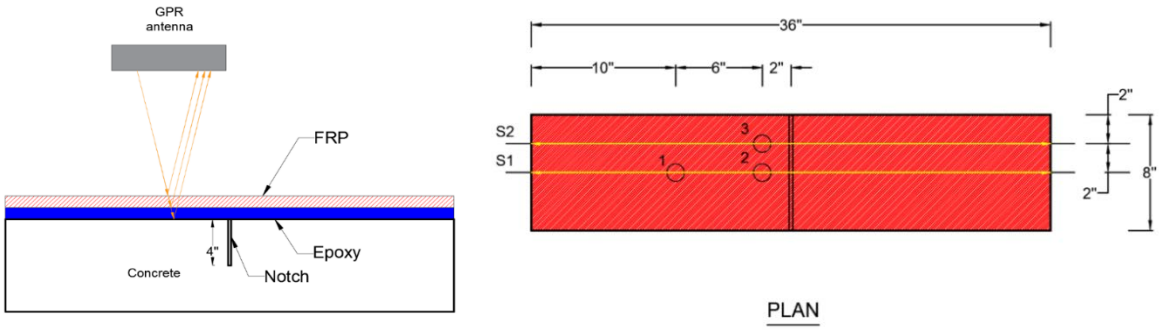

Figure 4- 47: GPR Test configuration

The GPR system used in this test from GSSI is presented in Figure 4- 46. The system consists of a laptop and SIR-30 control unit mounted on a cart for easier mobility. The line scan was performed using a mini-cart connected to the GPR antenna as shown in Figure 4- 47.

Figure 4- 48: GPR device

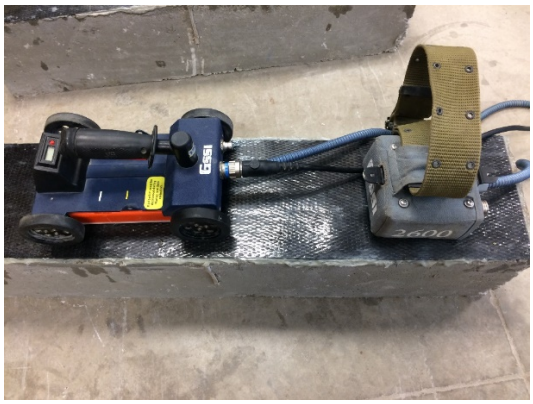

Figure 4- 49: 2600 MHz antenna connected to a mini-cart

A sample of the results from the GPR is presented in Figure 4- 48. The figure represents the B-scan of two different beams with different parameters. The B-scan indicate that the

amplitude values differs corresponding to the different parameters. This information is useful to study the different parameters.

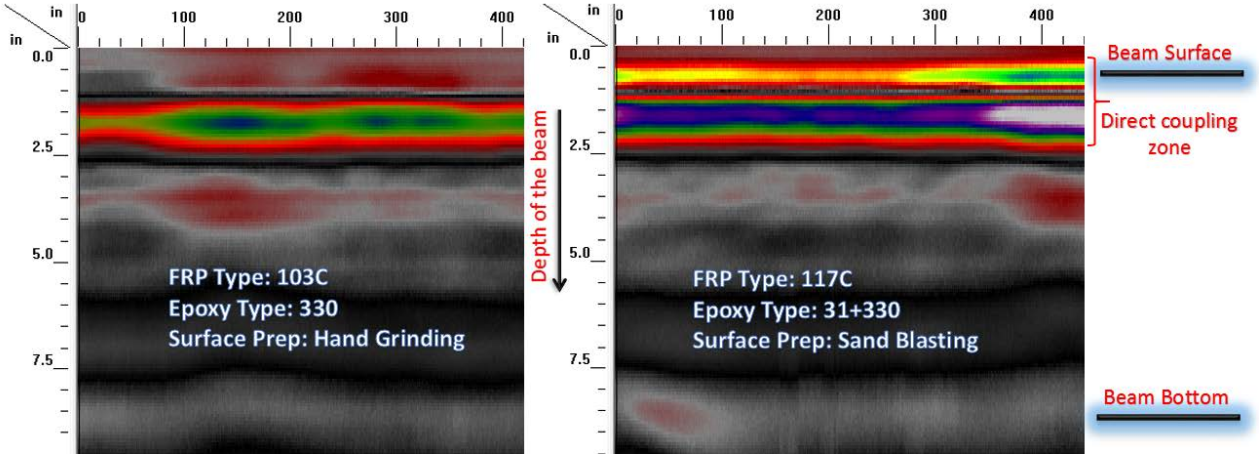

Figure 4- 50: A sample of the B-scan of two different beams

To further study of the data recorded from the GPR test, the A-scan of three different beams is presented. The figure shows that the negative amplitude within the direct coupling zone is affected by the different parameters in the study.

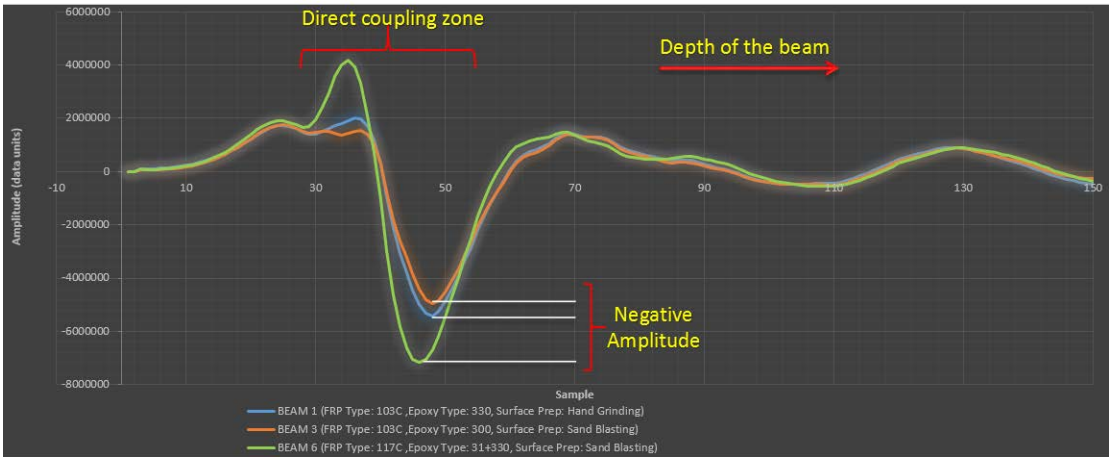

Figure 4- 51: A sample of the A-scan of three different beams

The negative amplitude values for all the beams were analyzed using the Minitab software. The negative amplitude of the direct coupling zone is presented in a percentage difference compared to the negative amplitude of the concrete surface without FRP. Following are some of the results of the design of experiment using Minitab software. Figure 4- 50 examine the assumption that the residuals are approximately normally distributed, are independent and have equal variances. The four charts show a large spread of the data and that there is no clear pattern of the residuals. The residuals do appear to have approximately, a normal distribution.

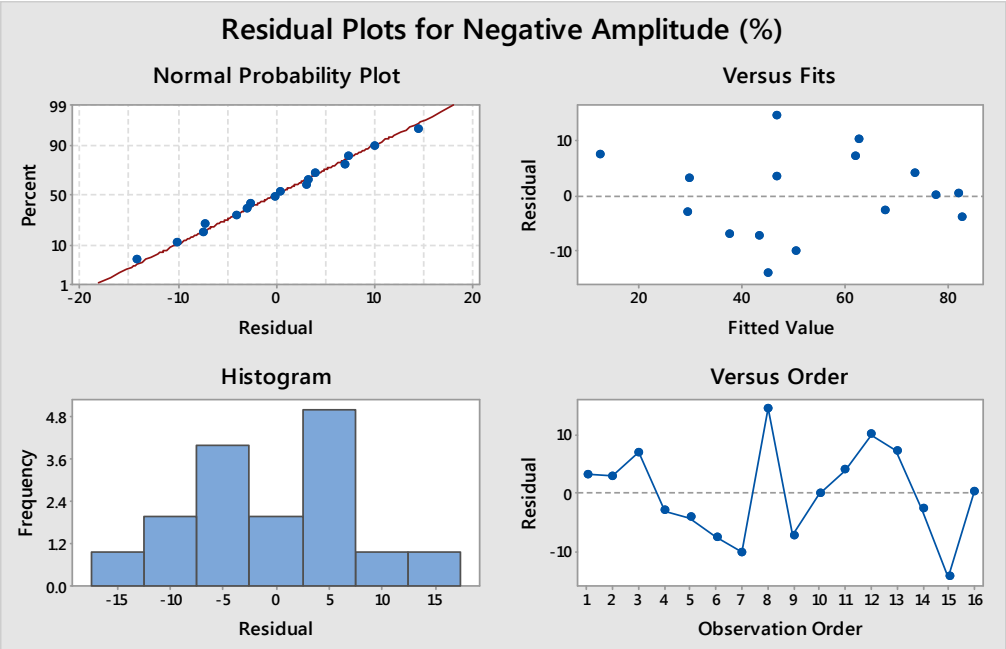

Figure 4- 52: Residual Plots for the Negative amplitude (%)

Next step, to look at the plots of responses versus each parameter as presented in Figure 4- 51. The plot shows each parameter versus the percentage change of the amplitude value of the FRP surface relative to the amplitude value of the concrete surface. The first chart of the amplitude (%) versus the FRP type shows that the

amplitude tends to decrease with the increase in the thickness of the FRP layer. The plot of the number of epoxy layers shows that adding an extra layer of Epoxy increase the amplitude reading. For the Epoxy type, the chart shows that the Epoxy with higher viscosity tends to increase the amplitude value. Finally, surface preparation using sandblasting seems to increase the amplitude value compared to hand grinding.

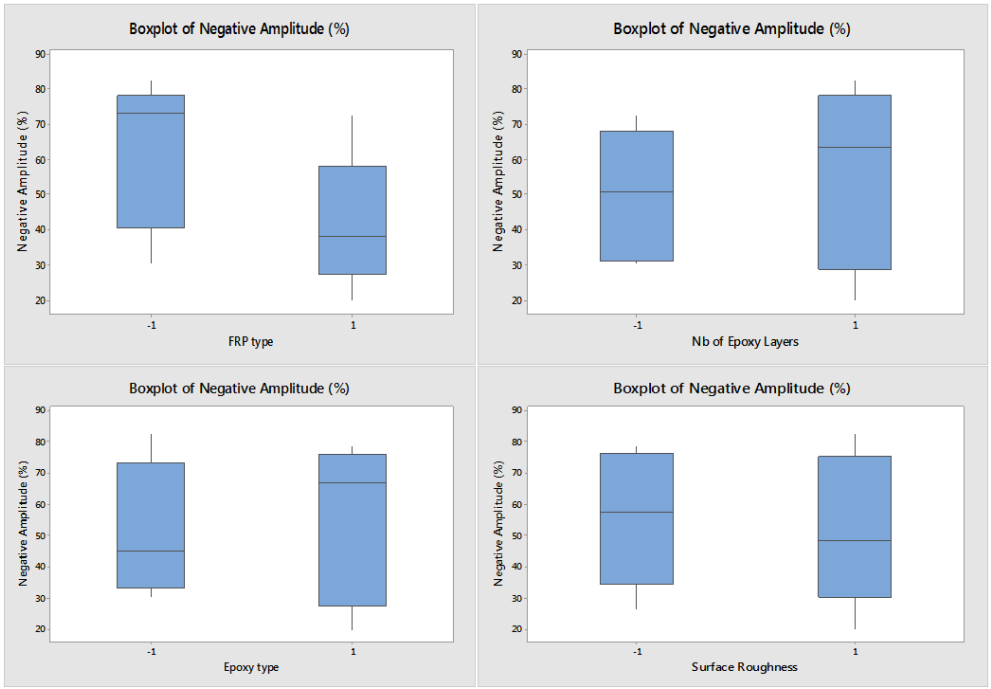

Figure 4- 53: Plots of responses versus each parameter

Minitab software presents the effect of each of the main parameters in a combined figure as illustrated in Figure 4- 52.

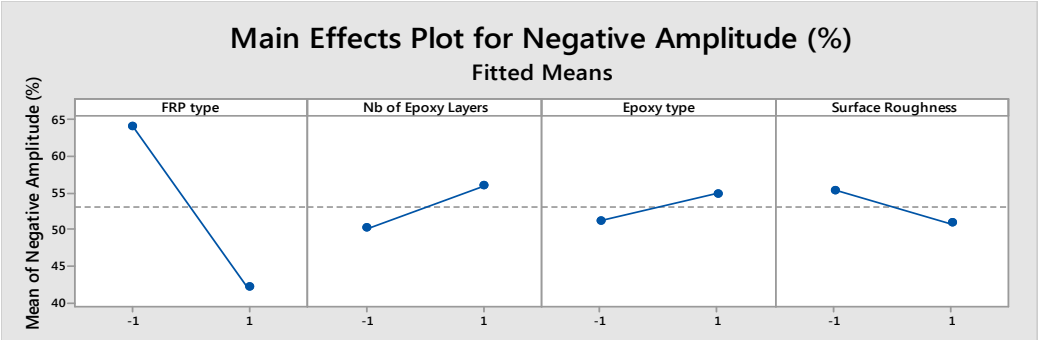

Figure 4- 54: Main Effect of the parameters

The interaction plot is presented in Figure 4- 53. The interaction plot shows that there is no interaction between the surface roughness and the number of Epoxy Layers used or the Epoxy type. The graph shows that there is an interaction between the FRP type and the number of Epoxy Layers used. Also, it seems that there is an interaction between the number of Epoxy type and the Epoxy type.

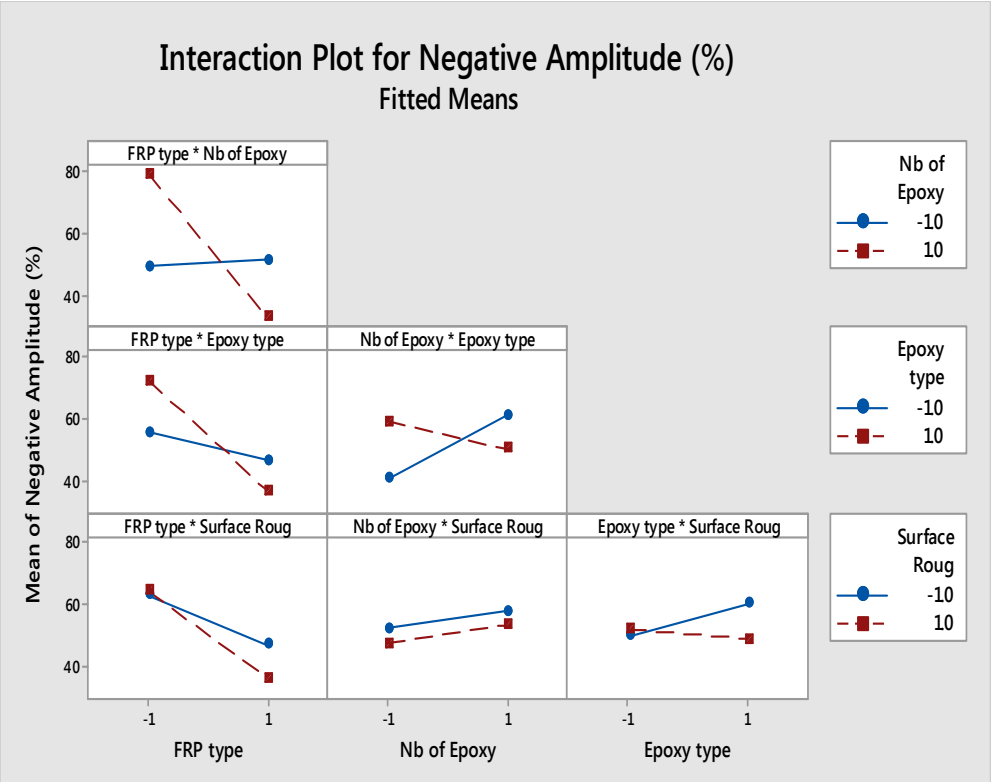

Figure 4- 55: Interaction plot for the amplitude value

Finally, to study the significance of each of the main parameters and the interaction between them, the ANOVA table prepared by Minitab is presented in Table 4- 4. The model has an R square of 87.64%.

Table 4- 4: Analysis of variance for the GPR test

Source	DF	Adj SS	Adj MS	F-Value	P-Value
Model	10	6412.66	641.27	3.55	0.087
Linear	4	2225.77	556.44	3.08	0.125
FRP type	1	1952.64	1952.64	10.80	0.022
Nb of Epoxy Layers	1	135.21	135.21	0.75	0.427
Epoxy type	1	55.04	55.04	0.30	0.605
Surface Roughness	1	82.87	82.87	0.46	0.528
2-Way Interactions	6	4186.89	697.82	3.86	0.080
FRP type*Nb of Epoxy Layers	1	2315.53	2315.53	12.80	0.016
FRP type*Epoxy type	1	684.09	684.09	3.78	0.109
FRP type*Surface Roughness	1	142.51	142.51	0.79	0.415
Nb of Epoxy Layers*Epoxy type	1	854.54	854.54	4.73	0.082
Nb of Epoxy Layers*Surface Roughness	1	0.49	0.49	0.00	0.961
Epoxy type*Surface Roughness	1	189.73	189.73	1.05	0.353
Error	5	904.25	180.85		
			91		

S	R-sq	R-sq(adj)	R-sq(pred)
13.4481	87.64%	62.92%	0.00%

The model prepared by Minitab present an equation that could be used in estimating the expected negative amplitude value for a specific beam. The estimated negative amplitude value is useful in the evaluation of the FRP application process. The Amplitude value can provide a base for quality inspection and assurance. The equation for estimating the Amplitude value is presented as follows.

$$\text{Negative Amplitude (\%)} = 53.04 - 11.05\,[\text{FRP type}] + 2.91\,[\text{Nb of Epoxy Layers}] + 1.85\,[\text{Epoxy type}] - 2.28\,[\text{Surface Roughness}] - 12.03\,[\text{FRP type} * \text{Nb of Epoxy Layers}] - 6.54\,[\text{FRP type} * \text{Epoxy type}] - 2.98\,[\text{FRP type} * \text{Surface Roughness}] - 7.31\,[\text{Nb of Epoxy Layers} * \text{Epoxy type}] + 0.17\,[\text{Nb of Epoxy Layers} * \text{Surface Roughness}] - 3.44\,[\text{Epoxy type} * \text{Surface Roughness}] \quad \text{Eq. (4-5)}$$

Where, FRP type is -1 for FRP type I and +1 for FRP type II. Similarly, for each parameter in the previous equation, a value of -1 is assigned to the type I and a value of +1 is assigned to type II.

In this section, a simple approach is presented to identify and locate any voids and delamination that might be hidden under the FRP surface. The method depends on the visual analysis of the B-scan of each beam to identify the presence of hidden voids. Samples of the results are presented in Figure 4- 54 and Figure 4- 55. The pictures show that the GPR device could be used for the detection of voids. From these two pictures, the location and the size of the voids could be determined and used to assess their effect on the overall strength of the bond.

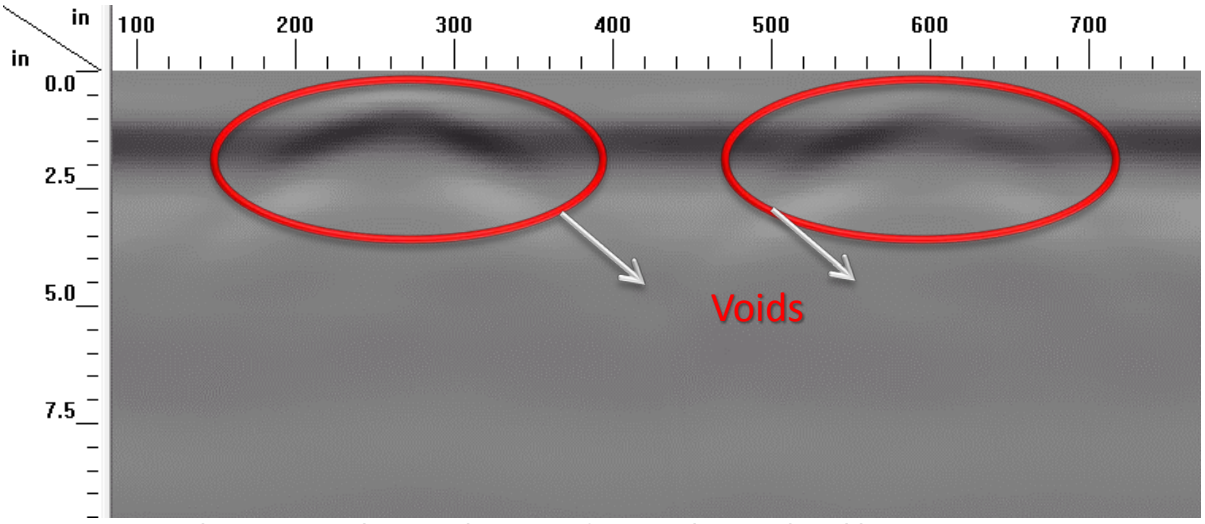

Figure 4- 56: Ultrasound B-scan of two 1.6 in × 1.6 in voids

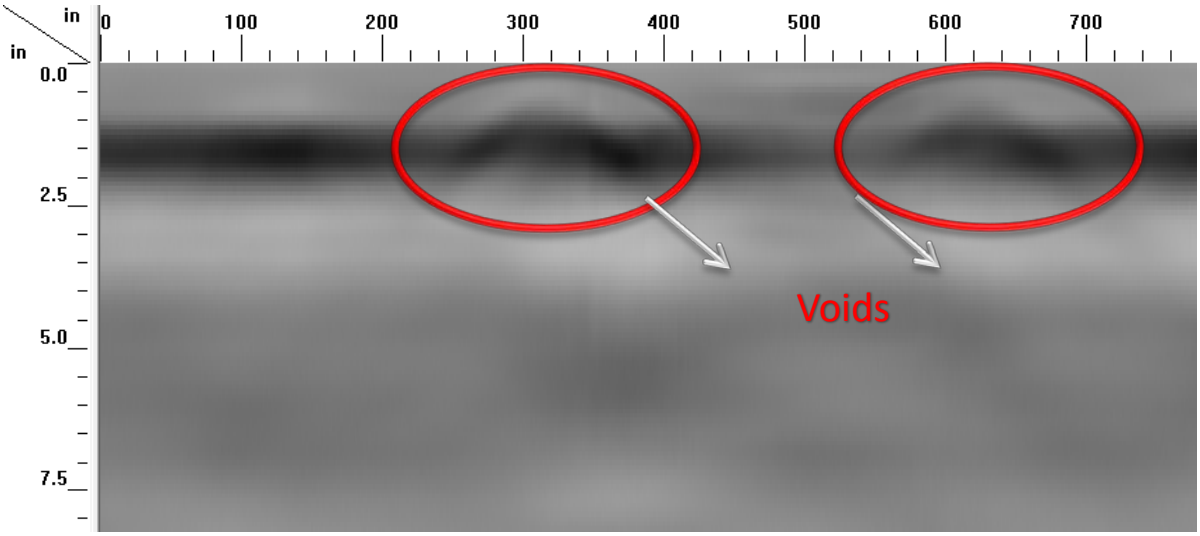

Figure 4- 57: Ultrasound B-scan of two 0.8 in × 0.8 in voids

In the previous approach, the reflected wave considered in the analysis is within the direct coupling. In this zone, several reflections from the antenna and the top surface of the beam are included. Therefore, the reading contains noises that affect the interpretation of the results. Hence, a new approach was considered in this section. The new approach rely on attaching an additional material with a known dielectric constant.

The thickness of the additional material taken more than the thickness of the direct coupling zone. In this case, the noises and the surface reflection are recorded within the thickness of the additional material which leaves the data under consideration clear of any unwanted disturbance. Figure 4- 56 illustrates the configuration of the new approach. A layer of foam, wood and concrete were used in this study.

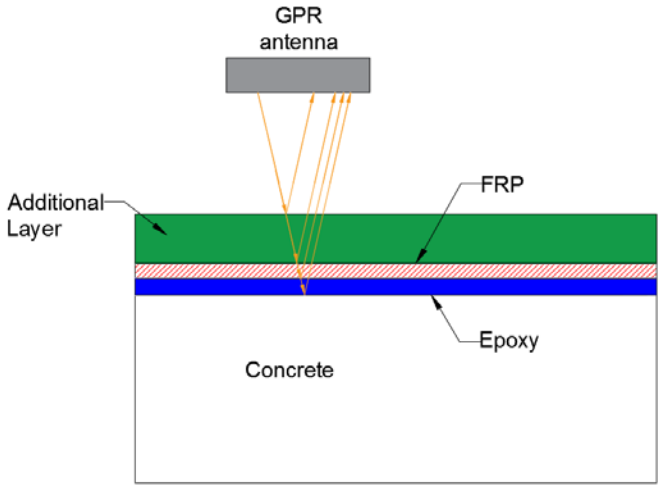

Figure 4- 58: GPR test configuration after adding the additional layer

The data of this test was analyzed using the Minitab software. Following are some of the results of the design of experiment using Minitab software. Figure 4- 57 examine the assumption that the residuals are approximately normally distributed, are independent and have equal variances. The four charts show a large spread of the data and that there is no clear pattern of the residuals. The residuals do appear to have approximately, a normal distribution.

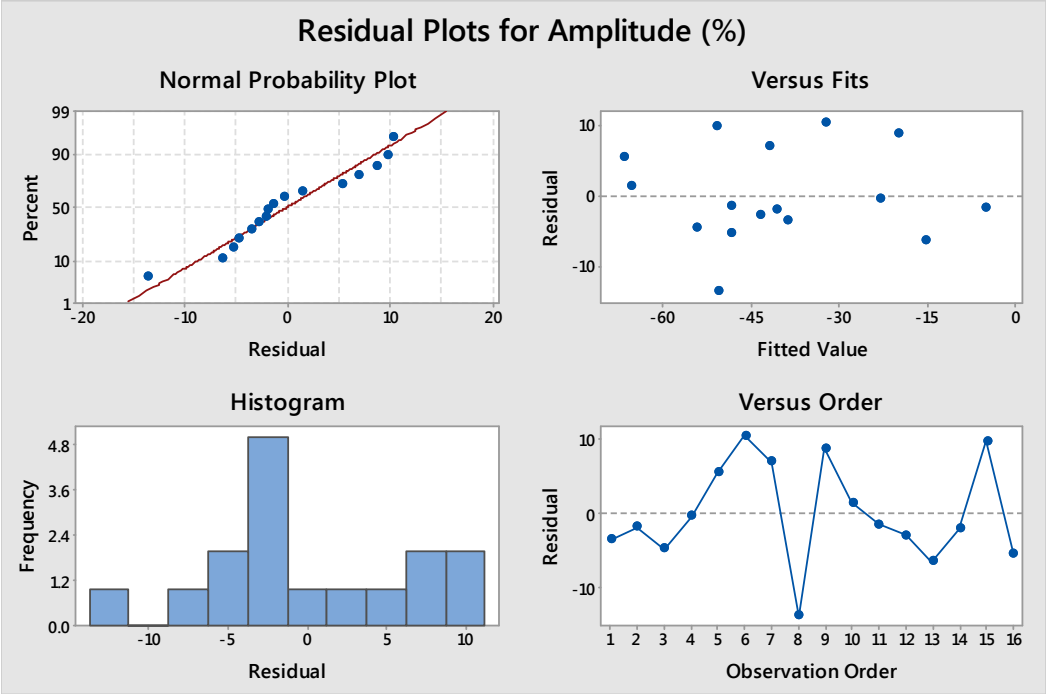

Figure 4- 59: Residual Plots for the amplitude (%)

Next step, to look at the plots of responses versus each parameter as presented in Figure 4- 58. The plot shows each parameter versus the percentage change of the amplitude value of the FRP surface relative to the amplitude value of the concrete surface. The first chart of the amplitude (%) versus the FRP type shows that the amplitude tends to decrease with the increase in the thickness of the FRP layer. The plot of the number of epoxy layers shows that adding an extra layer of Epoxy increase the amplitude reading. For the Epoxy type, the chart shows that the Epoxy with higher viscosity tends to decrease the amplitude value. Finally, surface preparation does not seem to have an effect on the amplitude value.

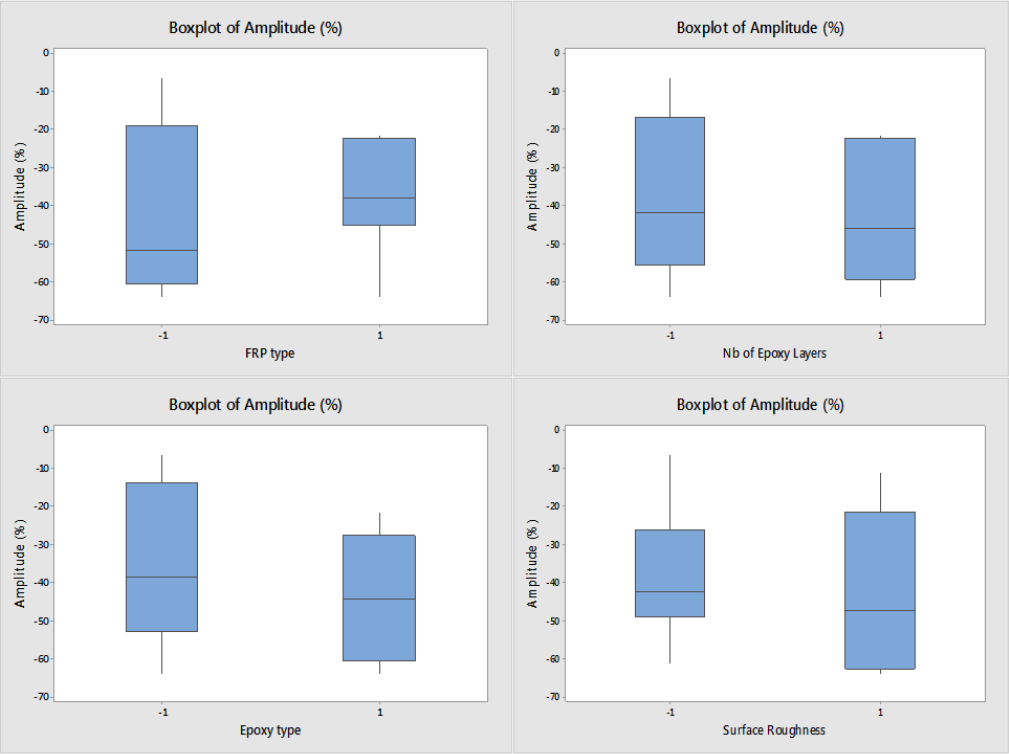

Figure 4- 60: Plots of responses versus each parameter

Minitab software presents the effect of each of the main parameters in a combined figure as illustrated in Figure 4- 59. The interaction plots is illustrated in Figure 4- 60.

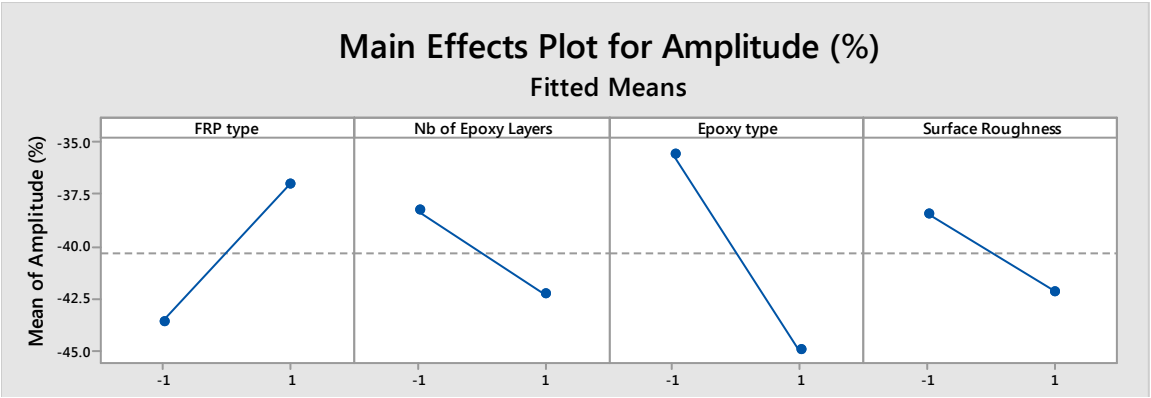

Figure 4- 61: Main Effect of the parameters

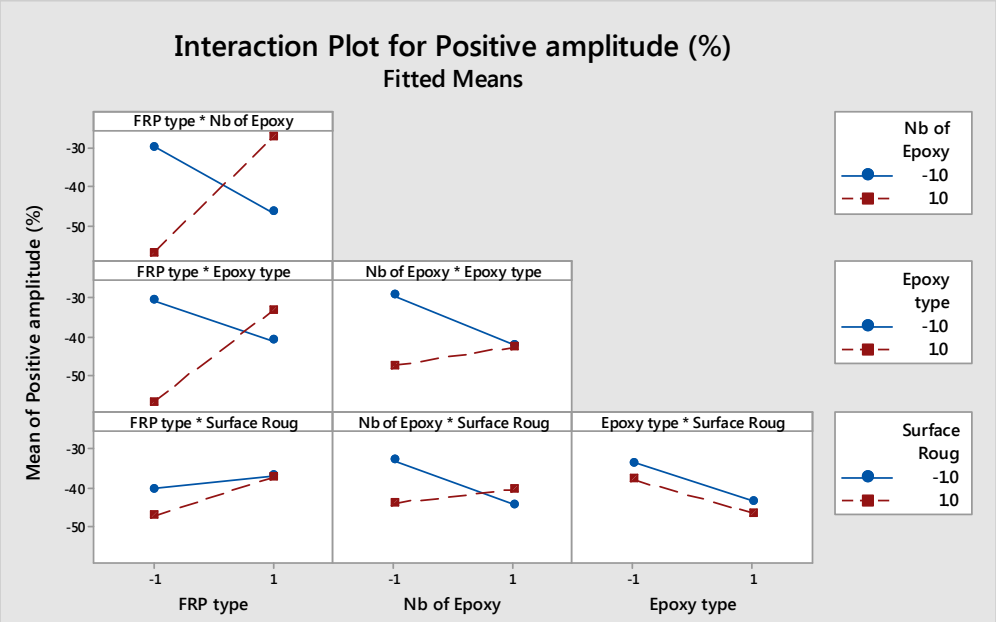

Figure 4- 62: Interaction plots of the parameters

Equation 4-5 prepared by Minitab software could be used in estimating the expected positive amplitude value for a specific beam. The estimated positive amplitude value is useful in the evaluation of the FRP application process. The Amplitude value can provide a base for quality inspection and assurance. The equation for estimating the Amplitude value is presented as follows:

Negative Amplitude (%) Eq. (4-6)

$$= -40.30 + 3.31\,[\text{FRP type}] - 2.00\,[\text{Number of Epoxy Layers}] - 4.67\,[\text{Epoxy type}] - 1.87\,[\text{Surface Roughness}] + 11.70\,[\text{FRP type} * \text{Nb of Epoxy Layers}] + 8.51\,[\text{FRP type} * \text{Epoxy type}] + 1.60\,[\text{FRP type} * \text{Surface Roughness}] + 4.37\,[\text{Number of Epoxy Layers} * \text{Epoxy type}] + 3.75\,[\text{Number of Epoxy Layers} * \text{Surface Roughness}] + 0.30\,[\text{Epoxy type} * \text{Surface Roughness}]$$

Where, FRP type is -1 for FRP type I and +1 for FRP type II. Similarly, for each parameter in the previous equation, a value of -1 is assigned to the type I and a value of +1 is assigned to type II.

Table 4- 5: Analysis of variance for the GPR test after covering the sample with additional layer

Source	DF	Adj SS	Adj MS	F-Value	P-Value
Model	10	4569.01	456.90	3.42	0.093
Linear	4	644.65	161.16	1.21	0.411
FRP type	1	175.40	175.40	1.31	0.304
Nb of Epoxy Layers	1	64.22	64.22	0.48	0.519
Epoxy type	1	349.22	349.22	2.62	0.167
Surface Roughness	1	55.82	55.82	0.42	0.546
2-Way Interactions	6	3924.35	654.06	4.90	0.051
FRP type*Nb of Epoxy Layers	1	2191.10	2191.10	16.41	0.010
FRP type*Epoxy type	1	1159.32	1159.32	8.68	0.032
FRP type*Surface Roughness	1	40.86	40.86	0.31	0.604
Nb of Epoxy Layers*Epoxy type	1	306.09	306.09	2.29	0.190
Nb of Epoxy Layers*Surface Roughness	1	225.53	225.53	1.69	0.250
Epoxy type*Surface Roughness	1	1.46	1.46	0.01	0.921
Error	5	667.69	133.54		
Total	15	5236.69			

S	R-sq	R-sq(adj)	R-sq(pred)
11.5558	87.25%	61.75%	0.00%

Chapter 5

Destructive testing

Introduction

In order to evaluate the effect of the FRP type, Epoxy type, number of Epoxy layer, surface roughness and voids on the bond FRP to concrete bond strength, a series of destructive testing were performed. In this chapter, the results of these destructive testing are presented. The first destructive test considered in this study is the pull-off test. The pull-off test was selected to highlight the strength of the bond under tension. The second destructive test presented is the bending test. The bending test highlights the strength of the bond in flexure.

Pull-off Test

The pull-off test method determines the greatest tension force (applied perpendicular to the surface) that the FRP–epoxy–concrete bond can resist. The method consists of adhesively bonding a metallic circular loading fixture (dolly) normal to the testing surface as illustrated in Figure 5- 1. After attaching the dolly, a tension force is applied gradually using the pull-off test device until the detachment of the dolly is witnessed. A load of rupture recorded is regarded as the maximum bond force [ASTM D7522/D7522M-15, 2015]. The observed modes of failure also can shed light on the condition of the epoxy–FRP–concrete interface.

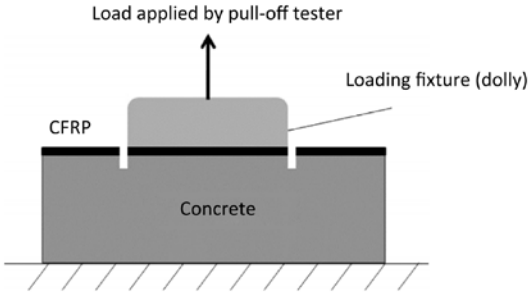

Figure 5- 1: Pull-off test mechanism

According to [ASTM D7522/D7522M-15, 2015], seven failure modes are possible depending on the location of failure interface, Mode A through Mode G, as shown in Figure 5- 2. Mode A corresponds to Epoxy failure at the dolly interface. Mode B corresponds to failure in the FRP laminate. Mode C corresponds to a failure at the FRP/Epoxy interface. Mode D corresponds to a failure within the Epoxy layer. Mode E corresponds to a failure in the concrete/Epoxy interface. Mode F corresponds to a mixed failure in the Epoxy/concrete interface and in the concrete substrate. Finally, Mode G corresponds to a failure in the concrete substrate. The additional mode of failure Mode M considers mixed failure was proposed by [Pallempati et al., 2016].

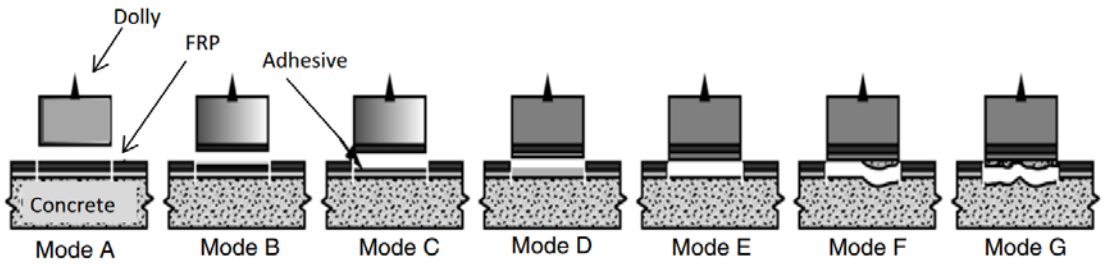

Figure 5- 2: Pull-off test mechanism

In this study, each sample was tested following the ASTM pull-off test to evaluate the bond strength in tension. Two pull off tests were performed for each sample with a diameter of 2 inches. The locations of the pull-off test are illustrated in Figure 5- 3. The location of the pull-off test is selected at the supports location to reduce any effect on the bending test.

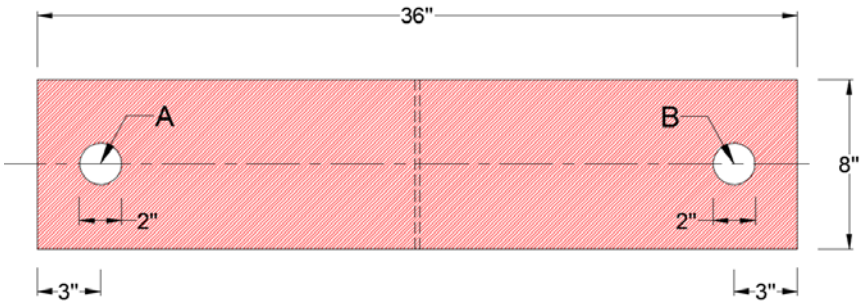

Figure 5- 3: Pull-off test locations.

The first step in the preparation for the pull-off test was to cut around the dolly. A circular hole with the diameter of the dolly at the location of each test. This step ensures that the effect of the test is limited to the dolly size and do not extend to the FRP surface. A coring drill bit was attached to a drill machine as illustrated in Figure 5- 4. A hole with a depth of 0.125 in was prepared for each test location.

Figure 5- 4: Core drilling

After drilling the hole at the concrete surface, sandpaper was used to prepare the surface. The area was then cleaned with acetone to remove dirt, dust and other particles. Water was used to clean off the acetone from the surface. To remove oxidation and contaminants, an abrasive pad on a flat surface was used to rub the base of the dolly shown Figure 5- 5.

Figure 5- 5: Two inch diameter dolly

The next step was to attach the dolly to the surface of the beams using adhesive. A fast setting epoxy was used to attach the dollies. The Epoxy was mixed using a wooden stick the applied to the dolly surface. The surface of the dolly was completely covered with epoxy as illustrated in Figure 5- 6 then placed over the concrete surface.

Figure 5- 6: Epoxy application to dolly surface

The dollies were attached to the concrete surface as illustrated in Figure 5- 7. Two dollies were attached at the ends of each sample. The Epoxy as left to dry for 24 hours before the pull-off test.

Figure 5- 7: Dollies attached to concrete surface

The “Posi-Test AT” Pull-Off Adhesion Tester was used in this study as shown in Figure 5-8. The pull-off tester measures the force required to pull a specified test diameter of coating away from its substrate using hydraulic pressure. The pressure is displayed on a digital LCD and represents the bond strength of adhesion to the substrate.

Figure 5- 8: Pull-off tester

The pull- off tester was used to test the bond strength of all the beams. The actuator handle was placed over the dolly head until it was completely engaged. After attaching the handle, the test was initiated and the instrument begins building pressure (priming stage). When the priming pressure was achieved the LCD started displaying pressure over time on the pull chart. Pressure build-up until the dolly is pulled from the surface as shown in Figure 5- 9. The maximum pressure value and the failure mode were recorded for each dolly.

Figure 5- 9: Dolly pulled from beam surface

The test results are presented in Table 5- 1. The table presents the failure stress and the failure mode from each dolly. Several mixed failure mode were recorded from the pull-off test. The results from this test to be used for determining the effect of each parameter on the bond strength in tension.

Table 5- 1: Summary of Pull-off test results

Beam type	***Pull-off test location***	***Failure Stress (psi)***	***Failure Mode***
1	A	380	G (90% G)
1	B	332	G (95% G)
1'	A	322	G (99% G)
1'	B	424	G (95% G)
2	A	306	M (85 % G 15% E)

2	B	449	M (50% G 50% E)
2’	A	481	M (75% G 25% E)
2’	B	400	M (50% G 50% E)
3	A	460	G (100% G)
3	B	447	G (100% G)
3’	A	407	G (100% G)
3’	B	424	G (100% G)
4	A	287	G (100% G)
4	B	560	F (85% G 15% C)
4’	A	415	F (85% G 15% C)
4’	B	454	G (90% G)
5	A	493	G (95% G)
5	B	454	G (95% G)
5’	A	460	G (100% G)
5’	B	525	G (99% G)
6	A	560	G (90% G)
6	B	560	M (80% G 20% E)
6’	A	560	M (80% G 20% E)
6’	B	530	M (70% G 30% E)
7	A	143	G (90% G)
7	B	519	G (100% G)
7’	A	557	G (100% G)
7’	B	560	G (100% G)
8	A	378	G (100% G)
8	B	377	G (100% G)
8’	A	281	G (100% G)
8’	B	374	G (100% G)
9	A	261	G (95% G)
9	B	299	G (95% G)
9’	A	325	G (100% G)
9’	B	263	G (95% G)
10	A	360	M (55% G 45% E)
10	B	560	M (80% G 20% E)
10’	A	350	G (95% G)
10’	B	347	G (95% G)
11	A	468	A (100% A)
11	B	398	F (60% G 40% C)

11'	A	346	G (100% G)
11'	B	300	G (100% G)
12	A	329	A (100% A)
12	B	354	C (100% C)
12'	A	446	G (100% G)
12'	B	490	G (100% G)
13	A	402	G (95% G)
13	B	442	G (98% G)
13'	A	282	A (100% A)
13'	B	455	G (95% G)
14	A	507	M (75% G 25% E)
14	B	70	M (60% G 40% E)
14'	A	215	M (40% G 60% E)
14'	B	545	G (90% G)
15	A	476	G (100% G)
15	B	461	G (100% G)
15'	A	460	G (100% G)
15'	B	382	G (100% G)
16	A	418	G (100% G)
16	B	522	G (100% G)
16'	A	371	A (100% A)
16'	B	490	G (100% G)

Figure 5- 10 shows a selected sample from the pull-off failure modes. The majority of the test failed according to ASTM-Mode G failure as shown in Figure 5- 10 (a). A total of 44 test failed in Mode G. Three test failed according to another ASTM mode of failure described as Mode F as shown in Figure 5- 10 (b). Twelve test shows a Mode M failure as shown in Figure 5- 10 (c). Only one test shows a Mode C failure as shown in Figure 5- 10 (d). Finally four test record a Mode A failure was the dolly wasn't adequately attached to the surface of the beam.

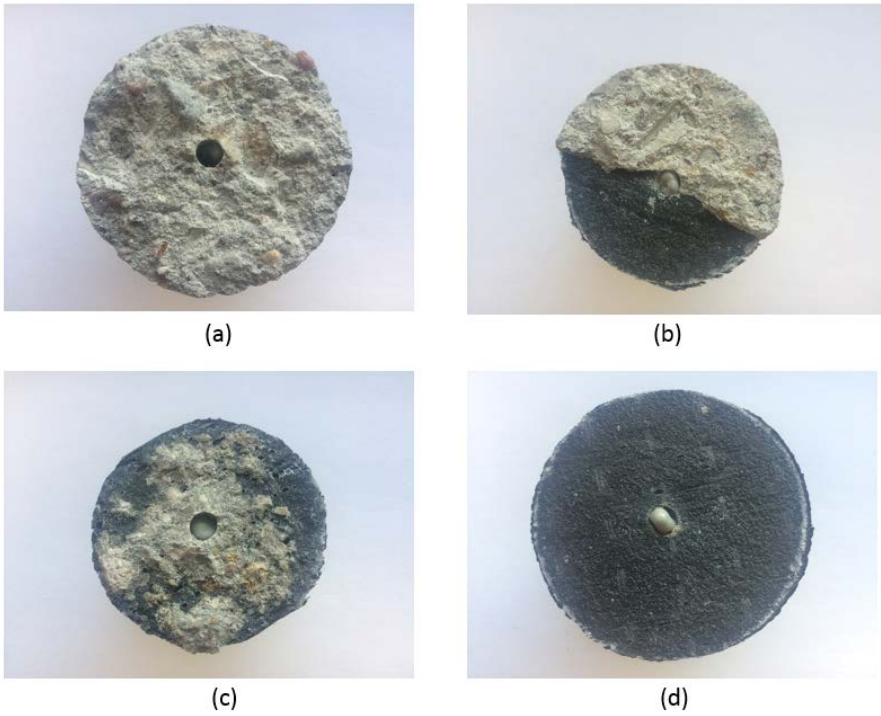

Figure 5- 10: Various observed failure modes:

(a) Mode G; (b) Mode F; (c) Mode M; (d) Mode C

To analyze the data and determine the effect of each parameter on the failure stress of the pull-off test, Minitab software package for statistical analysis was used. The input values are the failure stress of each beam. Following are some of the results of the design of experiment using Minitab software.

The first step is plotting the data several ways to see if any trends or anomalies appear that would not be accounted for by the model. Figure 5- 11 illustrates the four plots of the residuals generated by Minitab: a normal probability plot, residuals versus the fitted values, histogram and a run-order plot of the residuals. The four charts show the spread

of the data and indicate that there is no clear pattern of the residuals. The residuals do appear to have a normal distribution.

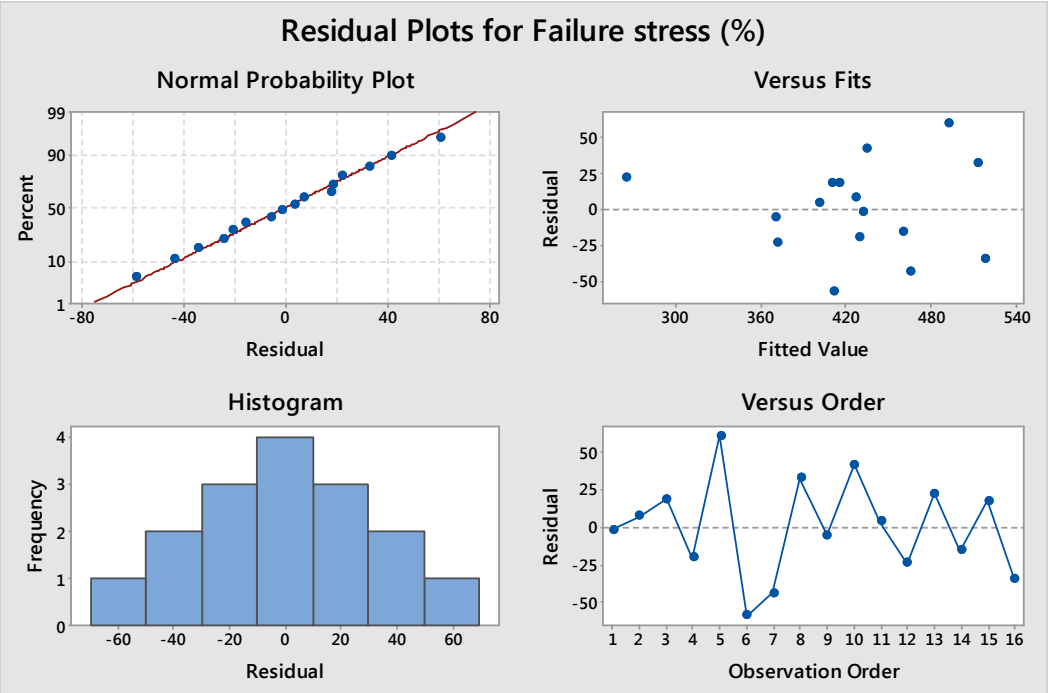

Figure 5- 11: Residual Plots for pull-off test

Next step, to look at the plots of responses versus each parameter as presented in Figure 5- 12. The graph shows that the FRP type and the number of Epoxy layers used have much less impact on the failure stress compared to the type of Epoxy used. The strength of the bond in tension increase while using the Sikadur 330 versus the Sikadur 300. Sandblasting the concrete surface improve the contact and increase the strength of the bond in tension compared to use the technique of hand grinding in preparing the surface of the concrete.

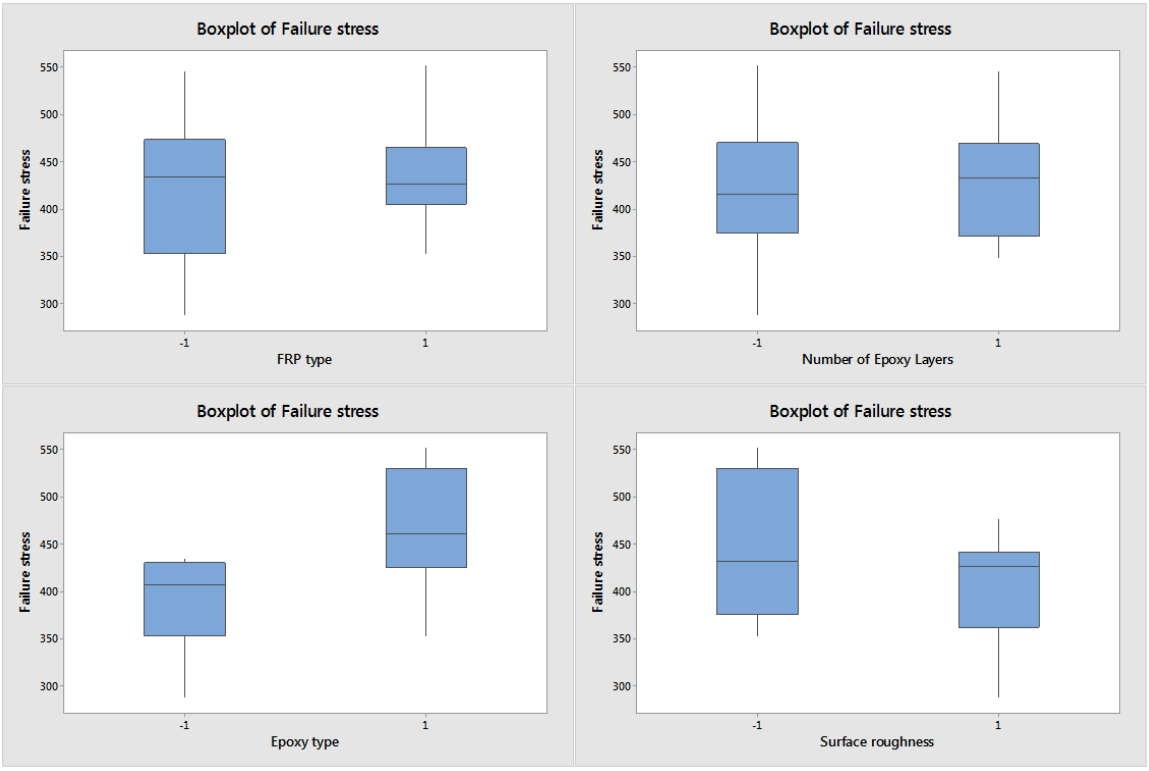

Figure 5- 12: Plots of the failure stress versus each parameter

To investigate the main effects, Minitab software presents the effect of each of the main parameters in a combined figure as illustrated in Figure 5- 13. The graph shows that the Epoxy type has the highest effect among all the parameters compared to the other parameters considered. The FRP type and the number of Epoxy layers used seems to have the lowest effect on the bond strength.

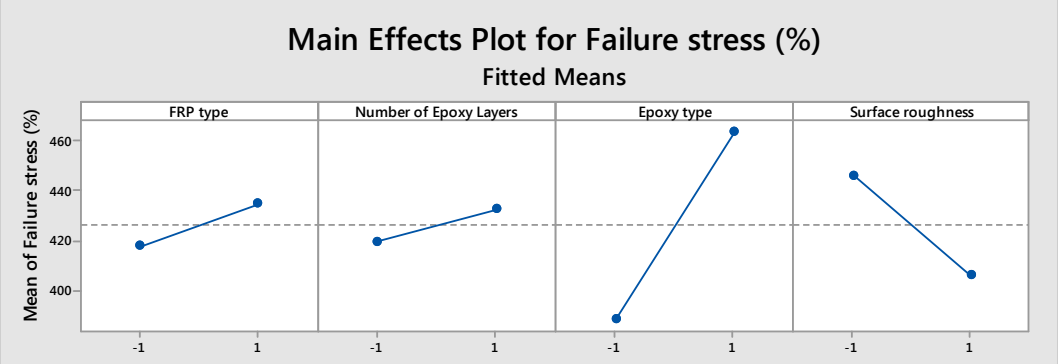

Figure 5- 13: Main Effect of the parameters

The interaction plot is presented in Figure 5- 14. The interaction plot shows that there is no interaction between the Epoxy type and the surface roughness. The graph also shows that the highest interaction is between the FRP type and number of Epoxy layer used.

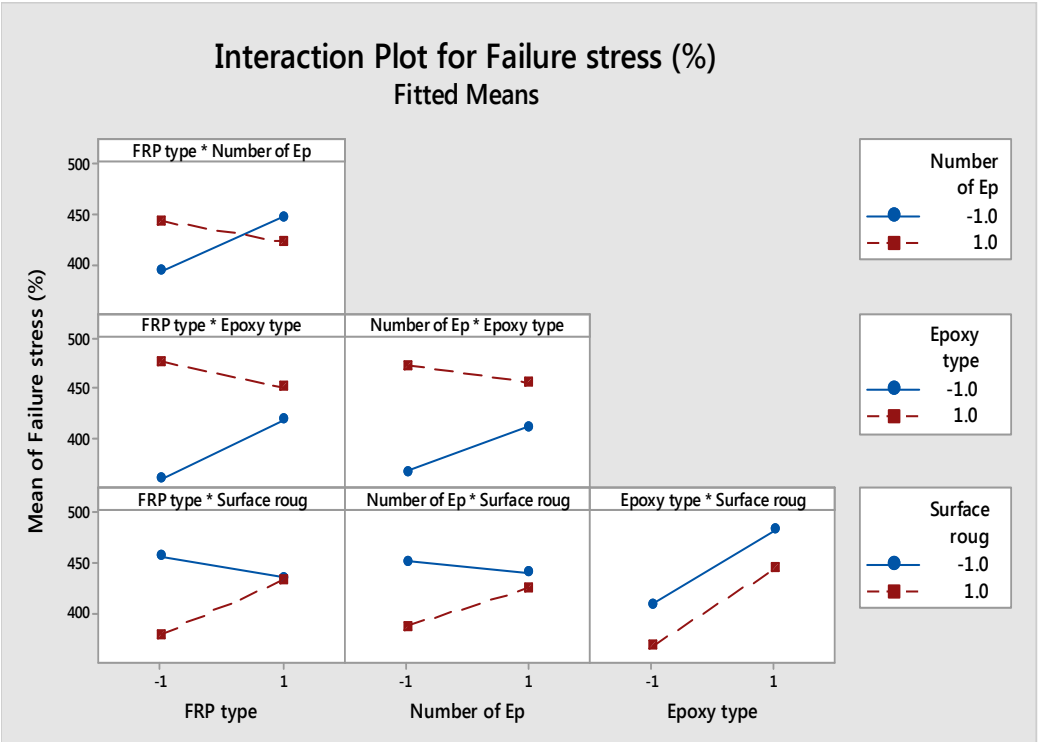

Figure 5- 14: Interaction plot for the rate of cooling down

The results from the pull-off test presented in the above section to be used for calibration purposes of the finite element model. The Finite element model presented in the following chapters uses the results as input properties of the contact between the FRP and concrete. The values from the pull-off test correspond to the normal stiffness of the bond in the FE model.

Three points bending test

The bending test determines the flexural properties (including strength, stiffness, and load/deflection behavior) of the beam strengthened with FRP. A three-point loading system utilizes a center loading on a simply supported beam. In this method, the beam rests on two supports and is loaded by means of a loading nose midway between the supports as illustrated in Figure 5- 15. The specimen is loaded continuously and without shock at a constant rate to the breaking point.

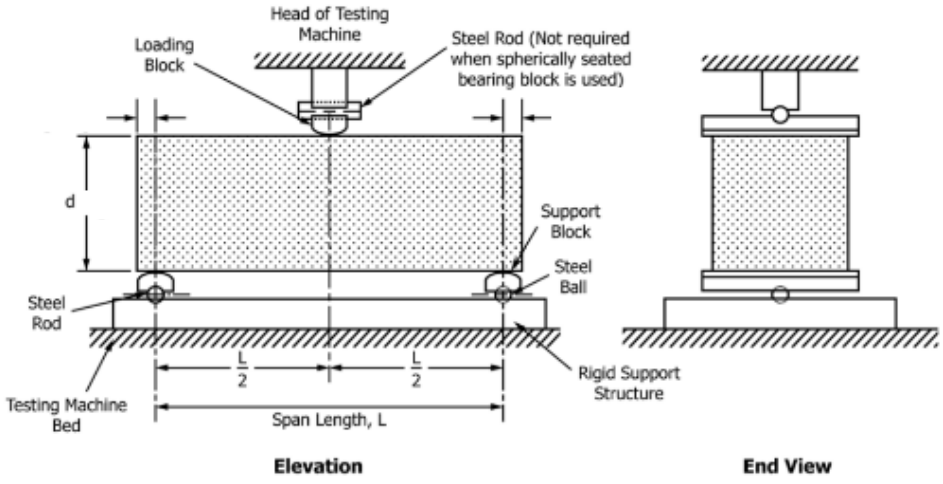

Figure 5- 15: Schematic Apparatus for Flexure Test of Concrete by Three Point Loading Method [ASTM C293/C293M, 2016]

ACI 440 committee define several failure modes for beams. The flexural strength of a section depends on the controlling failure mode. The following flexural failure modes are possible for an FRP-strengthened section [ACI 4402R-17, 2017]: Crushing of the concrete in compression before yielding of the reinforcing steel, yielding of the steel in tension followed by rupture of the FRP laminate, yielding of the steel in tension followed by concrete crushing, Shear/tension delamination of the concrete cover (cover delamination) and Debonding of the FRP from the concrete substrate (FRP debonding).

Cover delamination or FRP debonding can occur if the force in the FRP cannot be sustained by the substrate. Such behavior is generally referred to as debonding, regardless of where the failure plane propagates within the FRP-adhesive-substrate region. Figure 5- 16 shows the Debonding and delamination of externally bonded FRP systems.

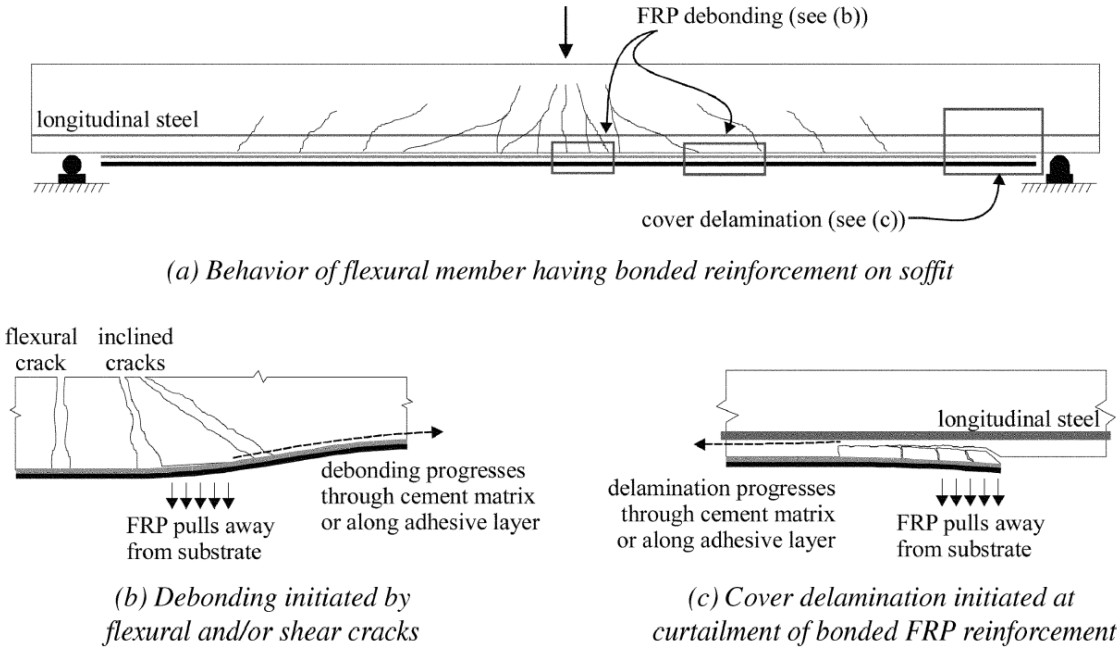

(a) Behavior of flexural member having bonded reinforcement on soffit

(b) Debonding initiated by flexural and/or shear cracks

(c) Cover delamination initiated at curtailment of bonded FRP reinforcement

Figure 5- 16: Debonding and delamination of externally bonded FRP systems [ACI 440, 2017]

In this study for each sample, the bending beam test was performed as an indication of the strength of the bond in bending. The test setup is illustrated in Figure 5- 17. Two strain gages were attached to each beam. The first strain gage is attached to the FRP layer at mid-span to capture strain corresponding to the maximum tensile stress at the bottom of the beam section. The second strain gage is attached to the top of the concrete beam to record the strain corresponding to the maximum compressive strain at the top of the beam. An additional strain gage was attached to FRP layer at mid-span in only 16 of the 32 beams to verify the reading from the first strain gage.

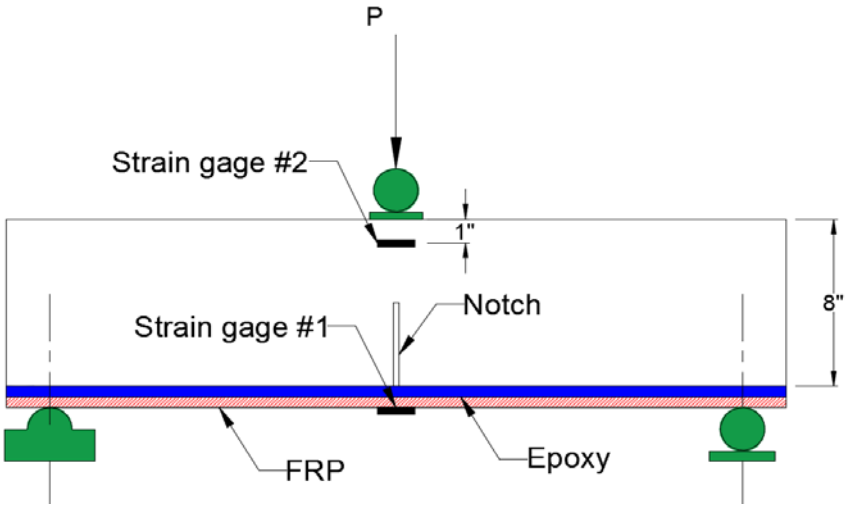

Figure 5- 17: Bending test setup

Two displacement transducers (LVDT) were used to record the displacement at the mid-span during the bending test. The LVDT were placed at both sides at the mid-span of the beam as in the side view shown in Figure 5- 18.

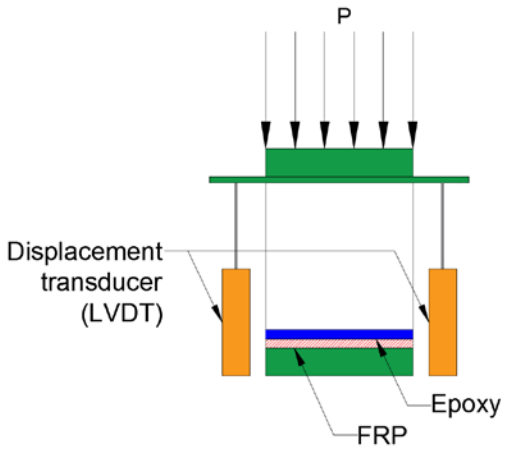

Figure 5- 18: Displacement transducer location

Figure 5- 19 shows the strain gages attached to the concrete beam. The installation of strain gages on the concrete surface requires a detailed process which had to be followed to assure all the gages are properly attached. Strain gages on the concrete and FRP have different processes for installation. The installation of strain gages in the concrete surface involves the following steps:

1. The locations for the installation of strain gages were marked on the concrete surface and the FRP.
2. The surface was made smooth by sanding or grinding so that the surface was uniform and even.
3. The area was then cleaned with acetone to remove dirt, dust and other particles. Water was used to clean off the acetone from the surface.
4. A fast setting epoxy was used as backing for the strain gages to fill the voids in the concrete and provide a smooth surface. This epoxy was used only for the concrete surface.

5. The epoxy was allowed to dry properly and Tokyo Sokki strain gages were attached with the use of the CN and CN-E adhesive for both the FRP and concrete surface respectively.

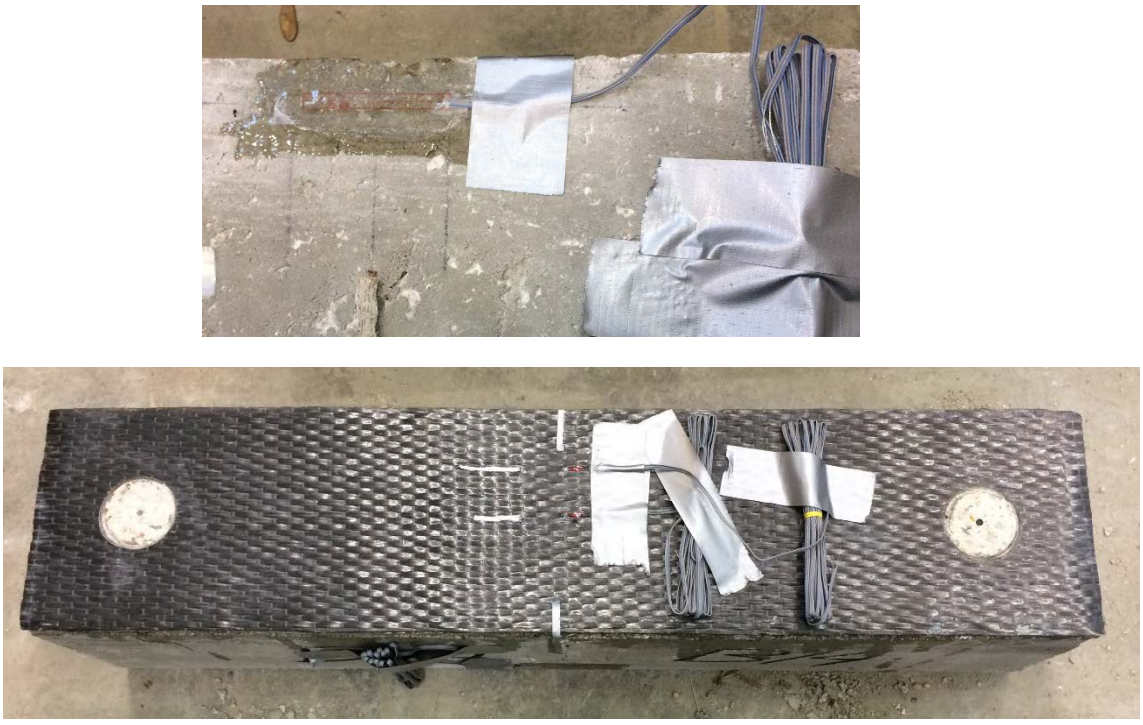

Figure 5- 19: Concrete and FRP Strain gages

After attaching the strain gages to the beams, the epoxy was left to dry for 24 hours. Figure 5- 20 shows the concrete beams after attaching the strain gages. The beams were ready for the bending test.

Figure 5- 20: Strain gages attached to the concrete beams

After preparing the beams for the test, a 400 kip compression test machine was used. Figure 5- 21 shows the setup for the test. The beam was supported on two rollers where one was restrained from movement to represent a hinged support and the other was allowed to move to represent the roller support. A plate was placed on top of the beam at the mid-span to distribute the load uniformly at the total width of the beam.

Figure 5- 21: Setup of the three points bending test

The 400 kip compression machine was connected to a computer to record the applied load and displacement and to control the rate of loading. For this test, a load rate of 0.05 lb/min was selected. All strain gage wires were connected to the data acquisition system as illustrated in Figure 5- 22. Two LVDT to measure the displacement also were connected to the DAQ. A Tokyo Sokki DS750 DAQs was used to collect the data at 100 Hz. The system was connected to a laptop to record a view the data.

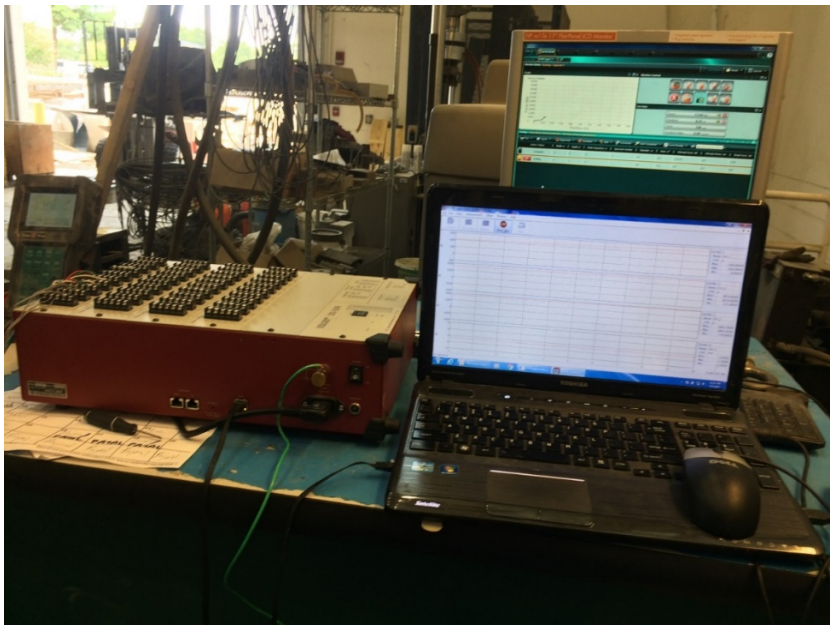

Figure 5- 22: Data acquisition system

The test results are presented in Table 5- 2. The table presents the failure load and the failure mode from each dolly. The failure modes defined in this table are taken similar to the failure mode defined by the ASTM to describe the failure of the pull-off test. The results from this test to be used for determining the effect of each parameter on the bond strength in bending.

Table 5- 2: Summary of three points bending test

Beam type	***Pull-off test location***	***Failure Load (lb.)***	***Failure Mode***
1	A	1190	80% G 20% E
1	B	7790	30% G 70% E
2	A	12600	10% G 90% E
2	B	11300	10% G 90% E

3	A	11300	100% G
3	B	9720	100% G
4	A	15000	100% C
4	B	15200	100% G
5	A	9580	50% G 50% E
5	B	8950	50% G 50% E
6	A	11800	20% G 80% E
6	B	13700	30% G 70% E
7	A	11700	100% G
7	B	10600	100% G
8	A	5510	100% G
8	B	12500	100% G
9	A	5320	50% G 50% E
9	B	6630	30% G 70% E
10	A	10100	5% G 95% E
10	B	8920	70% G 30% E
11	A	5820	100% G
11	B	8810	100% G
12	A	12500	100% G
12	B	14300	100% G
13	A	6100	100% G
13	B	10500	50% G 50% E
14	A	1190	20% G 80% E
14	B	11600	10% G 90% E
15	A	12500	100% G
15	B	10400	100% G
16	A	10000	100% G
16	B	13700	100% G

Figure 5- 23 shows a selected sample from the three points bending. With the application of loads, the started to deflect to a point where flexure cracks started to appear at mid-span. These flexure cracks lead to debonding between the FRP and the concrete. The debonding progressed from the mid-span toward the edge of the beam with the increase

of loading until failure. The failure happened when the FRP layer was completely debonded from the FRP.

Figure 5- 23: Three points bending test failure

Figure 5- 24 illustrates the debonded FRP sheet from the concrete surface. The majority of the test failed according to Mode G failure where part of the concrete cover is attached to the FRP layer. Only one beam failed according to Mode C where the failure happens

at the edge between the Epoxy Layer and the FRP. Several mixed failure modes were recorded.

Figure 5- 24: Debonding of the FRP layer

To analyze the data and determine the effect of each parameter on the failure load of the three points bending test, Minitab software was used. The first step is plotting the data several ways to see if any trends or anomalies appear that would not be accounted for by the model. Figure 5- 25 illustrates the four plots of the residuals generated by Minitab: a normal probability plot, residuals versus the fitted values, histogram and a run-order plot of the residuals. The four charts show the spread of the data and indicate that there is no clear pattern of the residuals. The residuals do appear to have a normal distribution.

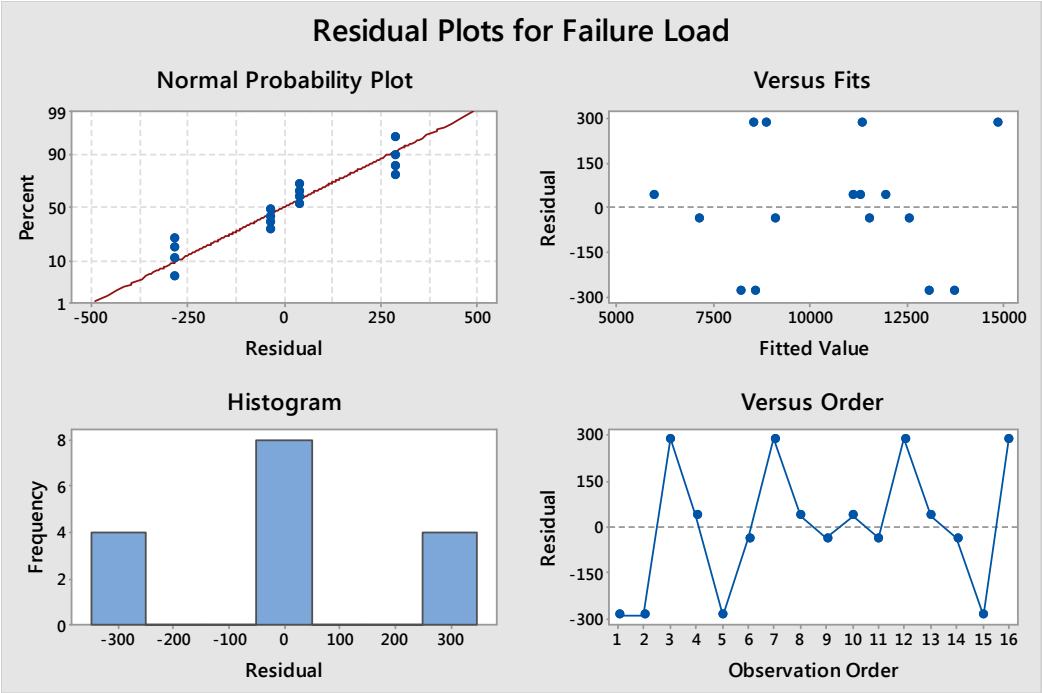

Figure 5- 25: Residual Plots of the three points bending test

Next step, to look at the plots of responses versus each parameter as presented in Figure 5- 26. The graph shows the effect of each parameter on the bond strength and consequently on the total load that the beam can carry. To have a better judgment on the effect of each parameter Minitab provide a figure showing the main effect of each parameter.

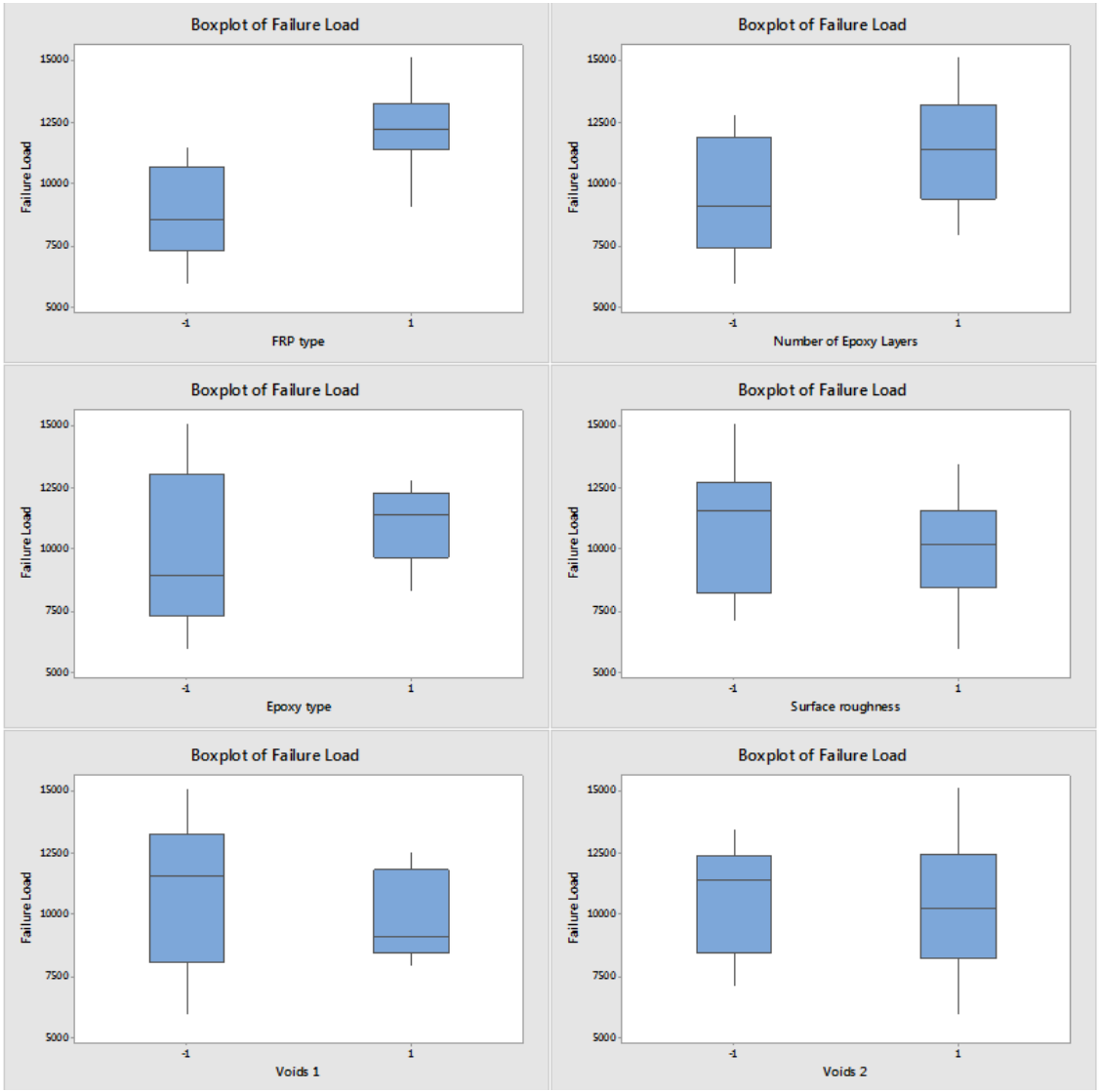

Figure 5- 26: Plots of the failure load versus each parameter

To investigate the main effects, Minitab software presents the effect of each of the main parameters in a combined figure as illustrated in Figure 5- 27. The graph shows that the FRP type has the highest effect among all the parameters followed by the number of Epoxy layers used and the large voids. The surface roughness and Epoxy type also

seem to have an effect on the bond strength. Finally, the small voids seem to have no effect on the overall beam capacity.

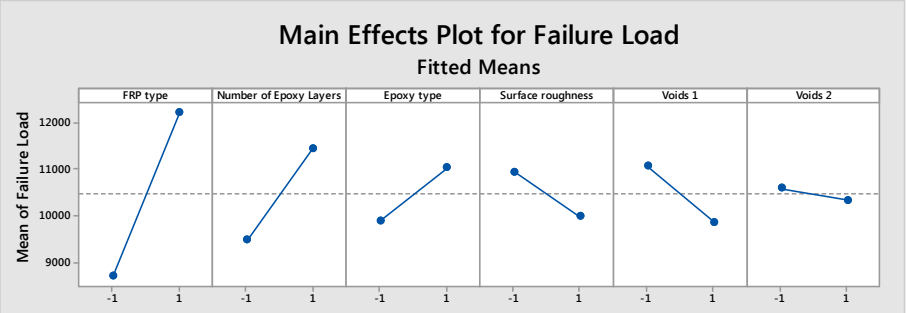

Figure 5- 27: Main Effect of the parameters

The interaction plot is presented in Figure 5- 28. The interaction plot shows there is an interaction between the voids and the number of Epoxy layers used. Also, there is an interaction between the voids and the surface roughness.

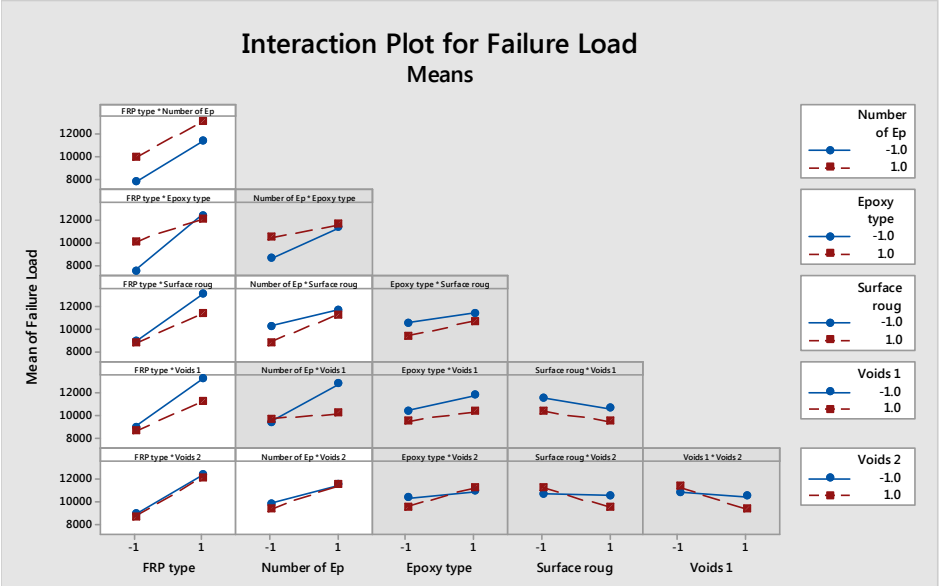

Figure 5- 28: Interaction plot for the three points bending test

The results from the bending test presented in the above section to be used for calibration purposes of the finite element model. The Finite element model presented in the following chapters uses the results as input properties of the contact between the FRP and concrete. The values from the bending test to be used to calibrate the contact properties of the bond in the FE model.

Chapter 6

Numerical Modelling

Introduction

The results obtained from the experimental analysis are used to construct a series of finite element models using the finite element software package ABAQUS. The finite element models are required to accurately reflect the effect of the parameters and their interactions on the bond strength with no aliases. The results from the calibrated FEM models are presented and compared to the findings of the experimental test.

Development of modeling framework

One main focus of this study is to develop a modeling framework to simulate the interaction between the FRP and concrete and capture the actual behavior of beams retrofitted with FRP. This involves several aspects of theoretical and practical interest. Important issues include material models, element types, mesh, convergence and boundary conditions. A general approach regarding these issues is presented in this study.

A Finite Element Model (FEM) was created using ABAQUS CAE [Simulia, 2011]. ABAQUS is a non-linear finite element software which has a wide array of modeling capabilities which allow modeling all kinds of different structural members, including CFRP, which is critical for this particular subject.

- The first material considered in this FE model is the concrete. In the last decade, many constitutive models which can predict the behavior of concrete, including cracks and crushing were developed. Two approaches are available in ABAQUS to predict the behavior of concrete: Brittle cracking model and concrete damage plasticity [Simulia, 2011]. The Brittle Cracking Model is designed for cases where

the overall material behavior is dominated by tensile cracking. It assumes that the compressive behavior of concrete is always linear elastic, which does not resemble reality and is a weakness of the model [Martin, 2010]. The concrete damage plasticity model assumes that the two main concrete failure mechanisms are cracking and crushing. Crack propagation is modeled by using continuum damage mechanics and stiffness degradation [Obaidat, 2011].

In this study, the concrete compressive and tensile properties were modeled as concrete damaged plasticity. ABAQUS uses the plasticity model proposed by [Lubliner et al. 1989]. The compressive and tensile behavior of concrete used is illustrated in Figure 6- 1. Figure 6- 1 (a) shows the behavior under uniaxial tension. The stress-strain response follows a linear elastic relationship until the value of the failure stress is reached. The failure stress corresponds to the onset of micro-cracking in the concrete material. Beyond the failure stress, the formation of micro-cracks is represented macroscopically with a softening stress-strain response, which induces strain localization in the concrete structure [Simulia, 2011].

Figure 6- 1 (b) shows the behavior under uniaxial compression, the response is linear until the value of initial yield is reached. In the plastic regime, the response is typically characterized by stress hardening followed by strain softening beyond the ultimate stress [Simulia, 2011].

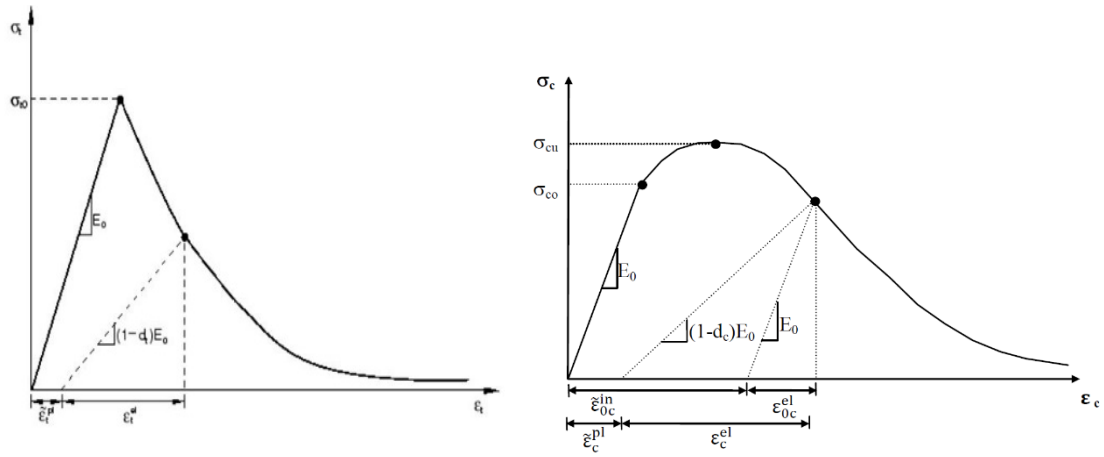

(a) Tension behavior of concrete

(b) Compression behavior of concrete

Figure 6- 1: Response of concrete to uniaxial loading [Obaidat, 2011]

The concrete damage plasticity model requires the values of elastic modulus, Poisson's ratio, the plastic damage parameters and description of compressive and tensile behavior. The five plastic damage parameters are the dilation angle, the flow potential eccentricity, the ratio of initial equi-biaxial compressive yield stress to initial uniaxial compressive yield stress, the ratio of the second stress invariant on the tensile meridian to that on the compressive meridian and the viscosity parameter that defines viscoplastic regularization. The values of the last four parameters were recommended by the ABAQUS documentation [Simulia, 2011] for defining concrete material and were set to 0.1, 1.16, 0.667, and 0.01, respectively. The dilation angle and Poisson's ratio were chosen to be 35° and 0.15, respectively.

The degradation of the elastic stiffness is characterized by two damage variables which are assumed to be functions of the plastic strains. The damage variables can take values from zero, representing the undamaged material, to one, which represents a total loss of strength. A linear relationship between the damage variable and stress was assumed.

- The second material considered in this FE Model was the FRP. For FRP, linear elastic behavior up to failure was assumed. Elastic modulus, Poisson's ratio, and tensile strength were needed for the simulation. The material type was assumed to be lamina with Poisson's ratio as 0.222.

- The model for the interface between FRP and concrete is of essential importance. A cohesive surface model was evaluated for describing the concrete-FRP interface. The cohesive model available in ABAQUS is a recommended choice for representing the interface behavior [Obaidat, 2011]. The cohesive model defines surfaces of separation and describes their interaction by defining a relative displacement at each contact point. The definition of the model is characterized by the parameters, initial stiffness, shear strength, fracture energy and curve shape of the bond slip model. Input values for the cohesive model found in the literature were widespread. In order to find the values of initial stiffness, shear strength and fracture energy that gave the best fit, the equations from [Obaidat, 2011] were used. Several iterations were performed to calibrate the model with the corresponding experimental results.

Model Geometry and element types

Based on the above-mentioned assumptions, a 3D FEM was created. The modeling involved defining the geometry, boundary condition, material properties, loads, analysis methods and contact. The defined geometry is discretized into elements. ABAQUS has an array of element types for modeling the beam. The concrete was modeled using C3D8R (eight-node solid) element. The FRP sheets were modeled using S4R (shell, 4-node) element. Figure 6- 2 illustrates the beam geometry modeled in ABAQUS.

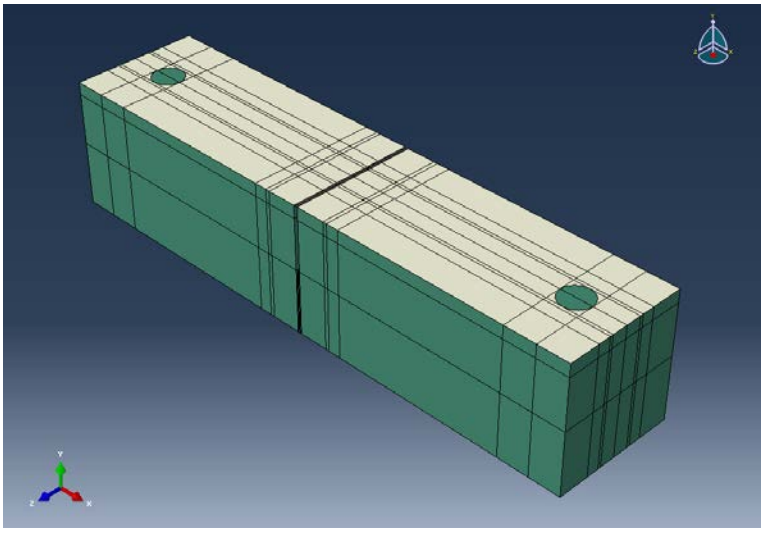

Figure 6- 2: ABAQUS model geometry

The first component of the model is the FRP sheet. The FRP was modeled as shell element as illustrated in Figure 6- 3. Two circular holes of diameter 2 in. each was inserted on both ends of the FRP layer to simulate the actual case of the beam after performing the pull-off test. The presence of these voids was necessary to consider any stress concentration that might happen at the end of the FRP layer.

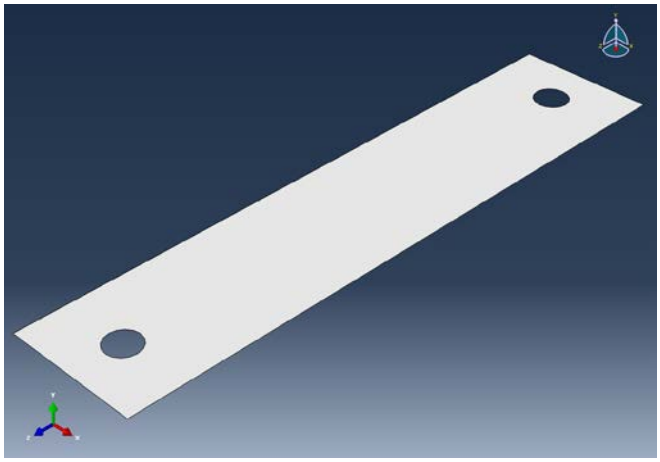

Figure 6- 3: FRP sheet as modeled in ABAQUS

The second component of the model was the concrete beam. The concrete geometry was modeled in ABAQUS as illustrated in Figure 6- 4. A notch was inserted in the concrete beam to model the actual beam specimen. Also, voids were modeled in some of the concrete element to simulate the voids created in the beam samples.

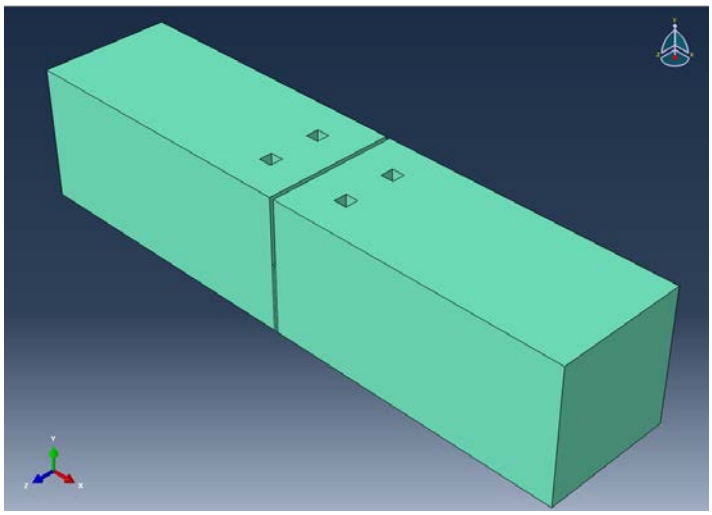

Figure 6- 4: Concrete beam as modeled in ABAQUS

Preliminary results obtained with a rather coarse mesh showed that it was fairly difficult to obtain convergence and the results were not acceptable. The results obtained from a fine mesh were more accurate. An even finer mesh gave almost the same result as the previous mesh but more time was needed for computations. Therefore a moderately fine mesh was chosen in this study. The solution time with this mesh is approximately 1 h. Figure 6- 5 illustrates the mesh used to model the concrete beam in this study.

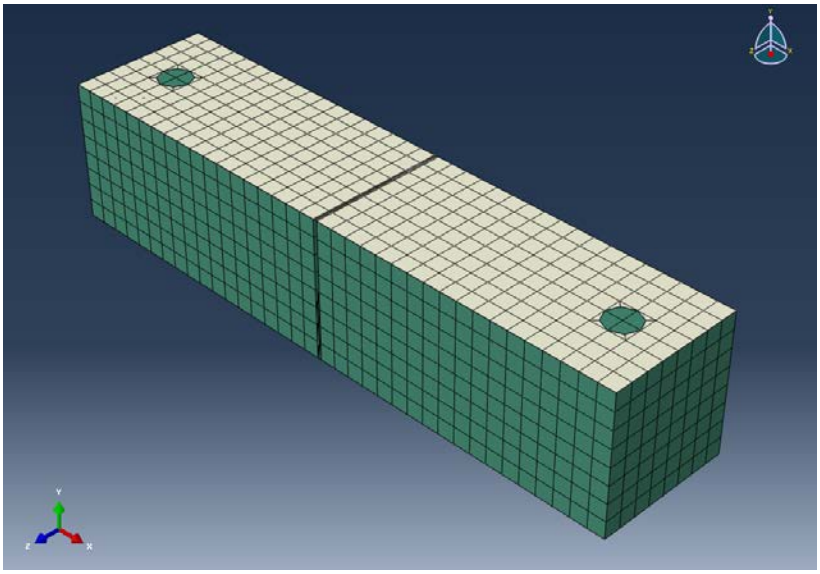

Figure 6- 5: Mesh used in ABAQUS model

Finally, the boundary conditions and loads were defined to complete the inputs of the ABAQUS model. The boundary conditions that represent structural supports specify values of displacement and rotation variables at appropriate nodes. The boundary conditions for the simulated beam was a hinge on one side and a roller for the other side to simulate the condition of the experimental test. The load was applied at midspan corresponding to the experimental situation. The experiment in this study was performed as a displacement controlled test. Therefore, a displacement at mid-span was used to control a constant displacement rate of 0.05 in/min similar to the experiment.

Model adjustment and calibration

The preliminary model is based on theoretical values and equations from literature and does not take into consideration the actual materials and test conditions. It is hence required to calibrate the finite element model to accurately reflect each of the elements used in the test.

The first step is to calibrate material properties input in the model with the actual material properties used in the experimental test. It was hence decided to carry out a few ASTM tests to make to collect the actual material properties and make the inputs more accurate. In order to determine the materials properties of the concrete used in the test, twelve concrete cylinders were taken as per [ASTM-C39, 2017] during the concrete casting. After 28 days, six cylinders were tested according to the [ASTM-C39, 2017] to find the compressive strength of the concrete. Another six cylinders were tested simultaneously with the bending test to capture the material properties of the concrete used. Table 6- 1 shows the results of the cylinders compressive test after 28 days. The Concrete compressive strength calculated based on these values is 3.3 ksi.

Table 6- 1: Cylinder test results

Cylinder no.	Failure Load (kip)
1	43
2	34
3	30.5
4	47.4
5	43.3
6	50.9

Two strain gages were installed on two sides of each of the remaining six concrete cylinders to plot the stress-strain diagram of the concrete. The setup of the ASTM

cylinders compressive test is illustrated in Figure 6- 6. The results of this test were used to determine the Young's modulus value of the concrete used (E = 27,753 MPa).

Figure 6- 6: ASTM cylinders compressive test setup

The next material properties required to calculate the model was the FRP. A total of six FRP coupons were tested to determine the tensile properties of the cured FRP laminate according to the [ASTM D3039, 2014]. Figure 6- 7 illustrates the coupon test performed to determine the material properties of the FRP. The results of this test were used as inputs of the material properties of the FRP in ABAQUS.

Figure 6- 7: ASTM FRP coupon test

After determining the actual material properties for each component used in this test, the next step was to define the contact properties of the concrete and the FRP. As the contact properties differ from one sample to the other corresponding to the parameters incorporated in each sample, it was necessary to determine the contribution of each parameter separately on the contact properties.

In order to achieve this goal, each parameter was assigned separate properties in the model inputs. The surface roughness effect was included in the friction coefficient properties of the contact. The Epoxy type and thickness effect were included in the damage properties of the contact. On the other hand, the voids effect was simulated by creating the voids in the model. Finally, the FRP type was included in the material properties of the FRP.

A series of iterations were performed to calibrate the models. For each iteration, the parameter values were selected to achieve a similar failure load in the model as per the corresponding experimental test. The load-displacement curve was plotted for each beam. Figure 6- 8 illustrates the load-displacement curve of a beam after calibration the

graph show an agreement between the performance of the experimental results and the ABAQUS model.

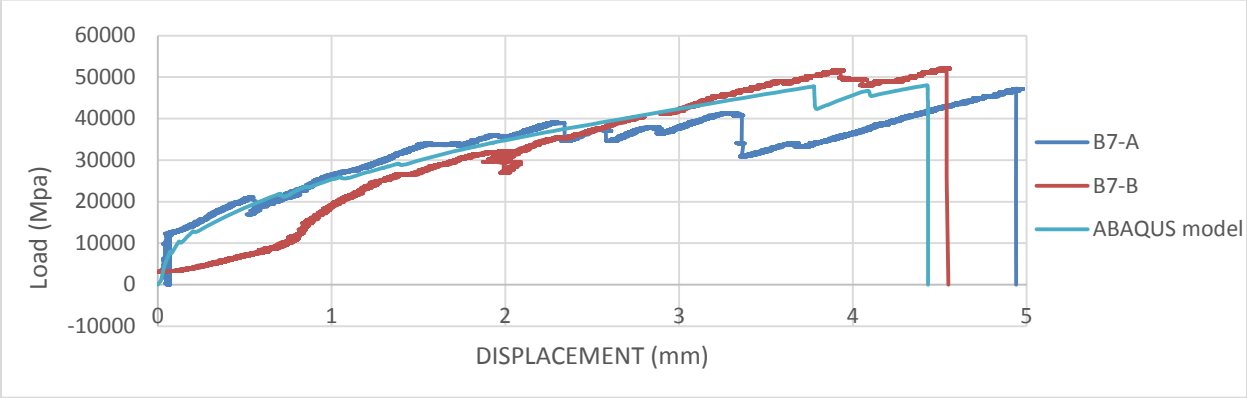

Figure 6- 8: Load-displacement curve of a beam

After several iterations, the following values were selected to represent the bond properties. The surface roughness was assigned a value of 0.1 and 0.3 in the friction coefficient of the contact properties were assigned to simulate the hand-grinding and the sandblasting respectively. The number of layers of Epoxy used was assigned a value of 0.29 and 0.42 in the shear damage parameter of the contact corresponding to type I and type II respectively. The Epoxy type was assigned a value of 1.7 and 3.7 in the fracture energy of the damage parameter of the contact corresponding to type I and type II respectively. Table 6- 2 presents the final results of the calibration process.

Table 6- 2: Results of the calibration process

Beam no.	Failure Load Experimental test (kip)	Failure Load ABAQUS model (kip)	Percentage change (%)
1	7.79	7.8	0.12
2	11.95	11.83	1.1
3	10.51	9.6	8.7

4	15.1	12.69	16
5	9.26	8.52	8
6	12.75	11.28	11.6
7	11.15	10.81	3.1
8	12.5	13.13	-5.1
9	5.975	5.514	7.8
10	9.51	9.86	-3.7
11	8.81	9.48	-7.7
12	13.4	11.24	16.2
13	8.3	7.3	12.1
14	11.6	9.95	14.3
15	11.45	9.88	13.8
16	11.85	11.36	4.2

After completing the calibration process, a value was assigned to each parameter in the study and could be used to simulate the effect of this parameter on the bond strength and the overall performance of the beam. This study focus on the effect of the surface roughness, Epoxy type, FRP type, number of Epoxy layers used and the number and size of voids on the bond behavior. The results from this chapter could be used reproduce the results from the experimental test and any desired additional combination of parameters that might be helpful in studying the bond behavior. The results of the calibrated model is presented below:

$$\text{Failure load } (\%) = 92.153 + 26.311\,[\text{FRP type}] + 18.975\,[\text{Number of Epoxy Layers}] + 5.054\,[\text{Epoxy type}] - 11.434\,[\text{surface Roughness}] - 2.028\,[\text{Voids 1}] - 4.752\,[\text{Voids 2}] - 4.494\,[\text{FRP type} * \text{Number of Epoxy Layers}] - 4.080\,[\text{FRP type} * \text{Epoxy type}] - 5.248\,[\text{FRP type} * \text{surface Roughness}] + 0.816\,[\text{FRP type} * \text{Voids 1}] + 1.187\,[\text{FRP type} * \text{Voids}] \quad \text{Eq. (6-1)}$$

Where, FRP type is -1 for FRP type I and +1 for FRP type II. Similarly, for each parameter in the previous equation, a value of -1 is assigned to the type I and a value of +1 is assigned to type II.

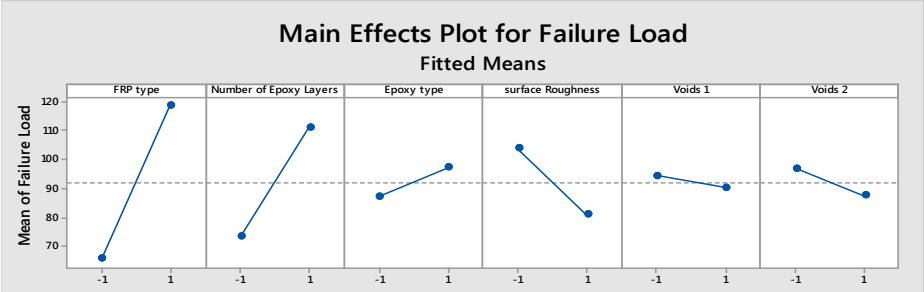

Figure 6- 9: Main Effect of the parameters

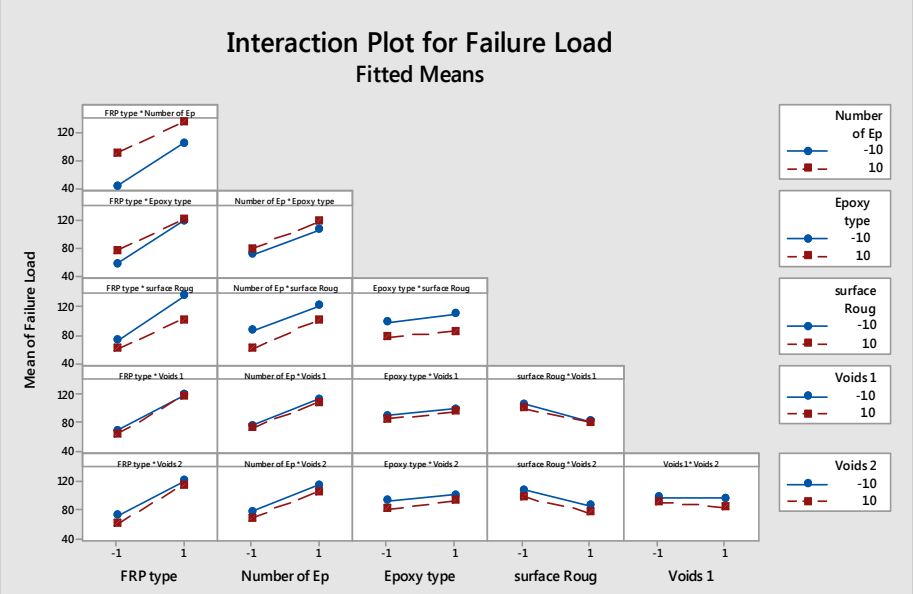

Figure 6- 10: interaction plots

To investigate the effect of voids on the bond strength a series of FEM models where prepared. Each model has voids inserted with different size under the FRP layer. The voids were chosen to be from 1% of the area up to 20%. Figure 6- 11 illustrates the effect of the voids on the bond strength. The figure shows a clear downtrend of the bond strength with the increase of voids size.

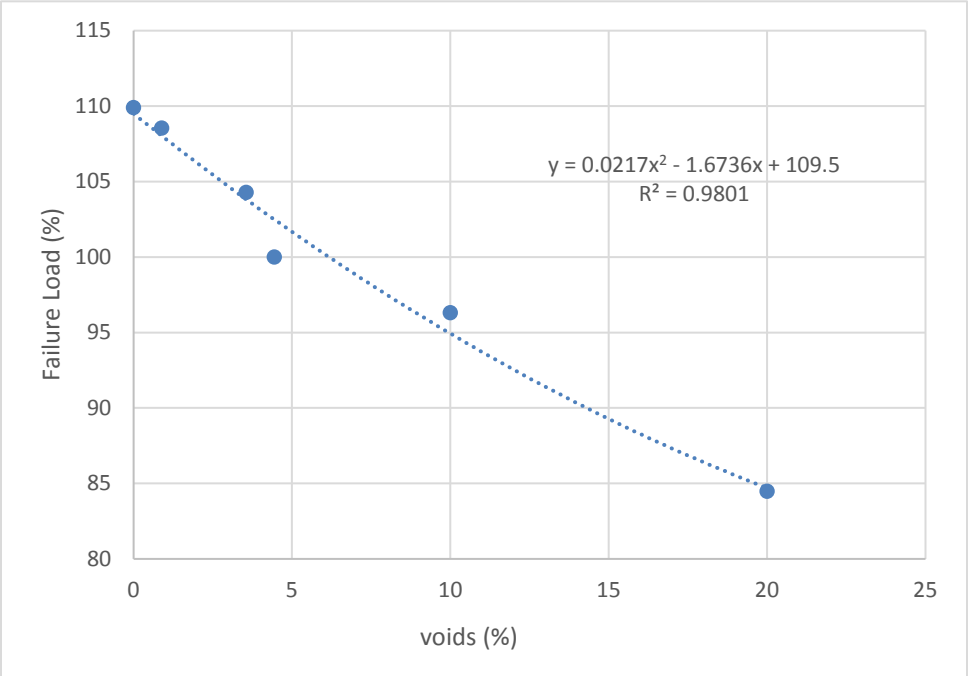

Figure 6- 11: Relationship between the voids area and the strength of the bond

Chapter 7

Conclusions and recommendations

Introduction

After scanning the beams using the different NDE methods and evaluating the strength of the beams using the destructive test, this chapter presents a summary for the findings and presents a proposed procedures for quantitative evaluation of the bond strength. The conclusion presented in this chapter could be used as a tool to assess and evaluate the condition of the bond between the concrete and the FRP in an existing structure strengthened with FRP.

Summary of findings and conclusion

This study explored the ability of Schmidt hammer, infrared camera, ultrasound tomography and ground penetrating radar (GPR) on identifying several parameters that are considered to have an effect on the bond strength between the FRP and the concrete. The parameters considered in this study were FRP type, number of Epoxy layers used, Epoxy type, surface roughness and voids.

In summary, the study demonstrated that all the NDE techniques used were capable of identifying some or all the parameters that affect the bond strength as described in the previous chapters. The research developed new formulas that could be used to find the relationship between the NDE readings versus the overall strength. The Quotient values from the Schmidt hammer test, the rate of cooling down of the temperature from the infrared camera test, the amplitude values from the ultrasound tomography test and finally the amplitude values from GPR test were studied. The conclusion of each NDE method is presented as following:

The first NDE method studied was the Schmidt hammer. In this method, the ratio of Q value from the FRP surface compared to the Q value from the concrete surface is used to evaluate the quality of the bond. This method was capable of identifying all the parameters in study. One equation was developed to represents the relationship between the Q value readings and the parameters that affect the bond strength. Additionally, this method proved to be successful in detecting any voids or delamination that might be hidden under the FRP surface. This method requires a point to point inspection and some voids may end up undetected.

The second NDE method presented was the infrared camera. In this method, the rate of cooling down of the FRP surface compared with the rate of cooling down of the concrete surface is used to evaluate the quality of the bond. This method wasn't able to identify all the parameters in the study. The infrared camera was not able to identify the Epoxy type used. One equation was developed to represents the relationship between the rate of cooling down and the parameters that affect the bond strength. In contrast, the infrared camera proved to be the most adequate for the detection of delamination or voids. The method is fast, easy and accurate. This method provides an overall view of the scanned area. The exact size of the voids could be detected.

The third NDE method presented was the ultrasound tomography test. In this method, the ratio of the amplitude of the ultrasound wave reflected at the FRP surface relative to the amplitude of the wave reflected at the concrete surface is used to evaluate the quality of the bond. This method was capable of identifying all the parameters in the study. Two equations were developed to represents the relationship between the amplitude readings and the parameters that affect the bond strength. Additionally, the proved to be

successful in detecting any voids or delamination that might be hidden under the FRP surface.

The last NDE method presented was the ground penetrating radar (GPR) test. In this method, the ratio of the amplitude of the radio wave reflected at the FRP surface relative to the amplitude of the wave reflected from the concrete surface is used to evaluate the quality of the bond. This method was capable of identifying all the parameters in the study. Two equations were developed to represents the relationship between the amplitude readings and the parameters that affect the bond strength. Additionally, the proved to be successful in detecting any voids or delamination that might be hidden under the FRP surface. Another advantage of this method is that it could perform continuous line scan.

The next part of this study was to perform destructive testing. The destructive testing was required to analyze the effect of each parameter on the bond strength. In order to complete this task, two destructive tests were performed. The first test was the pull-off test. This test investigates the strength of the bond in direct tension. The second destructive method was three points bending test. This test investigates the strength of the bond in bending. The results from both tests were used to calibrate several FEM models. The FEM models were required to evaluate the effect of all the parameters and the interaction between them. An equation was developed based on these results to calculate the expected failure load based on the actual parameters used.

In addition to the previous results, a series of FEM models were prepared to investigate the effect of voids on the bond strength. Each model included voids with specific size under the FRP layer to represent a percentage loss of the total area of the voids. The results showed a clear downtrend of the bond strength with the increase of voids size.

Proposed procedures

In order to implement the findings of this study and to successfully evaluate actual structures strengthened with FRP, a proposed procedure was prepared. The procedures could be followed to identify the bond strength of existing structures. The method included in this study can be helpful to engineers to investigate the quality of a new FRP application or evaluate the bond strength of existing FRP repair.

A flowchart was prepared to summarize the steps that need to be followed for a complete evaluation of the bond strength as illustrated in Figure 7- 1. The first step is to collect the available information about the repair work. If the information is available, a quick check of the bond strength could be performed. If not, a detailed procedure needs to be followed.

In the case of a quick check, one NDE method might be appropriate for the quick evaluation. The first step is to calculate the NDE parameter of the selected NDE method using the NDE equations provided in chapter 4 and using the repair information as inputs. Then, a complete scan of the area that requires evaluation need to be performed. After completing the scan, a comparison between the expected value calculated using the equation and the actual values recorded from the scan needs to be performed. If the values are similar, a conclusion about the quality of the bond can be drawn that the FRP application was properly executed and the bond strength is as expected. If the values are not similar, an additional step is required. In this step, the percentage of the area where the values are different need to be identified. If the area can be considered local, a quick solution could be to neglect the contribution of these areas on the total bond strength. To do so, these areas might be considered as voids and the voids chart presented in chapter

6 could be used. If the loss of strength is acceptable, the FRP bond could be considered as adequate. If the loss in bond strength exceeds the required values, a detailed procedure is necessary to judge the bond strength.

In the cases where a detailed check is required, at least three equations are required in that case. The first step is to select two or more NDE methods that cover the three required equations. The available NDE methods are: Schmidt Hammer (1 equation), Infrared camera (1 equation), Ultrasound tomography (2 equations) and Ground Penetrating Radar (2 equations). After selecting the NDE methods, the surface of the concrete and the surface of the FRP need to be scanned. After scanning, the areas that require evaluations, the FRP thickness needs to be measured and the areas with deboning and voids need to be identified. Using these data, the NDE equations presented in chapter 6 could be used to calculate the state of each parameter. Finally, the bond strength could be calculated using the information about the bond parameters deducted from the NDE equations and adding the voids area. The bond strength could be calculated using the bond strength formula presented in chapter 6.

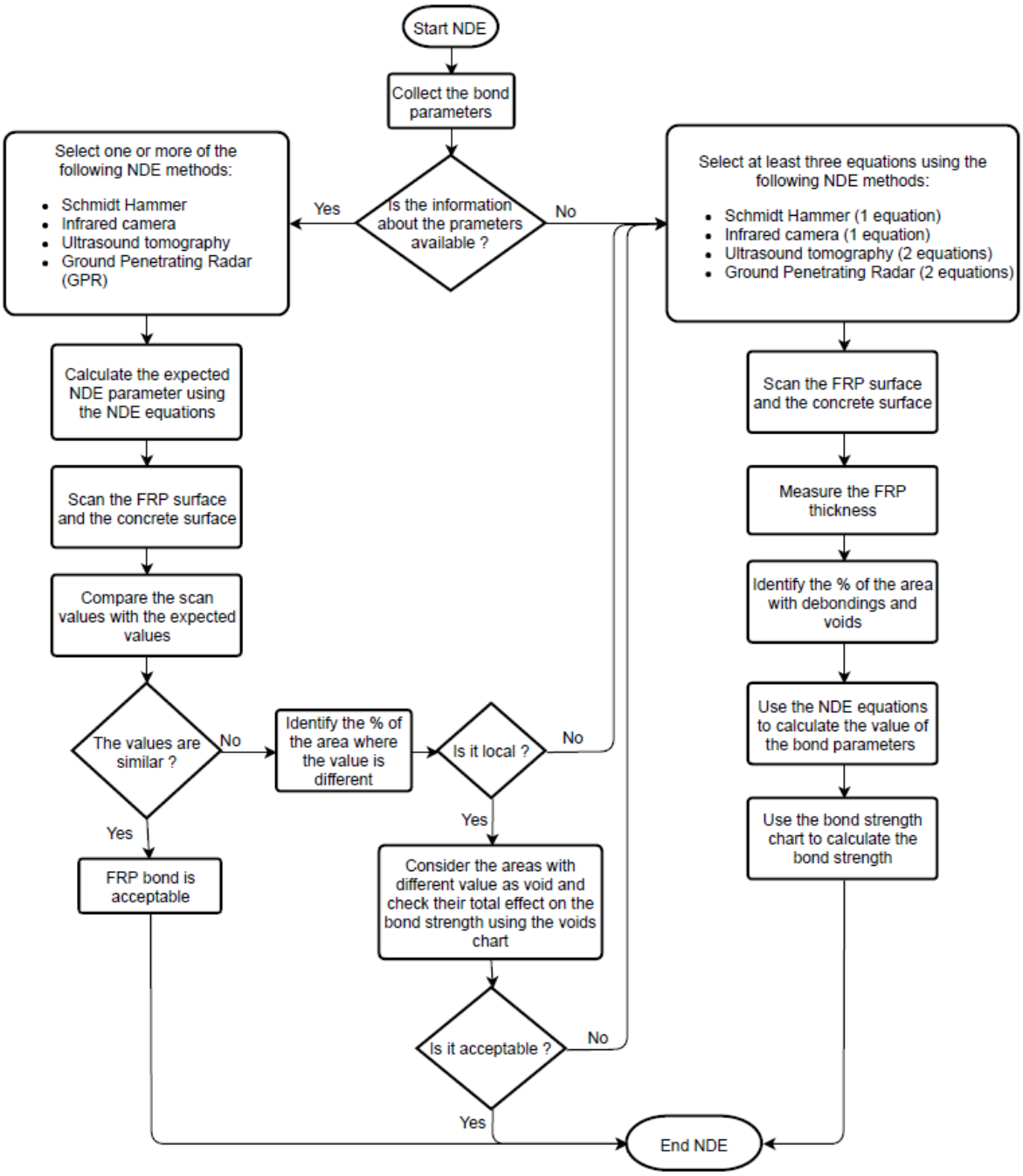

Figure 7- 1: Proposed procedures to evaluate the bond strength flowchart

Future Research

In this study, the effect of FRP type, number of Epoxy layers, Epoxy type, surface roughness and voids were considered to have an effect on the bond strength between the FRP and the concrete. The following are recommendations for future research work:

- This research was concerned with the effect of only five parameters on the bond strength. The effect of additional parameters that could affect the bond strength needs to be investigated. An example of additional factors to be considered are: the aging of Epoxy, application of FRP to concrete at hot versus cold temperature, application of FRP at direct sunlight versus shaded area, humidity, upward versus downward application and the application of the FRP on old versus new concrete.

- In this research, only two levels from each parameter were considered. The effect of others levels of these parameters needs to be investigated. For example, the surface roughness considered in this research was CSP2 and CSP3 as defined by ICRI. The effect of additional surface preparation on the bond strength could be considered.

- In this research, the ground penetrating radar with antenna 2600 MHz was used to develop the relationship between the bond strength and the amplitude in a form of two equations. Additional antenna frequency could be used to develop additional equations. Also, the orientation of the

antenna and the addition of other materials could be investigated to develop more formulas.

- In this research, due to some limitation, the number of samples used was reduced using the fractional factorial method resolution IV. This method neglect the third-degree interaction of the parameters. To consider the effect of this interaction, a full factorial design of the experiment is required.

Appendix A

Visual Basic code for GPR results

```
Sub SelectOpenCopyP1()
Dim vaFiles As Variant
Dim i As Long
Dim wbkToCopy As Workbook
vaFiles = Application.GetOpenFilename("Excel Files (*.CSV),
*.CSV", _
Title:="Select files", MultiSelect:=True)
If IsArray(vaFiles) Then
For i = LBound(vaFiles) To UBound(vaFiles)
Set wbkToCopy = Workbooks.Open(Filename:=vaFiles(i))
''''''''''''''''''''''''''''''''''''Start''''''''''''''''''''''''''
''''''''''''''''''''
''''''''''''''''''''''''''''''
Set sh = ThisWorkbook.Sheets("Sheet1")
Dim ndepth As Integer
Dim nlength As Integer
Dim minaavg As Double
Dim n1a As Integer
Dim p1a As Integer
Dim n2a As Integer
Dim p2a As Integer
Dim filenamemina() As String
Dim filenamemina1() As String
''''''''''Determine preliminary
nlength = WorksheetFunction.CountA(Range("C:C"))
ndepth = WorksheetFunction.CountA(Range("2:2"))
Dim ampavg() As Double
Dim p1ampavg() As Double
Dim n1ampavg() As Double
Dim p2ampavg() As Double
Dim n2ampavg() As Double
Dim rng1 As String
Dim rng2 As String
Dim rng As String
ReDim ampavg(1 To ndepth)
Dim sal As Double
Dim ali As Variant
Dim shiko As Variant
For ii = 1 To ndepth
ampavg(ii) = (((Cells(107, ii)) + (Cells(757, ii)))) / 2
Next ii
''''''''''''''''[end]''''''''''''''''''''''''''''''''''''''''''''''
'''''''''[start]determine the position of the positive and
negative amp''''''''''''''
For ii = 1 To ndepth
If ampavg(ii) < 0 Then
p1a = ii
GoTo line1
Else
End If
```

```
Next ii
line1:
For ii = p1a + 1 To ndepth
If ampavg(ii) > 0 Then
n1a = ii
GoTo line2
Else
End If
Next ii
line2:
For ii = n1a + 1 To ndepth
If ampavg(ii) < 0 Then
p2a = ii
GoTo line3
Else
End If
Next ii
line3:
For ii = p2a + 1 To ndepth
If ampavg(ii) > 0 Then
n2a = ii
GoTo line4
Else
End If
Next ii
line4:
ReDim p1ampavg(p1a)
ReDim n1ampavg(n1a)
ReDim p2ampavg(p2a)
ReDim n2ampavg(n2a)
For ii = 1 To p1a
p1ampavg(ii) = ampavg(ii)
Next ii
For ii = p1a To n1a
n1ampavg(ii) = ampavg(ii)
Next ii
For ii = n1a To p2a
p2ampavg(ii) = ampavg(ii)
Next ii
For ii = p2a To n2a
n2ampavg(ii) = ampavg(ii)
Next ii
filenamemina = Split(vaFiles(i), "\")
filenamemina1 = Split(filenamemina(UBound(filenamemina)), ".")
ThisWorkbook.Sheets("sheet1").Cells(i, 1) =
filenamemina1(LBound(filenamemina1))
For ii = 1 To ndepth
ThisWorkbook.Sheets("sheet1").Cells(i, ii + 1) = ampavg(ii)
Next ii
''''''''''''''''''[end]''''''''''''''''''''''''''''''''''''''''''''''''''''
```

```
''''''''''''''''''''''''''''''''''''''END''''''''''''''''''''''''
wbkToCopy.Close savechanges:=False
Next i
End If
End Sub
```

References

ACI Committee 440, *"Guide Test Methods for Fiber Reinforced Polymers (FRPs) for Reinforcing or Strengthening Concrete Structures (ACI 440.3R-04)"* American Concrete Institute, 2004.

ACI Committee 440, "*Guide for the Design and Construction of Externally Bonded FRP Systems for Strengthening Concrete Structures (ACI 440.2R-17)"* American Concrete Institute, 2017.

ASTM, C293/C293M, *"Standard Test Method for Flexural Strength of Concrete (Using Simple Beam with Third-Point Loading)."* Philadelphia, PA: American Society for Testing and Materials, 2016.

ASTM, C39/C39M-17b, *"Standard Test Method for Compressive Strength of Cylindrical Concrete Specimens"*. West Conshohocken, 2017.

ASTM D3039/D3039M-14, *"Standard Test Method for Tensile Properties of Polymer Matrix Composite Materials"* West Conshohocken, 2014.

ASTM D7522/D7522M-15, *"Standard Test Method for Pull-Off Strength for FRP Laminate Systems Bonded to Concrete Substrate"* ASTM International, West Conshohocken, PA, 2015.

ASTM D 3039/ D 3039M-14, *"Standard Test Method for Tensile Properties of Polymer Matrix Composite Materials"* ASTM International, 2014.

Akuthota, B., Hughes, D., Zoughi, R., Myers, J. and Nanni, A. "*Near-field microwave detection of disbond in carbon fiber reinforced polymer composites used*

for strengthening cement-based structures and disbond repair verification" Journal of Materials in Civil Engineering, 2004.

Antonaci, P., et al. *"Nonlinear Ultrasonic Evaluation of Load Effects on Discontinuities in Concrete"* N.p.: Elsevier, 2009.

Arrigoni M., S. E. Kruger, A. Blouin, D. Lévesque, B. Arsenault and J.-P. Monchalin *"Adhesive Bond Testing By Laser Induced Shock Waves"* 17th World Conference on Nondestructive Testing, 2008.

Bakis CE, Bank LC, Brown L, Cosenza E, Davalos JF, Lesko JJ, et al. *"Fiber reinforced polymer composites for construction-state-of-the-art review"* J. Compos. Constr, 2002.

Bastien Ehrhart, Bernd Valeske, Charles-Edouard Muller and Clemens Bockenheimer *"Methods for the Quality Assessment of Adhesive Bonded CFRP Structures"* NDT in Aerospace, 2010.

Bizindavyi L. and Neale K., "*Transfer lengths and bond strengths for composites Bonded to concrete"* journal of composites for construction, 1999.

Brotherhood CJ, Drinkwater BW and Dixon S. "*The Detectability of Kissing Bonds in Adhesive Joints using Ultrasonic Techniques"* Ultrasonics, 2003.

Bungey, John H., Michael G. Grantham, and Stephen Millard *"Testing of concrete"* Structures. Crc Press, 2006.

Cantrell J., *"Determination of Absolute Bond Strength from Hydroxyl Groups at Oxidized Aluminum-Epoxy Interfaces by Angle Beam Ultrasonic Spectroscopy"* Journal of Applied Physics, 2004.

Chen J. and Teng J., *"Anchorage strength models for frp and steel plates Bonded to concrete"* Journal of Structural Engineering, Vol. 127, No. 7, 2001.

Choi NS, Gu JU and Arakawa K. "*Acoustic Emission Characterization of the Marginal Disintegration of Dental Composite Restoration*" Composites: Part A, 2011.

Degala, Sandeep, et al., *"Acoustic emission monitoring of CFRP reinforced concrete slabs"* Construction and Building Materials 23.5, 2009.

Dobmann, G., et al., *"The potential of nuclear magnetic resonance (NMR) to non-destructively characterize early-age concrete by an one-sided access (OSA) technique."* National Seminar of ISNT chennai, Germany, 2002.

Doyum, A., and M. Duerer, *"Defect characterization of composite honeycomb panels by non-destructive inspection methods"* Proceedings DGZfP Conference, 2002.

Dutta, Shasanka Shekhar, "*Nondestructive evaluation of FRP wrapped concrete cylinders using infrared thermography and ground penetrating radar"* ProQuest, 2006.

Ékes, Csaba. "*GPR: A new tool for structural health monitoring of infrastructure"* Structural health monitoring & intelligent infrastructure 3rd conference, 2007.

Epp, Tyler, and Young-Jin Cha, *"Air-coupled impact-echo damage detection in reinforced concrete using wavelet transforms"* Smart Materials and Structures 26.2, 2016.

Frédéric Taillade, Marc Quiertant, Karim Benzarti, Jean Dumoulin and Christophe Aubagnac, *"Nondestructive Evaluation of FRP Strengthening Systems Bonded on RC Structures Using Pulsed Stimulated Infrared Thermography"* Infrared Thermography, Dr. Raghu V Prakash, 2012.

Galietti, U., Luprano, V., Nenna, S., Spagnolo, L. and Tundo, A. *"Non-destructive defect characterization of concrete structures reinforced by means of FRP"* Infrared Physics & Technology, 2007.

Gostautas, Richard S., et al., *"Acoustic emission monitoring and analysis of glass fiber-reinforced composites bridge decks."* Journal of bridge engineering 10.6, 2005.

GSSI, *"GSSI Handbook for RADAR Inspection of Concrete"* Geophysical Survey Systems, Inc, 2005.

Halabe, U., et al. *"Infrared Scanning of FRP Composite Members"* AIP Conference Proceedings. Vol. 657. No. 1. AIP, 2003.

Hesham M. Diab, *"Performance of different types of FRP sheets bonded to concrete using flexible adhesive"* The Online Journal of Science and Technology, 2013.

Hing, CL Caleb, and Udaya B. Halabe, *"Nondestructive testing of GFRP bridge decks using ground penetrating radar and infrared thermography"* Journal of Bridge Engineering 15.4, 2010.

Hosur, M. V., et al., *"Performance of stitched/unstitched woven carbon/epoxy composites under high velocity impact loading"* Composite Structures 64.3, 2004.

Hu W., et al. *"Detection of air blisters and crack propagation in FRP strengthened concrete elements using infrared thermography"* Inframation-The Thermographer's Conference, 2002.

Huo S and Reis H., *"Estimation of Adhesive Bond Strength in Laminated Safety Glass using Guided Mechanical Waves"* Proceedings of SPIE - The International Society for Optical Engineering, 2007.

Karbhari, Vistasp, et al. *"Methods for Detecting Defects in Composite Rehabilitated Structures"* N.p.: Oregon Department of Transportation, 2005.

De Lorenzis L., Miller **a**nd Nanni A., *"Bond of FRP Laminates to Concrete"* ACI Materials Journal, Vol. 98, No. 3, 2001.

FLIR, *"The Ultimate Infrared Handbook for R&D Professionals"* Academic, 2009.

Jamil, Maslina, et al. *"Concrete dielectric properties investigation using microwave nondestructive techniques"* Materials and structures 46.1-2, 2013.

Laight, A., et al. *"Measurement of the electromagnetic shielding properties of mechanically loaded composites"* Polymer composites 18.3,1997.

Le Crom B and Castaings M. *"Shear Horizontal Guided Wave Modes to Infer the Shear Stiffness of the Adhesive Bond layers"* Journal of the Acoustical Society of America, 2010.

Leung CKY, *"Delamination failure in concrete beams retrofitted with a bonded plate."* J. Mater. Civ. Eng., 2001.

Lubliner, J., et al. *"A plastic-damage model for concrete"* International Journal of solids and structures 25.3, 1989.

Coronado, Carlos A. and Maria M. Lopez, *"Sensitivity analysis of reinforced concrete beams strengthened with FRP laminates"* Cement and Concrete Composites, 2006.

Maerz, N. H. and Galecki, G., *"Preservation of missouri transportation infrastructures: Validation of FRP composite technology"* Technical Report Volume 4 of 5 Non-Destructive Testing of FRP Materials and Installation, Gold Bridge, Prepared by Missouri S&T and Missouri Department of Transportation, 2008.

Martin, Oliver, *"Comparison of different constitutive models for concrete in ABAQUS/explicit for missile impact analyses."* JRC Scientific and Technical Reports, 2010.

Meier U., *"Strengthening of structures using carbon fibre/epoxy composites"* Construction and Building Materials, 1995.

Meola, Carosena, Giovanni Maria Carlomagno, and Luca Giorleo, *"Geometrical limitations to detection of defects in composites by means of infrared thermography"* Journal of Nondestructive Evaluation 23.4, 2004.

Mirmiran, Amir and Yunmei Wei. *"Damage Assessment of FRP-Encased Concrete Using Ultrasonic Pulse Velocity"* N.p.: Journal of Engineering Mechanics, 2001.

Monica A. Starnes, Nicholas J. Carino, and Eduardo A. Kausel "*Preliminary Thermography Studies for Quality Control of Concrete Structures Strengthened with Fiber-Reinforced Polymer Composites"* Journal Of Materials In Civil Engineering, 2003.

Moore D. and Dennis Roach Ciji Nelson "*Non-Destructive Inspection of Adhesive Bonds in Metal-Metal Joints"* Presentation Sandia National Laboratories, 2009.

Nagarkar VV, Miller ST, Tipnis SV, Gaysinskiy V and Lempicki A, Brecher C. "*A high-resolution, high-speed CT/radiography system for NDT of adhesive bonded composites*" Proceedings of SPIE - The International Society for Optical Engineering, 2001.

Nakaba K., Kanakubo T., Furuta T. and Yoshizawa H., "*Bond Behavior between Fiber-Reinforced Polymer Laminates and Concrete"* ACI Structural Journal, V98, No.3, 2001.

NIST/SEMATECH, *"http://www.itl.nist.gov/div898/handbook/"* e-Handbook of Statistical Methods, 2012.

NSF (National Science Foundation) *"NDT Course Material"* Non Destruction Test Resource Center, 2009.

Obaidat, Yasmeen, "*Structural retrofitting of concrete beams using FRP-debonding issues"* Department of Construction Sciences, Lund University, 2011.

Pallempati, Hemachand, et al. "Condition Assessment of Fiber-Reinforced Polymer Strengthening of Concrete Bridge Components." Journal of Performance of Constructed Facilities, 2016.

Raihan, Rassel, *"Dielectric Poperties of Composite Materials During Damage Accumulation and Fracture"* N.p.: University of South Carolina, 2014.

Roth, D. J., et al., *"Microstructural and defect characterization in ceramic composites using an ultrasonic guided wave scan system"* AIP Conference Proceedings. Vol. 700. No. 1. AIP, 2004.

Ribolla, Emma La Malfa, et al., *"Assessment of bonding defects in FRP reinforced structures via ultrasonic technique"* CHALLENGE 2.3, 2016.

Rizkalla S., Hassan T. and Hassan N., *"Design recommendations for the useof FRP for reinforcement and strengthening of concrete structures"* Prog. Struct Engng Mater, 2003.

Saadatmanesh H. and Ehsani M., "*RC Beams strengthened with GFRP plates, I: Experimental study"* Journal of Structural Engineering, ASCE Vol. 117, 1991.

Sansalone, Mary, and William Streett, *"Impact Echo: Nondestructive Evaluation of Concrete and Masonry"* N.p.: Bullbrier Press, 2003.

Santulli and A.C. Lucia "*Relation between acoustic emission analysis during cure cycle and bonded joints performances*" NDT&E International 32, 1999.

Schabowicz, K. "Ultrasonic Tomography- The Latest Nondestructive Technique for Testing Concrete Members" N.p.: Elsevier, 2013.

Schroeder, J. A., et al., *"Non-destructive testing of structural composites and adhesively bonded composite joints: pulsed thermography"* Composites Part A: Applied Science and Manufacturing 33.11, 2002.

Simulia, Dassault Systèmes, *"Abaqus 6.11 theory manual."* Providence, RI, USA: DS SIMULIA Corp, 2011.

Taljsten B., *"Strengthening of beams by plate bonding"* J. Mat. Civ. Eng. ASCE, 1997.

Teng J., Chen J., Smith S. and Lam L., *"BEHAVIOUR AND STRENGTH OF FRP-STRENGTHENED RC STRUCTURES: A STATE-OF-THE-ART REVIEW"* Structures & Buildings, 2003.

Tzu-Yang Yu and Oral B. *"A far-field airborne radar NDT technique for detecting debonding in GFRP–retrofitted concrete structures"* NDT&E International, 2008.

Ueda, T. and Dai, J., *"Local bond stress slip relations for FRP sheets-concrete interfaces"* In Proc. of 6th international symposium on FRP reinforcement for concrete structures Singapore, 2003.

Yazdani N. et al. *"Condition Assessment of Fiber-Reinforced Polymer Strengthening of Concrete Bridge Components"* Journal of Performance of Constructed Facilities 30.6, 2016.

Ying Xu n, Rui Chen, Zhian Liu and Changjun Shao *"An acoustic-optical fiber NDE technique for interfacial debonding detection in FRP-retrofitted structures"* NDT&E International, 2015.

Biographical Information

Mina Riad received his Bachelor's degree in Civil Engineering from Cairo University, Egypt in 2007. He completed his Master's degree in Structural Engineering from Cairo University, Egypt in 2012 where he proposed an innovative new boundary element formulation for the analysis of multi-thickness slabs. His paper was published on innovative method (Boundary element analysis of multi-thickness shear-deformable slabs without sub-regions). He worked as a Structural Engineer with Dar Al Handasah. Dar Al Handasah is an international project design, management and supervision consultancy. Dar Al Handasah has served over 950 different clients in 63 countries with a staff of 6900 operating from 45 offices in the Middle East, Africa, Asia and Europe with five design centers in Beirut, Cairo, London, Pune and Amman. Dar Al Handasah is ranked #6 of the top international design firm by ENR. Mina has 7 years of experience in the design of several mega projects (Airports, Universities, Hotels and Residential Buildings).